THEORETICAL FORMULATION AND NUMERICAL IMPLEMENTATION OF ELECTROMAGNETIC AND THERMOMECHANICAL LOADING PROCESSES IN SOLIDS

by

Jesse D. Thomas

A dissertation submitted in partial fulfillment
of the requirements for the degree of
Doctor of Philosophy
(Aerospace Engineering)
in The University of Michigan
2008

Doctoral Committee:

Professor Nicolas Triantafyllidis, Chair
Professor James R. Barber
Professor Eric Michielssen
Associate Professor John A. Shaw
John R. Bradley, General Motors Research and Development

To my wife, Krystle.

ACKNOWLEDGEMENTS

TABLE OF CONTENTS

LIST OF FIGURES

Figure

LIST OF TABLES

Table

CHAPTER I

Introduction

The focus of this thesis is electromagnetic and thermomechanical loading processes in solids, inspired by the primary example process of electromagnetic forming (EMF). EMF is a cost-effective and flexible manufacturing technique for sheet metal forming. It consists of connecting an actuator (typically a copper wire solenoid) to a high energy capacitor equipped with fast action switches. When the capacitor is discharged, the large transient current that goes through the actuator generates by induction strong eddy currents in the nearby metallic workpiece. The presence of these induced currents, inside the magnetic field generated by the currents of the actuator, results in Lorentz body forces in the workpiece that are responsible for its plastic deformation.

The EMF technique was first used in this country in the 1950's and 60's, due to its advantages in enabling the fabrication of many complex geometry parts and enhancing the formability of low ductility materials. Numerous applications of EMF have been implemented in industrial production; among the more spectacular applications are engine nacelles made in a single piece, electromagnetic riveting guns and hammers (developed by NASA in the mid 1980s) used in the assembly of aircraft skins, and dent pullers[1]. Recent advances in electronics and energy storage make EMF technology ripe for mass

---

[1] Electroimpact Inc. http://www.electroimpact.com/

Figure 1.1: A 316L stainless steel sample formed electromagnetically using a uniform pressure actuator (courtesy of Dr. J. R. Bradley, General Motors Research and Development).

production, and plans are well under way for the large scale manufacturing of fuel cell plates and tubular frames for the automotive industry. One of the most promising recent applications is the manufacturing of fuel cell plates (Figures 1.1 and 1.2), where conventional stamping methods have failed and only the EMF technique can deliver the final shape without wrinkling or tearing deeper channels. American Trim Corporation[2] has recently been awarded $1M for researching methods to produce fuel cells more economically. A major automotive supplier, Dana Corporation[3], is already using EMF technology for producing tubular structures for space frame car designs.

The EMF techniques are popular in the aerospace and automotive industries because of several advantages they hold over conventional forming techniques. These advantages are process repeatability and flexibility (due to its electric nature, energy input can be easily and accurately adjusted), low cost single side tooling (thus reducing need for lubrication and tool marks), and high speed (typical process duration is on the order of 50 μsec). The most important advantage – and the main reason for the recent interest in EMF – is the resulting significant increase in ductility observed in certain metals, with

---

[2]American Trim, LLC `http://www.amtrim.com/fuel.php`

[3]Dana Limited `http://www.dana.com/technology/tailormetal.shtm`
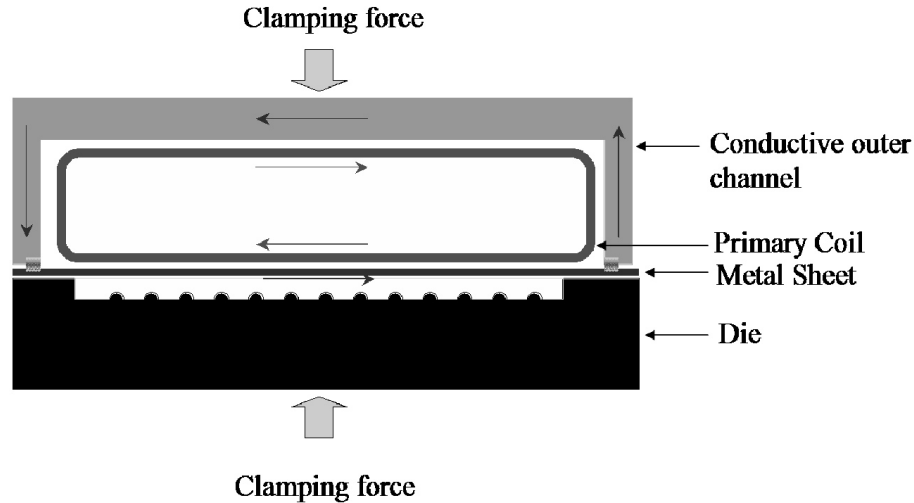
Figure 1.2: Schematic of a uniform pressure actuator. The primary coil has many turns going into the plane of the figure (courtesy of Dr. J. R. Bradley, General Motors Research and Development).

aluminum featuring preeminently among them.

Two issues are of particular importance when analyzing EMF. First is the increase in ductility and its causes, and second is the coupled modeling of the electromagnetic-mechanical interactions. Thus given subsequently, following a review of the early experimental and modeling work with EMF, are detailed discussions of the recent investigations relevant to the prediction of EMF ductility (Section 1.2) and to predictive modeling of EMF processes (Section 1.3). These sections explain the state of the art and the need for the present work, and an outline of this thesis is given at the end of this chapter.

1.1 Review of Early Work

Although research activity in EMF during the 1950's and 60's was important, as evidenced by the (mainly experimental) number of publications reported in the engineering literature, the research activity in the next twenty years (from the early 70's to early 90's) diminished to a trickle (see the survey article by Daehn et al. (1999)). Even in the hey-

day of EMF research, the scarcity of modeling work for these processes is strikingly noticeable. The main reason can be attributed to timing: computational methods and the hardware required for the numerical execution of the related algorithms were not yet in place. Although the physics of these complex thermomechanical plus electromagnetic phenomena were in principle understood, the pertaining coupled nonlinear systems of partial differential equations could not be solved with the technology available at that time.

Of the initial modeling efforts in EMF, one should mention the work of Furth and Waniek (1956) and Furth et al. (1957), who describe the basic equations of the problem, as do the analytical studies of Birdsall et al. (1961) and Meagher (1964). The modeling of Baines et al. (1965) involves many simplifying assumptions, with the goal of providing analytical results. Subsequent work by Al-Hassani et al. (1967, 1974) relaxed some of the previous assumptions and calculated numerically the Lorentz forces at the workpiece. As computing power became cheaper and more readily accessible, a new set of EMF modeling studies has emerged since the 1980's. Of particular interest here is the experimental and theoretical paper by Gourdin (1989), who studied the electromagnetic expansion of copper, tin, and lead rings. Gourdin (1989) formulated his coupled problem and considerably reduced the number of simplifying assumptions by taking into account the geometry changes of the ring to find the correct induced currents (shown to be in close agreement with his experimental results). His modeling of the ring's mechanical properties assumed a uniaxial deformation and several stress-strain laws but did not model necking or fracture. It is worth mentioning here that a number of studies have addressed the mechanical aspects of ring expansion and fragmentation (Becker, 2002; Grady and Benson, 1983; Pandolfi et al., 1999; Sørensen and Freund, 2000) using 3-D modeling of the ring and sophisticated constitutive equations and failure criteria. However, these mechanics-based

studies ignored the coupled nature of the problem and imposed the velocity boundary conditions on the specimen.

At about the same time as Gourdin (1989), Takatsu et al. (1988) published their experimental and theoretical study of the deformation of a clamped circular plate electromagnetically loaded by a flat spiral coil. They took into account the rate sensitivity of the plate and the effect of geometry change in the specimen on the induced currents but ignored temperature and bending effects (membrane solution used for the plate). Their interest was in predicting the plate's deformed shape, so their modeling never addressed the issue of localization and fracture.

Unlike the case of standard metal forming processes, to the best of the author's knowledge there is unfortunately no English language book dedicated to the EMF processes, save for the recent translation of the work by Belyy et al. (1977). The closest engineering book on the subject is perhaps the book by Moon (1984) on "Magneto-solid Mechanics", which discusses the calculation of Lorentz forces in metals from the angle of magnetoelastic buckling, applications that do not involve large strain deformations of the electromagnetically loaded solids.

1.2   EMF Ductility

There is extensive recent work that investigates forming limits under EMF processes. Experimental results by Balanethiram and Daehn (1992, 1994) with die impact EMF show dramatic increases (compared to conventional forming) in the ductility of AA6061-T4. Their work demonstrates that electromagnetically formed aluminum alloys are potentially and significantly more ductile than conventionally formed steel alloys (DFQ steel, which is about twice as ductile as conventionally formed AA6061-T4). A key ingredient in this ductility increase is the strain-rate sensitivity of the material's constitutive

response, as explained by Hutchinson and Neale (1977). A detailed theoretical explanation of this observed increase in formability, based on fully coupled electromagnetic and thermomechanical modeling of the free expansion of an electromagnetically loaded ring, was recently provided by Triantafyllidis and Waldenmyer (2004).

There is further recent work (Fressengeas and Molinari, 1989; Hu and Daehn, 1996; Imbert et al., 2005a,b; Knoche and Needleman, 1993; Mercier and Molinari, 2004; Oliveira and Worswick, 2003; Oliveira et al., 2005; Regazzoni et al., 1986; Seth and Daehn, 2005; Seth et al., 2005; Zhang and Ravi-Chandar, 2006) examining high strain rate (EMF and non-EMF) free forming limits. Oliveira and Worswick (2003) and Oliveira et al. (2005) show little increase in ductility due to high EMF strain rates, Zhang and Ravi-Chandar (2006) show no increase in uniform strain under EMF ring expansion, and Oosterkamp et al. (2000) show little strain-rate sensitivity in aluminum. The work by Oosterkamp et al. (2000) uses a split Hopkinson pressure bar to examine strain rates up to 2 10^3 s^{-1}, with a moderate number of data points, and reports that apparent strain-rate sensitivity is an artefact and not inherent in the material. However, other work, such as that by Hu and Daehn (1996), indicates high strain rate free formability increases, and Vural et al. (2004) and Yadav et al. (1995) show significant strain-rate sensitivity in aluminum. In particular, Vural et al. (2004) use the shear compression specimen technique (e.g. see Rittel et al. (2002)) to give extensive data for AA6061-T6 up to strain rates on the order of 10^4 s^{-1}. This data shows distinct strain-rate sensitivity above 10^3 s^{-1}. Also, several of the above mentioned recent investigations (Fressengeas and Molinari, 1989; Hu and Daehn, 1996; Knoche and Needleman, 1993; Mercier and Molinari, 2004; Regazzoni et al., 1986) show theoretically that inertial effects can delay instability. These investigations also point to the fact that the physical dimensions of the sample affect strains to instability and rupture.
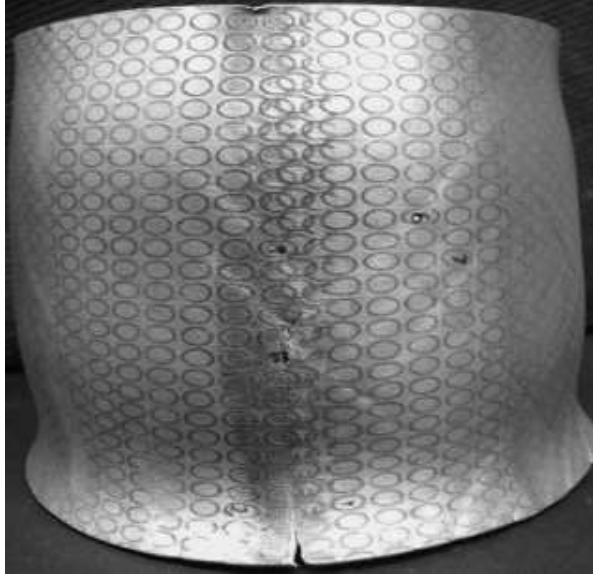
Figure 1.3: Onset of necking in a freely, electromagnetically expanded tube (courtesy of Professor Glenn Daehn, The Ohio State University).

In order to quantify the ductility of sheet metal, a key concept is that of a forming limit diagram (FLD), according to which a thin sheet (stress-free in the thickness direction) is subjected to proportional in-plane straining until the onset of localization. Typical examples of an EMF process with these (approximate) forming conditions are circular plate expansion (loaded by a flat coil parallel to the plate) and axisymmetric tube bulging (loaded by a cylindrical coil coaxial with the tube). Figure 1.3 shows a freely, electromagnetically expanded tube at the end of deformation with necking zones. There is a voluminous mechanics literature going back to the early 1970's addressing the choice of localization criterion as well as the influence of the constitutive properties on the onset of localization prediction. However, all of these investigations address a mechanical deformation phenomenon but none – to the best of the author's knowledge – addresses the coupled electromagnetic-thermomechanical localization problem that occurs with electromagnetic forming of sheet metal, thus motivating the present work.

1.3 Modeling of EMF Processes

Predictive modeling of EMF and other coupled electromagnetic-mechanical processes has also been a topic of extensive research in recent years. Semi-analytical techniques have been applied to these coupled problems for rings and plates with some success, notably in the previously mentioned works of Gourdin (1989) and Triantafyllidis and Waldenmyer (2004), for ring expansion, and of Takatsu et al. (1988), for plate bulging. These investigations employ fully coupled techniques that rely on known integration forms and inductance formulas that take advantage of the special geometry of rings and plates. However, they do not generalize to arbitrary geometries.

Recently, numerical solutions of coupled electromagnetic-mechanical problems with more complex geometries have been discussed in the literature. A good survey may be found in El-Azab et al. (2003), and since that work much progress has been made. The coupled solutions in the literature use either loose coupling of separate electromagnetic and mechanical solvers or a staggered approach where a unified code solves separately the electromagnetic and mechanical (and thermal) problems at each solution step. Often commercial finite element method (FEM) codes form the basis of the solution, as in Oliveira et al. (2005), Karch and Roll (2005), and L'Eplattenier et al. (2006). Also, good reviews of different coupled techniques for EMF solutions are given in Kleiner et al. (2004) and Svendsen and Chanda (2005). Furthermore Svendsen and Chanda (2005) along with Stiemer et al. (2006) introduce a new finite element technology specifically to solve electromagnetic-mechanical problems (see also Reese et al. (2005) and Unger et al. (2006)). Another program, which uses the Arbitrary Lagrangian-Eulerian (ALE) framework, was employed by Fenton and Daehn (1998) to simulate EMF plate bulging, and a related staggered scheme in the ALE framework is given by Rieben et al. (2006).

Despite their sophistication, all these techniques lack both a consistent, fully coupled variational formulation and a consistent, efficient numerical solution algorithm.

1.4 Outline of Present Work

The goals of this investigation are twofold: first to address EMF ductility from a constitutive point of view by examining the onset of strain localization in thin sheets subjected to EMF loading conditions and second to present the consistent formulation and implementation of the coupled electromagnetic-mechanical problem in finitely strained solids. More specifically, addressing the first objective involves: i) the theoretical formulation for the onset of necking in an electromagnetically loaded thin sheet, i.e. subjected simultaneously to in-plane stresses and electric currents, ii) the investigation of the influence of the process characteristics and constitutive law on the resulting necking predictions, i.e. how the various aspects of the EMF process and thermoviscoplastic constitutive law influence the FLD, and iii) the comparison of the general theory with forming limits from relevant experiments. The analysis here is general for EMF process ductility calculations, but for reasonable data the simulation is based on aluminum alloys and axisymmetric processes. Since the constitutive choice is of paramount importance for the FLD predictions, the bulk of the results pertain to investigating how different parameters of the adopted law (hardening, rate, and thermal sensitivity as well as yield surface shape) affect onset of necking predictions.

To address the second objective the work covers: i) the derivation of the general governing electromagnetic and mechanical equations, including direct and variational methods, ii) the application of the eddy current approximation to the variational technique to provide a consistent variational formulation for EMF processes that is appropriate for numerical implementation, iii) the consistent implementation of this variational formula-

tion, which provides a theoretical justification for a staggered solution scheme, and iv) the numerical validation of the formulation and implementation and simulation of relevant EMF processes, including the novel problem of an electromagnetically expanded tube with a non-conducting outer coating.

CHAPTER II

Ductility of Electromagnetically Loaded Thin Sheets

The ductility of thin sheets under EMF conditions is strongly influenced by the sheet's constitutive response. To investigate formability mechanisms for EMF processes, one therefore must consider the details of the constitutive response's effect on forming limits. The consistent approach to this issue must involve the fully coupled electromagnetic and mechanical modeling of the actuator and the workpiece. This is a computationally intensive process that requires the development of sophisticated algorithms for the solution of a dynamic finite strain thermoplasticity boundary value problem coupled (in view of the driving Lorentz body forces) to an electromagnetic problem with moving boundaries. Although this direct approach is the correct way for accurate calculations of specific EMF processes (with known part and actuator geometries), and is discussed in Chapter III, the designer can be helped by some simpler, and considerably more rapid, calculations that give a reasonable estimate of the ductility of a given alloy under EMF conditions. With this requirement in mind, a general theory to calculate EMF-based FLD's is proposed, in which the calculation of strains at the onset of necking in a sheet accounts for the presence of electric currents and the resulting ohmic heating effect.

The presentation is organized as follows. Section 2.1 introduces the theoretical formulation of the onset of necking problem in a finitely strained thin sheet under combined

in-plane stresses and electric currents. The analysis is based on a Marciniak-Kuczynski "weak band" model using a full Lagrangian formulation. The same section deals with the most general form of the thermoviscoplastic constitutive law and explains the choice for the strain and current density profiles. In Section 2.2, following a brief explanation of the numerical algorithm adopted for solving the problem's ordinary differential equations (ODE's), the results of the investigation are presented and discussed. The general theory is then applied to comparisons with experiments in Section 2.3. Section 2.4 is a concluding discussion of the work. The important issue of choice for the onset of necking criterion is presented in detail and justified in the Chapter II Appendix, Section 2.A, where the weak band imperfection criterion is compared to a linearized stability criterion that is independent of imperfection size.

2.1   Problem Formulation

As discussed previously, a weak band analysis for the localization of deformation is used to analyze the onset of necking in an unconstrained, electromagnetically expanded axisymmetric tube or plate, modeled as a biaxially stretched sheet subjected to electric currents. The governing equations for the mechanical and electrical field quantities in the localized deformation zone are followed by the presentation of the rate and temperature-dependent constitutive models for the sheet. The adopted strain and electric current profiles for modeling the EMF process complete the simulation description.

2.1.1   Localization Zone Analysis

Figure 2.1 shows a thin sheet under plane stress conditions, an idealization of a small portion of a tube or plate sheet, thus ignoring curvature effects. Inertia effects are also ignored in the present analysis, and the tube or plate hoop direction and the 1-direction in Figure 2.1 are taken coincident. Localized deformation is assumed to occur in a narrow
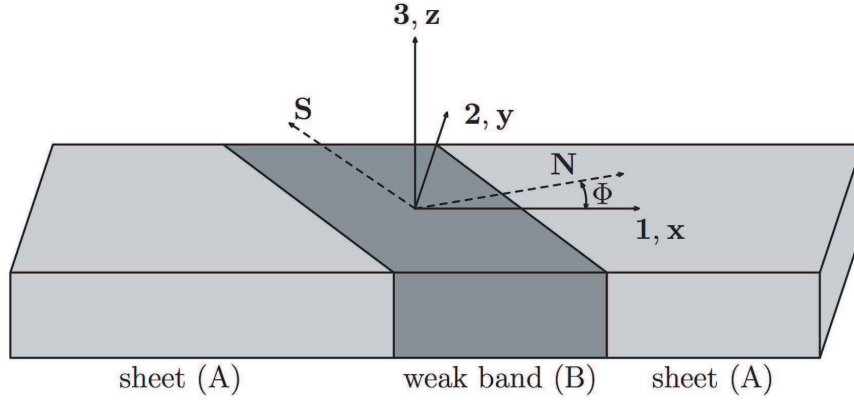
Figure 2.1: Reference configuration geometry of the weak band.

band (B) with normal direction $N = i\cos\Phi + j\sin\Phi$ and tangent $S = -i\sin\Phi + j\cos\Phi$. These are the reference configuration directions, while the corresponding current configuration quantities are denoted by n, s, and ϕ. An initial imperfection differentiates the band and sheet and is implemented as either a material parameter or geometric (thickness) discontinuity in the reference configuration properties. With this model in place, one endeavors to calculate the deformation gradient F^B, stress σ^B, current j^B, temperature θ^B and internal variable (plastic strain) ϵ_B^p inside the band from their counterpart quantities outside the band (F^A, σ^A, j^A, θ^A and ϵ_A^p).

The large deformations inherent in this problem lead naturally to a full Lagrangian (reference configuration) formulation. A current configuration formulation could have been chosen, but the Lagrangian formulation consistently accounts for the complex large deformation kinematics, reducing the likelihood of error in their representation. Mechanical considerations require that displacement and traction be preserved across the band. More specifically displacement continuity across the band dictates[1]

$$\left[F_{\alpha\beta}^B - F_{\alpha\beta}^A\right] S_\beta = 0, \qquad (2.1.1)$$

---

[1]Here and subsequently Greek indexes range from 1 to 2 while Latin indexes range from 1 to 3. Einstein's summation convention over repeated indexes is implied, unless specified otherwise.

and traction continuity requires

$$N_\alpha \left[\Pi^B_{\alpha\beta} - \Pi^A_{\alpha\beta} \right] = 0, \tag{2.1.2}$$

where the first Piola-Kirchhoff (P-K) stress $\mathbf{\Pi}$ is expressed in terms of the Cauchy stress as

$$\Pi_{ij} = \det(\mathbf{F})[F^{-1}_{ik}\sigma_{kj}]. \tag{2.1.3}$$

Electrical considerations require that the electric current and tangential component of the electromotive force must be preserved across the band. From current continuity one has

$$N_\alpha \left[J^B_\alpha - J^A_\alpha \right] = 0, \tag{2.1.4}$$

where the electric current density vector in the reference configuration $\mathbf{J}$ is related to $\mathbf{j}$, its counterpart in the current configuration, by

$$J_i = \det(\mathbf{F})[F^{-1}_{ik}j_k]. \tag{2.1.5}$$

Faraday's induction law requires that the tangential component of the electromotive force in the reference configuration $\mathbf{E}$ be preserved, which dictates

$$S_\alpha \left[E^B_\alpha - E^A_\alpha \right] = 0, \tag{2.1.6}$$

where the reference configuration electromotive force $\mathbf{E}$ is related to its current configuration counterpart $\mathbf{e}$ by

$$E_i = e_k F_{ki}. \tag{2.1.7}$$

Finally, assuming adiabatic heating both outside (A) and inside (B) the weak band (thus the various field quantities need not be indexed), energy conservation (per unit current volume) dictates

$$\mu c_p \dot{\theta} = \chi \sigma_e \dot{\epsilon}^p + e_i j_i, \tag{2.1.8}$$

where μ is the mass density, c_p is the specific heat, $\dot{\theta}$ is the rate of change of the tempera-ture, χ $(0 < \chi < 1)$ is the plastic work conversion factor and $\sigma_e \dot{\epsilon}^p$ is the plastic dissipation (σ_e is the equivalent Cauchy stress and ϵ^p is the plastic strain).

2.1.2 Constitutive Response

Due to the electromagnetic nature of the forming process, the simulation requires two sets of constitutive equations: one for the mechanical response and one for the electrical response.

2.1.2.1 Mechanical Constitutive Law

An EMF process imposes high strain rates and high temperatures on the workpiece, thus requiring a temperature-dependent viscoplastic constitutive law, which can be de-scribed by

$$\overset{\circ}{\sigma}_{ij} = \mathscr{L}^e_{ijkl} D^e_{kl}, \tag{2.1.9}$$

where $\overset{\circ}{\sigma}_{ij}$ denotes the convected rate of Cauchy stress, $\mathscr{L}^e_{ijkl}$ are the solid's elastic moduli, and D^e_{ij} are the elastic components of the strain-rate tensor. The frame-invariant stress rate $\overset{\circ}{\sigma}_{ij}$ is given in terms of the stress rate $\dot{\sigma}_{ij}$ by

$$\overset{\circ}{\sigma}_{ij} = \dot{\sigma}_{ij} + L_{ki}\sigma_{kj} + \sigma_{ik}L_{kj}, \tag{2.1.10}$$

where L_{ij} is the solid's velocity gradient. Note that the choice of the convected rate of stress is arbitrary.

The strain rate may be additively decomposed into an elastic $\boldsymbol{D}^e$, a plastic $\boldsymbol{D}^p$ and a thermal $\boldsymbol{D}^\theta$ part, as follows

$$D_{ij} = D^e_{ij} + D^p_{ij} + D^\theta_{ij}. \tag{2.1.11}$$

The plastic part of the strain rate for a viscoplastic solid which is described in terms of

only one internal variable ϵ^p – the accumulated plastic strain – is

$$D_{ij}^p = \dot{\epsilon}^p \frac{\partial \sigma_e}{\partial \sigma_{ij}}, \qquad (2.1.12)$$

while the thermal part of the strain rate is

$$D_{ij}^\theta = \eta \dot{\theta} \delta_{ij}, \qquad (2.1.13)$$

where η is the thermal expansion coefficient. The internal variable ϵ^p determines the size of the material's current yield surface, which is characterized by the equivalent stress σ_e, and the relation between ϵ^p and the solid's quasistatic uniaxial response $\sigma = g\left(\epsilon^p, \theta\right)$ is

$$\dot{\epsilon}^p = \dot{\epsilon}_0^p \left[\left(\frac{\sigma_e(\sigma_{ij})}{g\left(\epsilon^p, \theta\right)} \right)^{1/m(\theta)} - 1 \right], \qquad (2.1.14)$$

where $m(\theta)$ is the solid's rate-sensitivity exponent that is (in general) a function of temperature and $\dot{\epsilon}_0^p$ is a material constant. Expressions that are based on experiments will be given subsequently for $\sigma_e\left(\sigma_{ij}\right)$ and $g\left(\epsilon^p, \theta\right)$.

Attention is now turned to the required kinematical relations. The components of the strain rate D_{ij} and velocity gradient L_{ij} are given in terms of the deformation gradient and its rate by

$$D_{ij} = \frac{1}{2}\left(L_{ij} + L_{ji}\right), \quad L_{ij} = \dot{F}_{ik} F_{kj}^{-1}. \qquad (2.1.15)$$

In the preceding equations the constitutive relations are presented in a general three dimensional form. For the EMF tube or circular disk bulging simulation, a state of plane stress is assumed. Consequently, only in-plane deformations are considered, and in view of transverse isotropy of the sheet one has

$$F_{\alpha 3} = F_{3\alpha} = 0, \qquad (2.1.16)$$

while the state of plane stress dictates

$$\sigma_{i3} = 0. \qquad (2.1.17)$$

The plane stress version of the constitutive equation (2.1.9) is thus expressed as

$$\mathring{\sigma}_{\alpha\beta} = \hat{\mathscr{L}}^e_{\alpha\beta\gamma\delta} D^e_{\gamma\delta}, \tag{2.1.18}$$

where the plane stress elastic moduli $\hat{\mathscr{L}}^e_{\alpha\beta\gamma\delta}$ and the full three-dimensional moduli are related by

$$\hat{\mathscr{L}}^e_{\alpha\beta\gamma\delta} = \mathscr{L}^e_{\alpha\beta\gamma\delta} - \mathscr{L}^e_{\alpha\beta33}(\mathscr{L}^e_{3333})^{-1}\mathscr{L}^e_{33\gamma\delta}. \tag{2.1.19}$$

To complete this temperature-dependent, viscoplastic model two experimentally based elements are necessary: the rate-independent uniaxial response $\sigma = g(\epsilon^p, \theta)$ and the yield surface $\sigma_e(\sigma_{ij})$.

The experimentally motivated (see Yadav et al. (2001)) rate-independent uniaxial response employed here is given by

$$g(\epsilon^p, \theta) = \sigma_y \left[1 + \frac{\epsilon^p}{\epsilon_y}\right]^n \left[1 - \left(\frac{\theta - \theta_0}{\theta_m - \theta_0}\right)^\alpha\right], \tag{2.1.20}$$

where σ_y is the yield stress, $\epsilon_y = \sigma_y/E$ is the yield strain, n is the hardening exponent, θ_m is the melting temperature, θ_0 is the reference temperature, and α is the thermal sensitivity exponent.

The mechanical constitutive equations are completed with the yield surface description. Three different yield surfaces are considered in this work. The first is the familiar von Mises (isotropic, quadratic) yield surface, included for comparison purposes. The second is an isotropic, non-quadratic yield surface. These two models are appropriate for isotropic materials that do not exhibit the Bauschinger effect, i.e. materials that exhibit no difference between their tensile and compressive responses, and both are described by

$$\sigma_e = \left[\left(|\sigma_1 - \sigma_2|^\beta + |\sigma_2 - \sigma_3|^\beta + |\sigma_3 - \sigma_1|^\beta\right)/2\right]^{1/\beta}, \tag{2.1.21}$$

where β is a coefficient determined by the yield surface and material type and σ_i are the principal values of the Cauchy stress tensor. The von Mises yield surface requires $\beta = 2$,

and for the non-quadratic surface, experimental evidence suggests $\beta = 8$ for aluminum (see Barlat et al. (1997b) and references cited therein).

The third yield surface considered is an anisotropic non-quadratic yield surface Yld94, proposed for aluminum alloys by Barlat et al. (1997a). It is described by

$$\sigma_e = \left[\left(\alpha_x |s_2 - s_3|^\beta + \alpha_y |s_3 - s_1|^\beta + \alpha_z |s_1 - s_2|^\beta \right) /2 \right]^{1/\beta}, \qquad (2.1.22)$$

where again $\beta = 8$ for aluminum. Moreover, the auxiliary isotropic stress $\mathbf{s}$ (with principal values s_1, s_2, s_3) is related to the actual Cauchy stress $\boldsymbol{\sigma}$ by

$$s_{ij} = L_{ijkl}\sigma_{kl}, \quad \mathbf{L} = \begin{bmatrix} \frac{1}{3}(c_2 + c_3) & -\frac{1}{3}(c_3) & -\frac{1}{3}(c_2) & 0 & 0 & 0 \\ -\frac{1}{3}(c_3) & \frac{1}{3}(c_3 + c_1) & -\frac{1}{3}(c_1) & 0 & 0 & 0 \\ -\frac{1}{3}(c_2) & -\frac{1}{3}(c_1) & \frac{1}{3}(c_2 + c_1) & 0 & 0 & 0 \\ 0 & 0 & 0 & c_4 & 0 & 0 \\ 0 & 0 & 0 & 0 & c_5 & 0 \\ 0 & 0 & 0 & 0 & 0 & c_6 \end{bmatrix}. \qquad (2.1.23)$$

The experimentally determined parameters $\alpha_x, \alpha_y, \alpha_z, c_1, c_2, c_3, c_4, c_5, c_6$ which determine the sheet's anisotropy are taken here as constants. It should be mentioned in Yld94 the parameters $\alpha_x, \alpha_y, \alpha_z$ are more generally functions of the stress state. The axes of material anisotropy are taken to coincide with the axes in Figure 2.1 (i.e. the rolling direction is aligned with the 1-direction), so the stress dependence of $\alpha_x, \alpha_y, \alpha_z$ is actuated only for strain paths with one positive and one negative principal strain (Barlat et al., 1997b). However, for these paths the influence of the yield surface anisotropy on the localization strain is not found to be significant (see also Butuc et al. (2003)), thus justifying our choice of using constant $\alpha_x, \alpha_y, \alpha_z$.

2.1.2.2 Electrical Constitutive Law

In addition to the mechanical an electrical constitutive response of the material is required. Here for simplicity an isotropic Ohm's law is assumed,

$$e_\alpha = r(\theta) j_\alpha, \tag{2.1.24}$$

where $r(\theta)$ is the resistivity of the isotropic sheet that is in general a function of temperature. This relation in addition to equation (2.1.7) allows equation (2.1.6) to be utilized (in addition to equation (2.1.4)) to find the currents j^B in the weak band.

One now has in equations (2.1.9)–(2.1.24) a complete description of the solid's constitutive response, where the necessary material constants are determined from experiments. An account of the material constant selection is given below.

2.1.3 Material Parameter Selection

Finding an alloy where all the relevant material parameters for the viscoplastic model in Sections 2.1.1 and 2.1.2 have been determined experimentally is a rather formidable task. A combination of AA6061-T6 and AA6016-T4 parameters seems the best available option for conducting a meaningful simulation. Constitutive parameters for AA6061-T6 are given by Yadav et al. (2001), based on experimental results by Yadav et al. (1995), and are presented in Table 2.1.

$\sigma_y = 276$ MPa	$E = 69$ GPa	$\epsilon_y = \sigma_y/E$
$n = 0.0741$	$m = 0.0870$	$\alpha = 0.5$
$\dot{\epsilon}_0^p = 1000$ s^{-1}	$\theta_0 = 298$ K	$\theta_m = 853$ K

Table 2.1: AA6061-T6 uniaxial response parameter values (Yadav et al., 2001)

Additional material parameters are required to implement equations (2.1.8) and (2.1.12). These parameters can be found from standard tables for aluminum (see also Triantafyllidis and Waldenmyer (2004)) and are presented in Table 2.2.

$\mu = 2700$ kg/m^3	$c_p = 896$ J/kg-K
$\chi = 0.9$	$r_0 = 2.65 \ 10^{-8}$ Ωm $\quad \eta = 2.3 \ 10^{-5}$ 1/K

Table 2.2: AA6061-T6 material parameter values (Triantafyllidis and Waldenmyer, 2004)

Values for the parameters describing the alloy's yield surface are also needed. Unfortunately, there is no information in the open literature regarding values for these parameters for AA6061-T6. This forces a compromise to be made, and these parameters are obtained from the closest available material data. Butuc et al. (2003) provides these data, which pertain to AA6016-T4, and the values for the corresponding parameters are given in Table 2.3.

$\alpha_x = 2.0$	$\alpha_y = 3.5$	$\alpha_z = 1.0$	
$c_1 = 1.0474$	$c_2 = 0.7752$	$c_3 = 1.0724$	$c_6 = 0.9288$

Table 2.3: AA6016-T4 yield surface parameter values (Butuc et al., 2003)

Triggering localized deformation requires an initial imperfection in the weak band, according to Marciniak and Kuczynski (1967) who first introduced this concept in predicting forming limit diagrams in the tensile region. Initially a thickness imperfection distinguished the weak band (e.g. Marciniak and Kuczynski (1967)), but imperfections in other material parameters were subsequently shown to be useful in predicting forming limits (e.g. Needleman and Triantafyllidis (1978)). Results of this method are sensitive to the magnitude of the imperfection. Alternative methods that do not utilize an imperfection have been proposed for rate-independent solids by Stören and Rice (1975) and for rate-dependent solids by Triantafyllidis et al. (1997). Unfortunately, the deformation theory approach proposed by Stören and Rice (1975) cannot be generalized for viscoplastic solids, while the perturbation method introduced by Triantafyllidis et al. (1997) produces unreasonable results for tensile loading (see Chapter II Appendix, Section 2.A).

For reasons discussed in detail in the Chapter II Appendix, the weak band method of Marciniak and Kuczynski (1967) has been adopted. A weakness in the yield stress σ_y is implemented using the imperfection parameter ξ such that $\sigma_y^B = (1 - \xi)\sigma_y^A$. In choosing a value for ξ simulated quasistatic (rate-independent, isothermal) forming limit curves using proportional straining paths and varying ξ values are considered. The sensitivity of these curves to ξ is most pronounced for biaxial stretching strain paths ($\epsilon_1 > 0$, $\epsilon_2 > 0$), while strain paths with one positive and one non-positive principal strain ($\epsilon_1 > 0$, $\epsilon_2 \leq 0$) show relatively little dependence on the value of the imperfection parameter. The resulting onset of necking curves are compared with the experimental quasistatic forming limit diagram for AA6061-T6, presented by LeRoy and Embury (1978). Requiring a value for ξ that gives the best overall agreement between simulated and measured forming limit curves resulted in the present choice of $\xi = 0.001$.

The issue of a temperature-dependent strain-rate sensitivity m needs also to be addressed. The constant value for m given in Table 2.1 does give a reasonable correlation with experimental constitutive data (Yadav et al., 2001), and this value will be used in the "base case" set of parameters. However, there is compelling evidence (see Krajewski (2005); Ogawa (2001)) that the strain-rate sensitivity is an increasing function of temperature, $m(\theta)$.

To obtain a reasonable estimate for $m(\theta)$, the work of Tirupataiah and Sundararajan (1994) and Ogawa (2001) is used. Tirupataiah and Sundararajan (1994) show a material-dependent transition strain rate between low strain-rate sensitivity and high strain-rate sensitivity. For aluminum with properties similar to AA6061-T6, the transition occurs at or below 100 s^{-1}; typical EMF strain rates are well above this. Thus, only data for strain rates above 100 s^{-1} are appropriate to fit a temperature-dependent strain-rate sensitivity for EMF processes. Ogawa (2001) provides stress versus strain rate data on AA6061-

T6 at 5% strain (or 6%, noted appropriately in the paper) for temperatures ranging from 77 K to 473 K and strain rates up to $1.5 \ 10^5 \ s^{-1}$. Equations (2.1.14) and (2.1.20) are used to find m at the different temperatures (m is assumed independent of strain rate); the quasistatic flow stress is adjusted to that indicated by Ogawa (2001) at each temperature (for the quasistatic case $\sigma = g(\epsilon^p, \theta)$ from equation (2.1.20)). Moreover, it is required that $m(\theta)$ match m constant at room temperature; a constant must be added to the functional dependence of m on θ implied by the data in Ogawa (2001). The following empirical relation is thus proposed (where θ is in degrees K)

$$m(\theta) = (1.40 \ 10^{-6})\theta^2 - (8.44 \ 10^{-4})\theta + 0.214, \qquad (2.1.25)$$

as the best fit for the above described experimental data (and therefore most appropriate in the temperature range 77 K $\leqslant \theta \leqslant$ 473 K).

2.1.4 Strain, Strain Rate, and Current Density Profiles

A proportional straining path is the standard assumption for the calculation of FLD's, i.e. $\epsilon_2 = \rho \epsilon_1$ with ρ a constant such that $-1/2 \leqslant \rho \leqslant 1$. A uniaxial stress state occurs for $\rho = -1/2$ while $\rho = 1$ represents an equibiaxial plane stress state. However, in contrast to the quasistatic forming case of rate-independent solids where the FLD is independent of the strain history $\epsilon_1(t)$, the present calculations on an electromagnetically formed viscoplastic solid need a time-dependent strain profile $\epsilon_1(t)$, in addition to a time-dependent current density profile $j_1(t)$. The strain, strain rate, and current density profiles are motivated by the ring calculations of Triantafyllidis and Waldenmyer (2004).

Therefore, since the principal hoop strain rate is shaped as a smooth pulse, a sinusoidal strain rate pulse is assumed for simplicity. Hence for a pulse of duration $4\tau_0$ the principal strains are taken to be

$$\epsilon_1(t) = \frac{\epsilon_{max}}{2}\left[1 - \cos\left(\frac{\pi t}{4\tau_0}\right)\right], \quad \epsilon_2(t) = \rho \epsilon_1(t), \qquad (2.1.26)$$

which gives for the corresponding strain rate

$$\dot{\epsilon}_1(t) = \frac{\pi \epsilon_{\max}}{8\tau_0} \sin\left(\frac{\pi t}{4\tau_0}\right). \tag{2.1.27}$$

The maximum principal strain, $\epsilon_{\max}$, and the characteristic time, τ_0, are variables of the simulation to be subsequently specified.

The effect of implementing the simplified strain profile above is investigated by comparison with a linear time-dependent strain profile. Again for a pulse duration of $4\tau_0$, the linear strain profile is taken as

$$\epsilon_1(t) = \frac{\epsilon_{\max}}{4\tau_0} t, \quad \epsilon_2(t) = \rho \epsilon_1(t), \tag{2.1.28}$$

which gives a constant corresponding strain rate

$$\dot{\epsilon}_1(t) = \frac{\epsilon_{\max}}{4\tau_0}. \tag{2.1.29}$$

Here for comparison purposes $\epsilon_{\max}$ and τ_0 are equal to those in the sinusoidal strain profile.

Due to the electromagnetic nature of the process, knowledge of the principal current flowing through the sheet is also necessary. Keeping in mind the ring simulations (Triantafyllidis and Waldenmyer, 2004) and the fact that in tube bulging only a current in the hoop direction occurs, with a pulse duration typically half of the strain pulse duration, the following sinusoidal form of the principal current density is adopted for simplicity

$$j_1(t) = J_{\max} \sin\left(\frac{\pi t}{2\tau_0}\right), \quad j_2(t) = 0, \quad j_i = 0 \text{ for } t > 2\tau_0, \tag{2.1.30}$$

where $J_{\max}$ is the maximum principal current density. It is also assumed that no backward current is allowed to flow, so that for $t > 2\tau_0$, $j_1 = j_2 = 0$. Although the exact nature of the strain and current density time profiles depends on the solution of the coupled electromagnetic and thermomechanical boundary value problem for the relevant experiment, the

profiles chosen above are good approximations of the calculated profiles of the EMF ring work (Triantafyllidis and Waldenmyer, 2004) thus justifying the simplifying assumptions of equations (2.1.26), (2.1.27) and (2.1.30).

To complete these profiles, some physically motivated values for τ_0, $\epsilon_{\max}$ and $J_{\max}$ must be selected. As defined in equations (2.1.26)–(2.1.30) τ_0 is one quarter of the total forming time, which equals the time to the electric current's first maximum. This definition is motivated by the work of Triantafyllidis and Waldenmyer (2004), where τ_0 is the time to the first maximum of the electric current in the forming circuit in isolation (without a workpiece). The fully coupled results show a similar time to the electric current's first maximum, and the total forming time is approximately $4\tau_0$. In the present work this characteristic time in combination with $\epsilon_{\max}$ determines the forming rate (see equation (2.1.27)). Without a fully coupled EMF boundary value problem simulation, $\epsilon_{\max}$ must be specified a priori. The value of $\epsilon_{\max}$ needs to be greater than the EMF necking strain for all materials and processes of interest, but it should be reasonable as well. If $\epsilon_{\max}$ is chosen high, τ_0 must be large to keep the applied strain rate similar to EMF rates. The method in the present work takes $\epsilon_{\max}$ as a constant (regardless of the strain path ρ), with value $\epsilon_{\max} = 0.8$ which is greater than all of the necking results found here.

With $\epsilon_{\max}$ specified, the strain and strain rate profiles need only τ_0 to be complete. An appropriate value is found by appealing to a property of the viscoplastic material model, namely its overstress ζ. Due to the dynamic nature of an EMF process, the workpiece experiences higher flow stresses than it would in a quasistatic process at identical strains and temperatures. The amount by which the flow stress exceeds the quasistatic flow stress is the overstress, defined as

$$\zeta \equiv \frac{\sigma_e(\sigma_{ij})}{g(\epsilon^p, \theta)} - 1. \tag{2.1.31}$$

Assuming the material constitutive response is fully defined, ζ can be related to the strain

rate through equation (2.1.14). Specifically, assuming a uniaxial process for simplicity and that $\dot{\epsilon}^p = \dot{\epsilon} = \dot{\epsilon}_1$ (a reasonable assumption at the large strains inherent in EMF processes), one has

$$\frac{\dot{\epsilon}_1}{\dot{\epsilon}_0^p} = \left((1 + \zeta)^{1/m(\theta)} - 1\right). \tag{2.1.32}$$

The maximum strain rate implies

$$\tau_0 = \frac{\pi \epsilon_{\max}}{8 \dot{\epsilon}_0^p} \left((1 + \zeta_{\max})^{1/m(\theta)} - 1\right)^{-1}. \tag{2.1.33}$$

Thus given an appropriate value of maximum overstress $\zeta_{\max}$, τ_0 is specified; since both m and $\dot{\epsilon}_0^p$ influence the time scale of a process, $\zeta_{\max}$ is chosen to give a physically meaningful forming speed. The value $\zeta_{\max} = 0.15$ is therefore the base case in all subsequent calculations.

Finally, the value for $J_{\max}$ is chosen by considering the temperature increase needed to cause melting. From equation (2.1.8), the temperature increase of the material is due to two sources: plastic work and ohmic heating. As shown in the ring simulations (Triantafyllidis and Waldenmyer, 2004), by the end of the forming process the dissipation of the plastic work and specimen ohmic heating are comparable. This allows the following approximation to equation (2.1.8)

$$\mu c_p \dot{\theta} = 2r(\theta) \left(j_\alpha j_\alpha\right). \tag{2.1.34}$$

From equation (2.1.30) the time-dependent form of the electric current is known, and equation (2.1.34) may be integrated with respect to time if $r(\theta)$ is taken as constant, an assumption that will subsequently be used throughout the simulations. Integrating equation (2.1.34) from $t = 0$ to $t = 4\tau_0$ gives

$$J_{\max} = \left(\frac{\mu c_p (\theta - \theta_0)}{2r\tau_0}\right)^{1/2}. \tag{2.1.35}$$

If one takes $\theta = \theta_m$, $J_{\max}$ from equation (2.1.35) is such that melting occurs at the end of the simulation, i.e.

$$J_{\text{melt}} = \left(\frac{\mu c_p (\theta_m - \theta_0)}{2 r \tau_0} \right)^{1/2}. \tag{2.1.36}$$

To avoid melting $J_{\max}$ must be lower than J_{melt}, and a reasonable value for EMF processes is $J_{\max} = 0.15 J_{\text{melt}}$. This value, along with $\epsilon_{max} = 0.8$ and τ_0 from equation (2.1.33), completes the base case forming conditions for the present simulations, and the result of the above analysis is $\tau_0 = 78.8 \ \mu\text{sec}$, $J_{\max} = 2.69 \ 10^9 \ \text{A/m}^2$ and a maximum forming speed of 3989 s^{-1}.

2.2 Forming Limit Results

The goal of the present section is to present an application of the general theory proposed in the previous section. Following the description of the numerical solution algorithm, the section proceeds with the calculation of the FLD for the "base case" alloy and the investigation of its dependence on the various material properties and loading parameters.

2.2.1 Assumptions and Numerical Implementation

In the interest of simplicity it is assumed that the material is incompressible. For the large strains encountered during the EMF process, this assumption is quite reasonable since compressibility effects in metals – due to elastic distortion and thermal strain of their crystals – are an insignificant part of the overall plasticity dominated deformation. Consequently, the total strain rate is decomposed into traceless elastic D_{ij}^e ($D_{ii}^e = 0$) and plastic D_{ij}^p ($D_{ii}^p = 0$) parts, the first property requiring a poisson ratio $\nu = 0.5$ and the second property guaranteed for yield functions which are independent of the first invariant of the stress σ_{ii}.

With these simplifying assumptions in place, the governing equations are cast as a system of first order ODE's. These ODE's are solved using a fourth order Runge-Kutta algorithm. For the solution outside the band only the adiabatic heating equation (2.1.8) and the constitutive equations are required, i.e. one has

$$\dot{\boldsymbol{x}}^A = f_A(\boldsymbol{x}^A, t), \ \boldsymbol{x}^A \equiv [\sigma_1^A, \sigma_2^A, \epsilon_A^p, \theta^A] \tag{2.2.1}$$

where σ_1^A and σ_2^A are Cauchy principal stresses. Inside the localized band, the four continuity equations (2.1.1), (2.1.2), (2.1.4) and (2.1.6) give six scalar equations, which in addition to energy balance equation (2.1.8) and the four constitutive equations detailed in Section 2.1.2 (three for the in-plane stresses $\sigma_{\alpha\beta}$ and one for the internal variable ϵ^p) can completely determine the eleven variable electromechanical state inside the band ($F_{\alpha\beta}$ (4), $\sigma_{\alpha\beta}$ (3), j_α (2), ϵ^p (1), θ (1)) in terms of the known counterpart field quantities outside the band. Note, the j_i^B are obtained directly (without recourse to ODE's) from equations (2.1.4)–(2.1.7), while due to the incremental nature of plasticity calculations, the rate forms of equations (2.1.1) and (2.1.2) are required. Once again, the resulting equations are cast as a system of first order ODE's

$$\dot{\boldsymbol{x}}^B = f_B(\boldsymbol{x}^B, t), \ \boldsymbol{x}^B \equiv [\sigma_{11}^B, \sigma_{12}^B, \sigma_{22}^B, F_{11}^B, F_{21}^B, F_{12}^B, F_{22}^B, \epsilon_B^p, \theta^B], \tag{2.2.2}$$

where the t-dependent terms in $f_B(\boldsymbol{x}^B, t)$ are functions of $\boldsymbol{x}^A$.

The numerical localization calculations require establishing a necking criterion. Localization occurs when ϵ_B^p becomes unbounded for a finite value of ϵ_A^p, which is numerically implemented as when $\dot{\epsilon}_B^p / \dot{\epsilon}_A^p > 10$. The value 10 is chosen arbitrarily but is adequately large to have a negligible effect on the calculated necking strain. The necking of the imperfect sheet depends on the angle Φ of the imperfection in the reference configuration (see Figure 2.1), which can take any value $0 \leqslant \Phi < \pi/2$. The value that minimizes the necking strain outside the band gives the sought forming limit strains. One

must therefore test through the entire $[0, \pi/2)$ range of band angles (satisfactory accuracy is obtained using increments of $\pi/180$) for each load path ρ, and this results in $\Phi = 0$ for $0 \leqslant \rho \leqslant 1$ but $\Phi \neq 0$ for $-1/2 \leqslant \rho < 0$.

Finally, numerical precision of the localization strain calculations must be checked. First, the quasistatic case has an analytical solution for $\rho = 0$ and $\beta = 2$ (isotropic J_2 flow theory of plasticity) of ϵ_{neck} obtained at the maximum of the nominal stress. Using $\xi = 0.001$ and an adequately small time step (see below) the analytical solution is recovered. Second, for both the quasistatic and rate-dependent cases the time step, Δt, is chosen by requiring less than 0.001 change in necking strain for any Δt decrease. This results in the nondimensional time steps $\Delta t/\tau_0 \approx 3 \; 10^{-7}$ for the quasistatic process and $\Delta t/\tau_0 \approx 2 \; 10^{-5}$ for the EMF processes.

2.2.2 Forming Limit Diagrams

The numerically calculated FLD's are presented in Figures 2.2 through 2.11. More specifically, the influence of material properties is presented in Figures 2.2–2.7, while the influence of various loading parameters is given in Figures 2.8–2.11.

The effect of EMF on the FLD is presented in Figure 2.2, with six forming limit curves, three each for EMF and quasistatic forming conditions (quasistatic results are obtained from the dynamic simulation by imposing a low forming speed, minimal strain-rate sensitivity, and an isothermal process). For each one of the three yield surfaces presented in Section 2.1.2.1 there are two FLD curves, one for an EMF process and one for its quasistatic counterpart. Use of an EMF process results in a significant increase in forming limit strains as compared to a quasistatic one of the same ρ, and the increase is dependent on the yield surface. This dependence is important in the $\rho > 0$ region, while $\rho \leqslant 0$ shows negligible influence of the yield surface choice. Notice that the
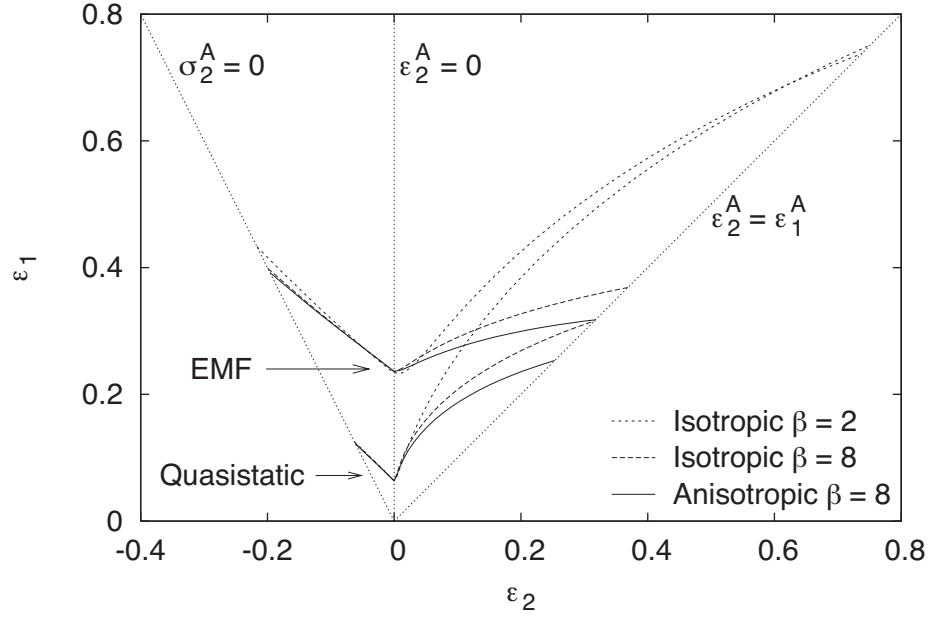
Figure 2.2: Comparison of EMF versus quasistatic forming limit curves for an alloy with a given uniaxial response for three different yield surfaces.

necking strains for the isotropic $\beta = 2$ surface (von Mises) are unrealistic even for the quasistatic loading. The reason is the low curvature of the yield surface, in particular near $\rho = 1$, a known deficiency of flow theory models (see discussion in Stören and Rice (1975)). Of the three yield surface models considered here, the anisotropic nonquadratic surface, Yld94, is the best choice based on comparison with the experimental quasistatic FLD presented in LeRoy and Embury (1978). Hence in all subsequent calculations the Yld94 model is used. From the curves generated with this yield surface, the EMF process provides between a 25% ($\rho = 1$) and 225% ($\rho = -1/2$) increase in forming limits over a quasistatic process.

The necking angle ϕ_{neck} of the weak band (where ϕ is the angle of the band in the current configuration related to its reference configuration counterpart Φ by $\tan(\phi) = \tan(\Phi)\exp(\epsilon_2 - \epsilon_1)$) is plotted for the base case EMF process against the strain ratio $\rho = \epsilon_2/\epsilon_1$ in Figure 2.3a. For $\rho \geqslant 0$, $\phi_{\mathrm{neck}} = 0$, while for $\rho < 0$, $\phi_{\mathrm{neck}} \neq 0$; ϕ_{neck}

approaches 40 degrees as $\rho \to -1/2$. These values of ϕ for both $\rho < 0$ and $\rho \geqslant 0$ mirror known quasistatic results (see Hill (1952); Stören and Rice (1975)), indicating that ϕ_{neck} is insensitive to EMF processes.

In order to give an idea of a typical temperature increase due to the application of an EMF process the temperatures at the onset of necking for the base case EMF process, both outside (θ^A) and inside (θ^B) the weak band, are shown in Figure 2.3b plotted against the strain ratio $\rho = \epsilon_2/\epsilon_1$. A temperature rise between 30 K and 80 K in the sheet (A) is predicted, with the minimum at $\rho = 0$ and the maximum at $\rho = 1$. Moreover, there is a significant temperature difference between the sheet (A) and weak band (B) due to higher plastic strain rate and higher current density. The ramifications of this additional rise in temperature inside the band will be discussed subsequently.

Figure 2.4 shows the influence on necking of the speed of the EMF process, with the quasistatic (QS) forming limits shown for comparison. Changing the loading speed is equivalent to changing the nondimensional time scale $\dot{\epsilon}_0^p \tau_0$, which for consistency (since m also controls viscosity) is driven by the maximum overstress ζ_{max} as discussed in Section 2.1.4. Increasing ζ_{max} corresponds to increasing the forming speed, which results in higher necking strains as expected from the material's viscosity. The increase in ductility due to EMF effect is greatest for $\rho < 0$, where the forming limit curve shifts up, and decreases with increasing ρ.

The influence of the hardening exponent n is shown in Figure 2.5. An increase in n is known to increase the forming limits for a quasistatic process (e.g. Stören and Rice (1975)), and the same influence is seen here for an EMF process. The increase in necking strains is found for both $\rho < 0$ and $\rho \geqslant 0$, with the minimum increase occurring at $\rho = 1$. Moreover with the values of n considered here $0 \leqslant n \leqslant 0.25$, there is a parallel shift in the forming limit curves for $\rho < 0$. For $\rho > 0$ with small values of n the necking strains
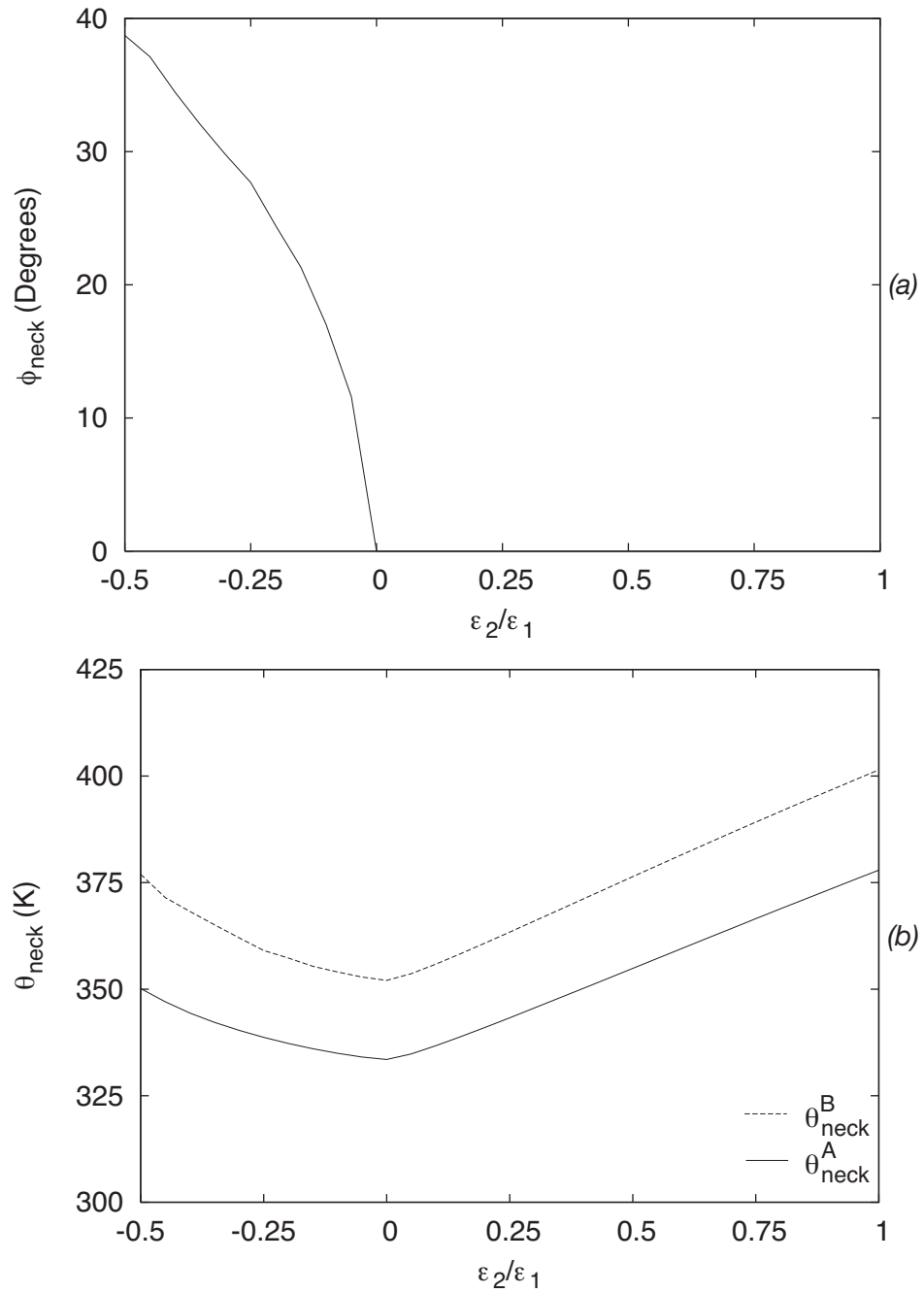
Figure 2.3: a) Angle of the weak band in the current configuration at the onset of necking ϕ_{neck} versus principal strain ratio ρ for the base case EMF process. b) Temperature at the onset of necking θ_{neck} as a function of the principal strain ratio ρ both outside (A) and inside (B) the weak band for the base case EMF process.
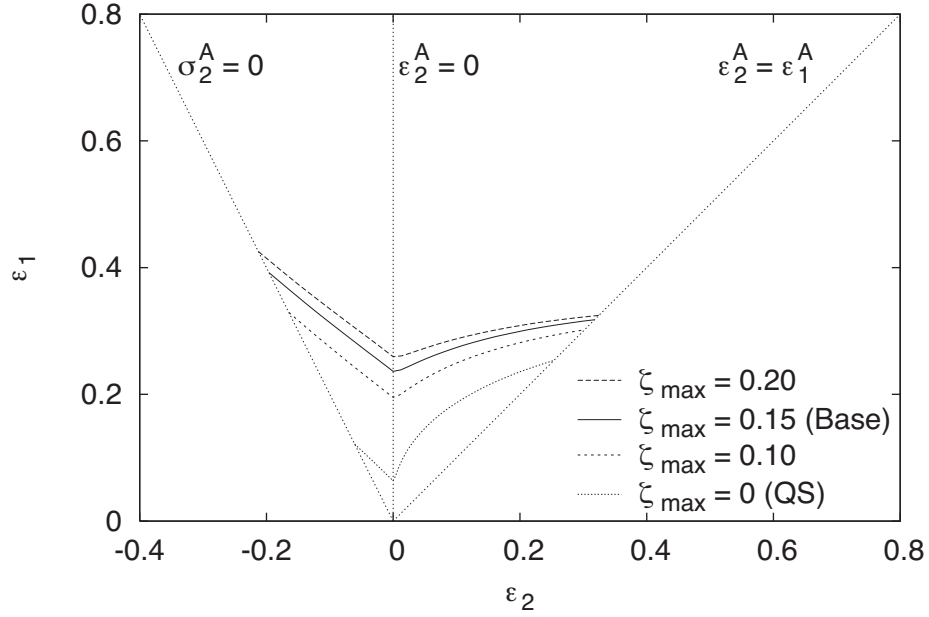
Figure 2.4: Influence of the process's characteristic time τ_0 (based on the resulting maximum overstress $\zeta_{\max}$) on the forming limit curve.

increase with increasing ρ while for large values of n this trend is reversed, with ϵ_{neck} decreasing for increasing ρ.

Figure 2.6 shows the influence on ductility of the strain-rate sensitivity exponent m. As expected from the thermally insensitive case (see Hutchinson and Neale (1977)), the forming limits increase with increasing m, with the minimum ductility increase occurring at $\rho = 1$. Here the influence of m is calculated for a fixed maximum strain rate (i.e. $\dot{\epsilon}_0^p \tau_0$ fixed), which implies that the pulse time for all experiments remains fixed.

The effect of the temperature sensitivity exponent α is presented in Figure 2.7. Recall that for temperature sensitive solids an increase in temperature reduces the flow stress, i.e. weakens the material. From equations (2.1.14) and (2.1.20) it also follows that a lower α indicates stronger temperature sensitivity. Since the weak band receives more heating than the sheet (see Figure 2.3b) through additional plastic work and higher current densities, consequently an increased temperature sensitivity weakens the band more in
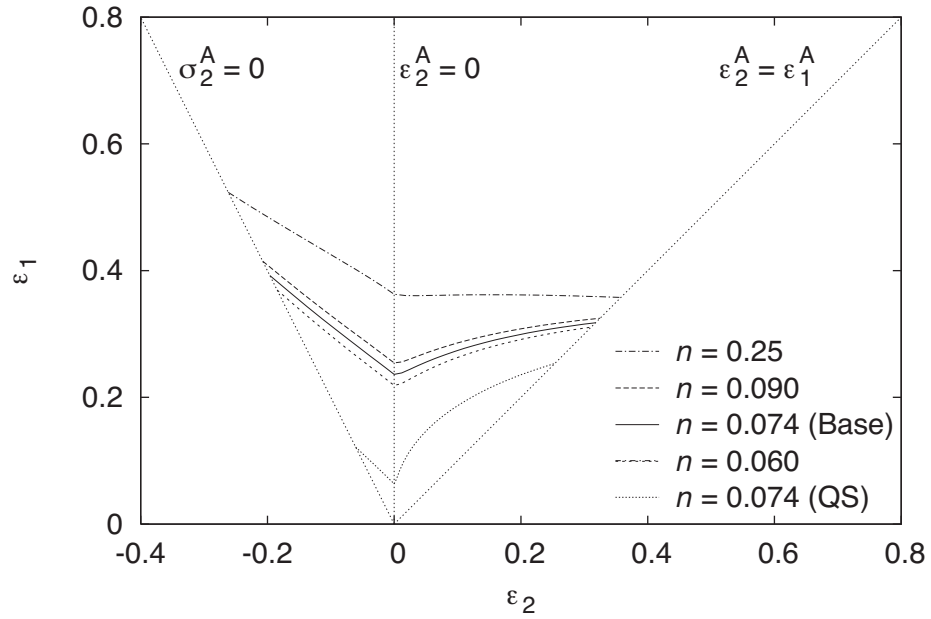
Figure 2.5: Influence of the hardening exponent n on the forming limit curve.
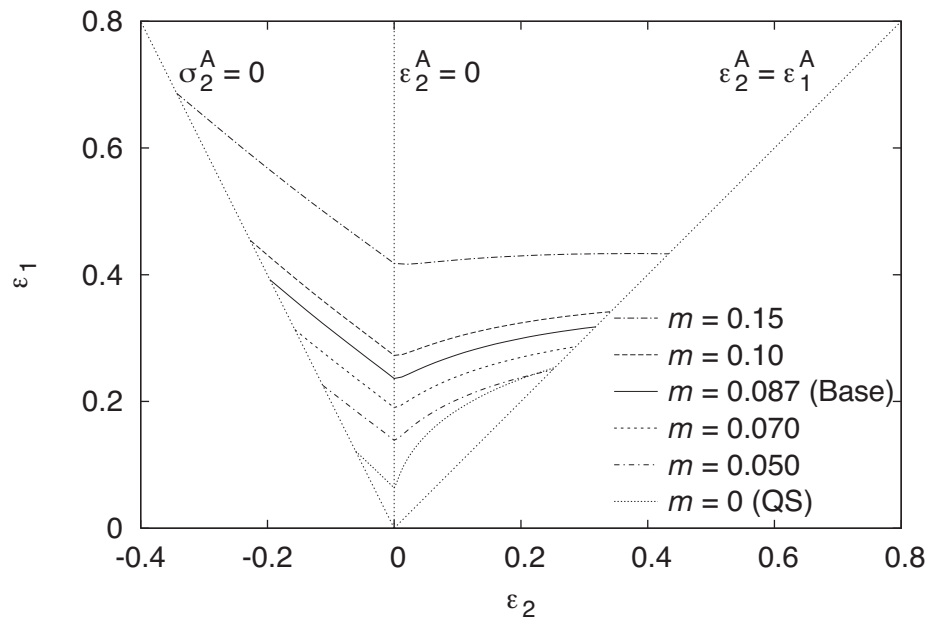
Figure 2.6: Influence of the rate sensitivity exponent m (with nondimensional time scale $\dot{\epsilon}_0^p \tau_0$ kept constant) on the forming limit curve.
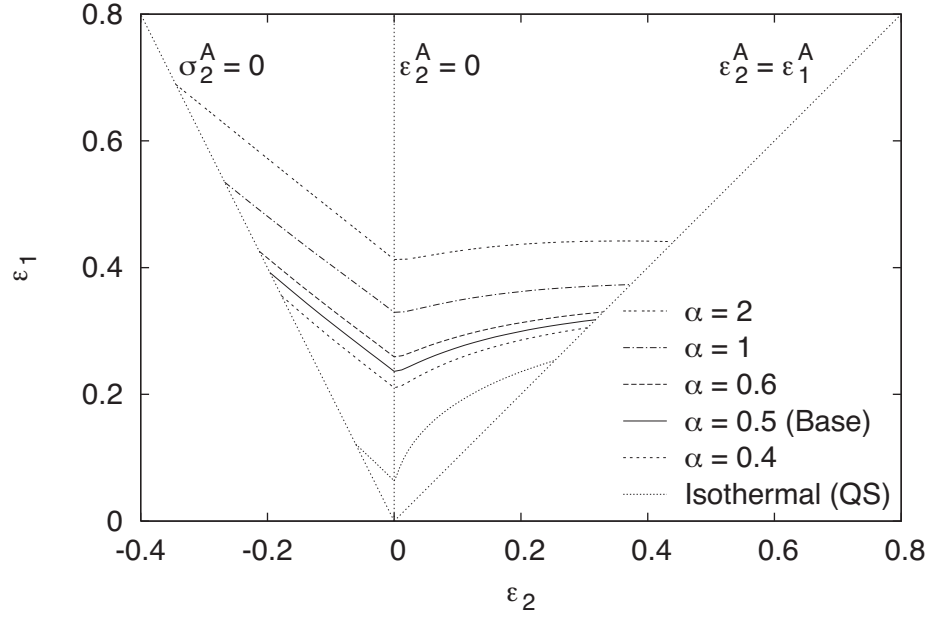
Figure 2.7: Influence of the temperature sensitivity exponent α on the forming limit curve.

relation to the sheet, which encourages necking. This mechanism explains why a decrease in α (*i.e* an increase in temperature sensitivity) causes a decrease in the forming limits for all values of ρ.

In Figure 2.8 is shown the influence of the initial temperature θ_i on the FLD. The sheet and weak band in all cases have the same initial temperature; the base case initial temperature is the reference temperature $\theta_0 = 298$ K. The form of the uniaxial response, equations (2.1.14) and (2.1.20), indicates that an increase in temperature makes the flow stress, for subsequent temperature changes, less temperature sensitive for $\alpha < 1$, equally temperature sensitive for $\alpha = 1$ and more temperature sensitive for $\alpha > 1$. Also, Figure 2.7 indicates that the forming limits increase with decreasing temperature sensitivity. These observations explain the influence of θ_i on the forming limits. In particular, $\alpha = 1$ shows negligible dependence on θ_i, while calculations with thermal sensitivity values $\alpha = 0.5$ and $\alpha = 2$ indicate that for increasing θ_i forming limits for $\alpha < 1$ increase and forming limits for $\alpha > 1$ decrease.
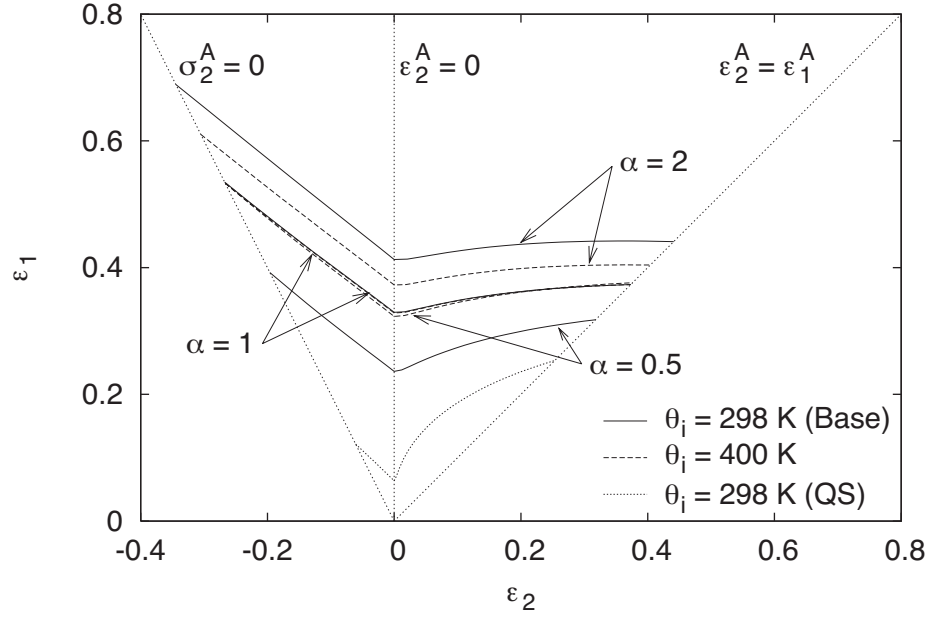
Figure 2.8: Influence of initial temperature θ_i on the forming limit curve for three different thermal sensitivity exponents.

Figure 2.9a presents the influence of the electric current density on the FLD. Plastic dissipation produces two orders of magnitude more temperature difference between weak band and sheet than ohmic dissipation in the base case EMF process. This indicates the electric current primarily heats the workpiece uniformly (i.e. the same amount inside and outside the band), and by the results in Figure 2.8 one expects increased forming limits with increased electric current. However, as J_{max} approaches J_{melt} the temperature difference (between weak band and sheet) due to ohmic dissipation approaches that of plastic dissipation. For large J_{max} ohmic dissipation has a strong negative influence on the forming limits since an increased temperature difference encourages necking. The result is the upper bound on the forming limits for increasing J_{max} observed in Figure 2.9a.

In Figure 2.9b the temperature difference between weak band and sheet $\theta^B - \theta^A$, for the cases $J_{max} = 0.15J_{melt}$, $J_{max} = 0.50J_{melt}$ and $J_{max} = 0.70J_{melt}$, is plotted with respect to nondimensional time t/τ_0 for the strain path $\rho = 0$. To illustrate the mechanism behind
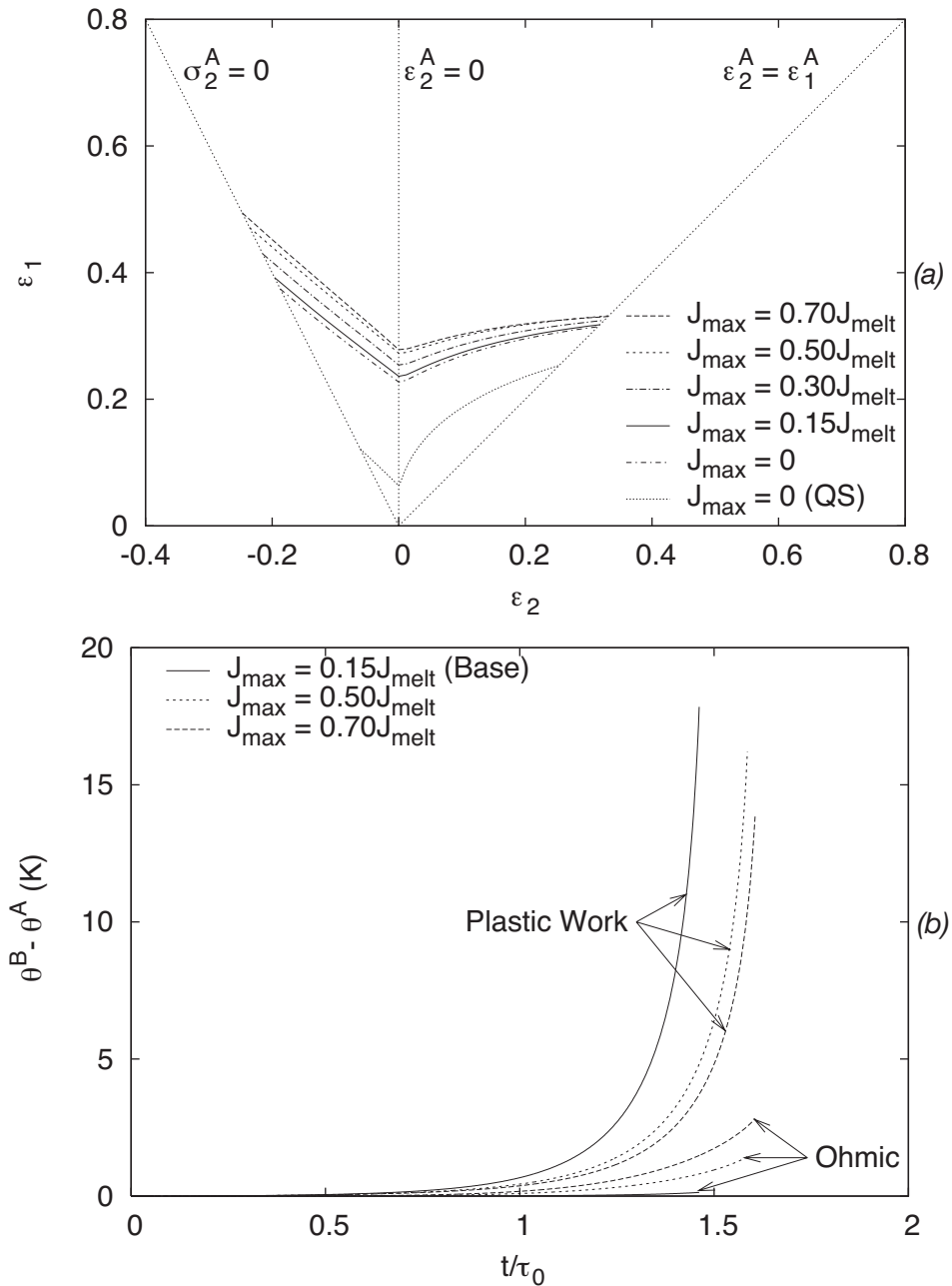
Figure 2.9: a) Influence of electric current density J_{max} on the forming limit curves for constant rate sensitivity exponent m. b) Influence of electric current density J_{max} on the temperature difference between weak band (B) and sheet (A) for constant rate sensitivity exponent m. The temperature differences due to ohmic heating and plastic work are calculated separately.

the upper bound on the forming limits for increasing J_{max}, the temperature difference is divided into a part due to plastic dissipation and a part due to ohmic dissipation. As J_{max} increases the plastic dissipation difference between zones A and B is reduced while the corresponding difference in ohmic dissipation dramatically increases due to thinning of the weak band and the subsequent electric current density increase. Between $J_{max} = 0.50J_{melt}$ and $J_{max} = 0.70J_{melt}$ these two influences add to produce minimal change in $\theta^B - \theta^A$; this correlates with negligible change in the forming limits (see Figure 2.9a). The increased $\theta^B - \theta^A$ due to unequal ohmic heating encourages necking and counteracts the uniform temperature increase that delays necking (see Figure 2.8).

Figure 2.10 shows the results of implementing a temperature-dependent strain-rate sensitivity $m(\theta)$ as described by equation (2.1.25). Since the strain-rate sensitivity increases with temperature, its effect overrides the influence of the ohmic dissipation. The forming limits thus behave monotonically with respect to the electric current. This indicates the temperature dependence of the strain-rate sensitivity strongly influences the FLD for EMF processes.

The influence of the strain profile on necking is presented in Figure 2.11. The sinusoidal base case profile (equations (2.1.26) and (2.1.27)) is compared with the simple linear profile (equations (2.1.28) and (2.1.29)), where ϵ_{max} and τ_0 are kept at the base case values for both profiles. Figure 2.11 shows the profile has little influence on the forming limits, and this further supports the use of equations (2.1.26) and (2.1.27) as a reasonable approximation to the actual strain profile encountered during an EMF process.

Figures 2.2–2.11 illustrate how the electromagnetic forming process enhances sheet ductility. The effects of material properties and EMF process characteristics have been examined in detail.
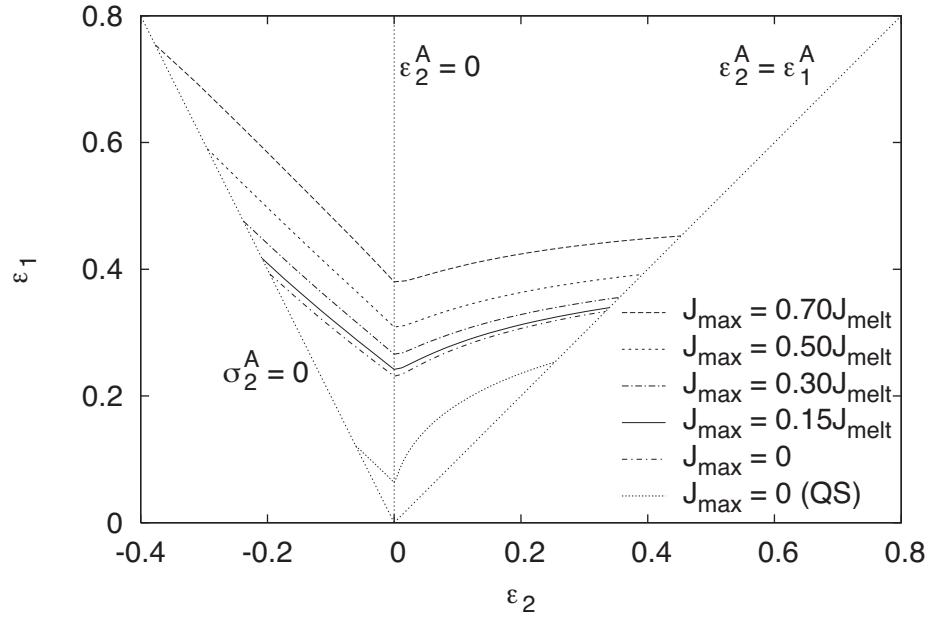
Figure 2.10: Influence of electric current density J_{max} on the forming limit curves for a temperature-dependent strain-rate sensitivity $m(\theta)$.
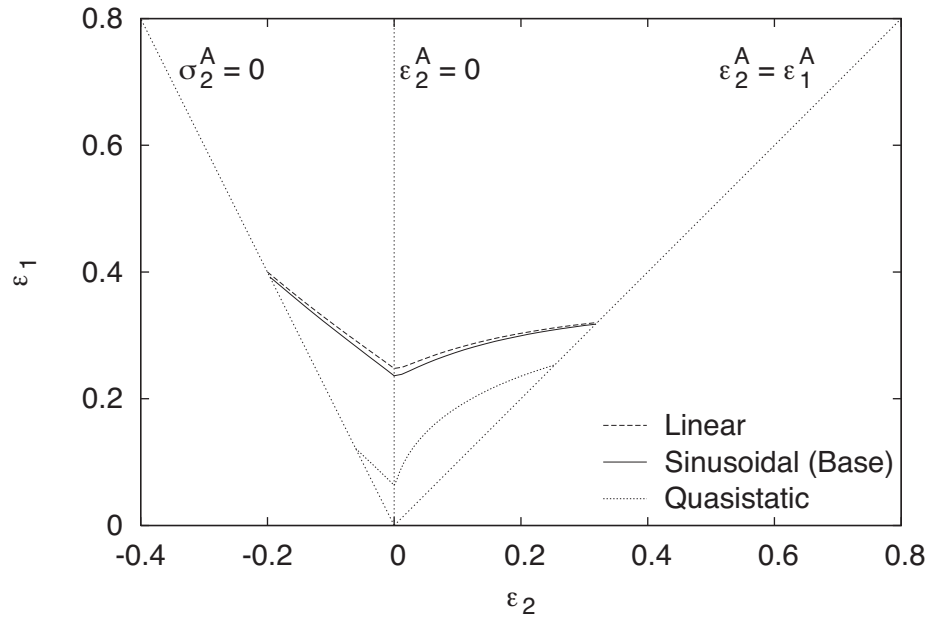
Figure 2.11: Influence of the assumed strain profile on the forming limit curve.

2.3 Experimental Comparisons

The work of this section pertains to the comparison of simulations based on the formulation discussed previously in Section 2.1 to experimental data obtained from a series of experiments on electromagnetically expanded aluminum alloy tubes. Section 2.3.1 gives a discussion of the experimental procedure, the selection of material properties for the AA6063-T6 tube alloy and a description of the strain and current density profiles. In Section 2.3.2 four different experiments are presented and compared to the corresponding theoretical simulations.

2.3.1 Experimental Problem Formulation

The general theory of the EMF-based FLD has been discussed previously and is here specialized to electromagnetic tube expansion experiments. The experimental procedure is first discussed, followed by the presentation of temperature-dependent viscoplastic constitutive models for the tube sheet. The formulation is completed by introducing the strain and current profiles adopted for modeling the EMF process.

2.3.1.1 Experimental Procedure

Figure 2.12 shows a schematic of the set-up for the electromagnetic tube expansion experiments. It consists of a capacitor bank connected to a solenoid actuator placed inside an aluminum alloy tube. The experiments are conducted using a commercial Maxwell Magneform capacitor bank with a maximum stored energy of 16 kJ. The energy is stored in 8 capacitors, each with a capacitance of 53.25 μF. The system has a maximum working voltage of 8.66 kV. Both the number of capacitors and charging voltage can be adjusted to control the discharged energy. One Rogowski probe, R1 in Figure 2.12, is used to measure the primary current. A second such probe, R2 in Figure 2.12, measures the
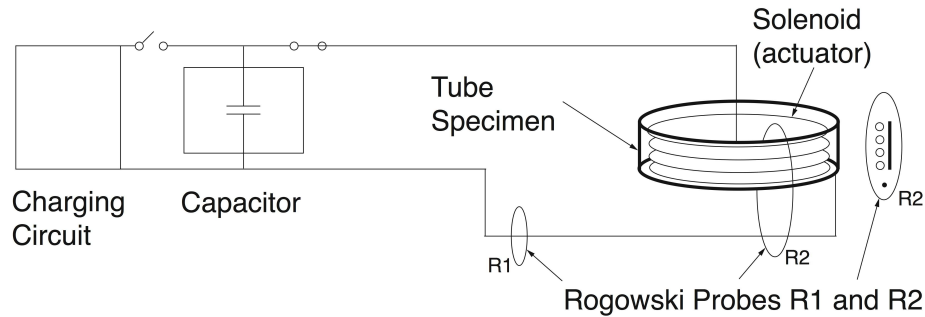
Figure 2.12: Schematic representation of the experimental set-up for electromagnetic expansion of tubes.

aggregate coil current, which is the product of the number of coil turns and the primary current, combined with the induced current in the tube.

Figure 2.13a shows one of the bare coils fabricated by commercial spring winding from 6.35 mm diameter ASTM B16 brass wire. Two coils are used in these experiments, one with four turns (as shown in Figure 2.13a) and an otherwise identical coil with ten turns. Both coils have an outer diameter of 54 mm and pitch of 9.4 mm. The wire is covered with heat shrink-wrap tubing to provide insulation and then potted in urethane. Figure 2.13b shows the actual experimental configuration with an aluminum alloy tube sample fitted over the epoxy-coated coil. The tube samples are AA6063-T6 aluminum alloy with an inner diameter of 57 mm and a wall thickness of 1.75 mm. The outer surface of each tube is electrolytically etched with a pattern of 2.5 mm diameter circles in order to measure the strain in the expanded samples.

For each combination of coil and sample size, multiple samples are expanded with incrementally increasing discharge energies until an energy level sufficient to initiate necking and/or fracture of the tube is reached. Major and minor limit strains are then measured from the deformed circles in areas where necking occurs, labeled "Unsafe", and in areas where no necking or failure is evident, labeled "Safe." Figure 2.14 shows a sample deformed tube for each of the four possible combinations of tube length and coil
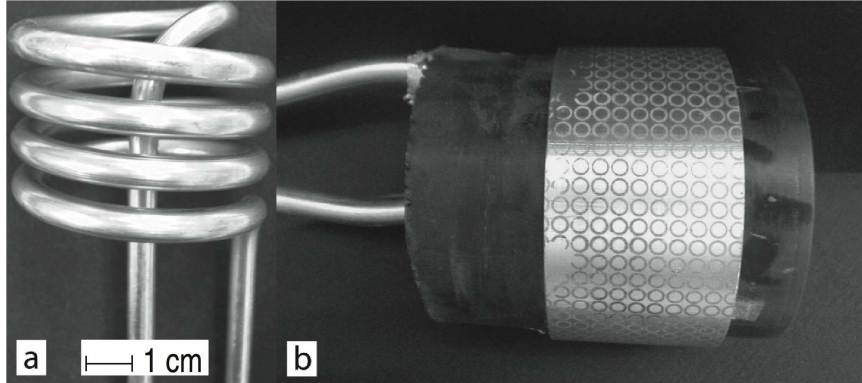
Figure 2.13: a) The bare 4-turn coil. b) Sample-actuator configuration. The 31.7 mm tall aluminum tube sample is shown fitted around the urethane-coated 4-turn coil.

length. The short coil is approximately the same length, 31.7 mm, as the short tubes; the long coil is about the same length, 85.1 mm, as the long tubes. In Figure 2.14, tubes (a) and (b) are short while tubes (c) and (d) are long, and tubes (a) and (c) are deformed using a 4-turn coil while tubes (b) and (d) are deformed using a 10-turn coil. The data gathered will subsequently be compared with the onset of necking calculations described above. Full details of these experiments are published in Seth (2006).

In addition, data on the tube material's uniaxial quasistatic stress-strain response are gathered using an MTS machine. Samples are cut from the AA6063-T6 tubes according to the ASTM tensile sample standard (0.630 cm wide, 2.54 cm long) by water jet. Tests are conducted at a strain rate of 3.3 10^{-3} s^{-1}, and the uniaxial quasistatic stress-strain response in equation (2.1.20) (with constant temperature $\theta = \theta_0$) is fit with data corresponding to a sample cut longitudinally from the tube (transverse samples are omitted since the curvature of the tube requires substantial straightening for them, altering the material's behavior in the test). Figure 2.15 gives a comparison of the experimental data and analytical fit. The resulting material parameters are detailed below.
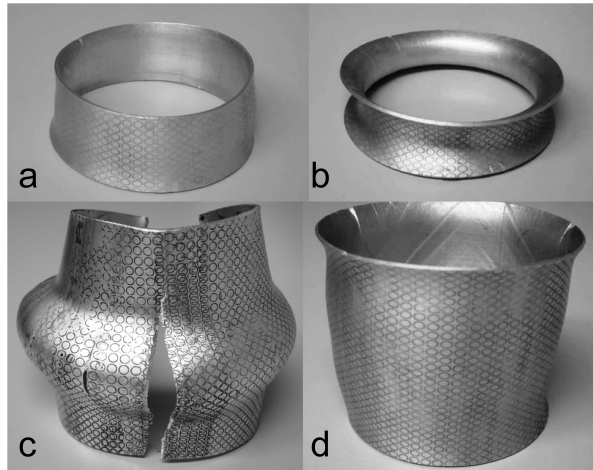
Figure 2.14: Final configuration showing localized necking of tubes deformed using the experimental EMF setup. a) 31.7 mm tube deformed with 4-turn coil. b) 31.7 mm tube deformed with 10-turn coil. c) 85.1 mm tube deformed with 4-turn coil. d) 85.1 mm tube deformed with 10-turn coil.
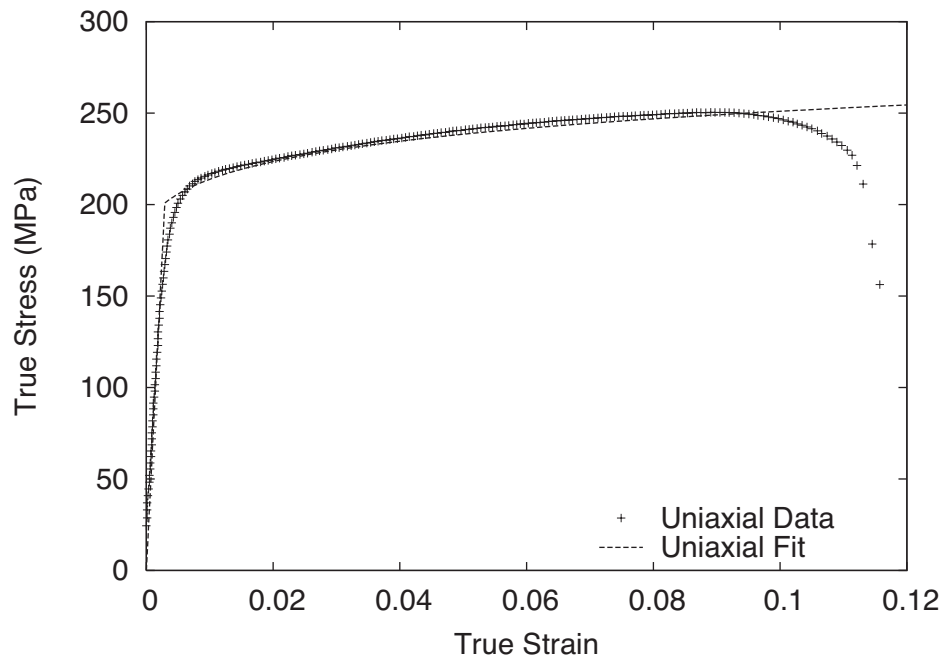
Figure 2.15: AA6063-T6 uniaxial quasistatic stress-strain response: experimental data and corresponding theoretical fit.

2.3.1.2 Selection of Material Constants

The electromagnetically expanded tubes are made of AA6063-T6, a tube alloy. How-ever, material constants required for the determination of the quasistatic FLD are obtained from experiments using flat sheet blanks. In addition, an independent measurement of rate and thermal sensitivity parameters, at the strain rates and temperatures of interest, requires highly specialized equipment that is not available to us. The strategy adopted to address these issues is to use uniaxial quasistatic test measurements from AA6063-T6 to obtain the values of Young's modulus E, yield stress σ_y, and hardening exponent n and to rely on existing independent experiments on a closely related alloy, AA6061-T6, for which the remaining required material parameters have been published in the open literature. From uniaxial tests on thin strips cut longitudinally from AA6063-T6 tubes, the best fit (see Figure 2.15) is achieved using the values in Table 2.4.

$$ E = 69 \text{ GPa} \quad \sigma_y = 190 \text{ MPa} \quad \epsilon_y = \sigma_y/E \quad n = 0.0769 $$

Table 2.4: Material parameters from AA6063-T6

The remaining parameters are obtained from different sources. The rate and thermal sensitivity related parameters are based on experiments by Yadav et al. (1995, 2001) and are given in Table 2.1.

The mass density, thermal and electrical properties are obtained from standard refer-ences on aluminum (they are not alloy sensitive) and are given in Table 2.2. The value of the plastic work conversion factor χ is the same as in Triantafyllidis and Waldenmyer (2004).

The remaining parameters to be determined pertain to the characterization of the yield surface and the size of the imperfection amplitude ξ. To this end the band is modeled by a discontinuity in the yield stress, using $\sigma_y^B = (1 - \xi)\sigma_y^A$. The yield surface is modeled

as isotropic, non-quadratic (see definition in equation (2.1.21)), and the exponent β is taken as in Barlat et al. (1997b) for aluminum. The value of ξ is then chosen as before to give the most reasonable agreement with the available quasistatic FLD experiments on AA6061-T6 by LeRoy and Embury (1978), as shown in Table 2.5. The parameters

$$\beta = 8 \quad \xi = 10^{-3}$$

Table 2.5: Material parameters for FLD of AA6061-T6

given in Tables 2.1, 2.2, 2.4 and 2.5 completely characterize the mechanical, thermal and electric properties of the model used to run the simulations of the free expansion experiments of the tubes.

2.3.1.3   Strain, Strain Rate and Current Density Profiles

As previously, the present calculations of FLD's are based on the simplifying assumption of proportional strain paths. It is assumed that $\epsilon_2/\epsilon_1 = \dot{\epsilon}_2/\dot{\epsilon}_1 = \rho$, where $-1/2 \leqslant \rho \leqslant 1$ with the lower limit corresponding to uniaxial stress and the upper to equibiaxial plane stress. Moreover, as before for the time-dependent viscoplastic response of the material in EMF processes, strain history influences the solid's response and hence a strain profile $\epsilon_1(t)$ is also required. Determining the exact strain profile $\epsilon_1(t)$ requires solution of a coupled electromagnetic and thermomechanical problem of the tube plus its actuator coil, a feasible but complicated and time consuming task that is discussed in Chapter III. Such a modeling approach would be the 2-D version of the 1-D ring calculations done by Triantafyllidis and Waldenmyer (2004). In the interest of simplicity, and since a pulse-like strain rate history is expected for the hoop strains at any height of the expanding tube, the sinusoidal-shape strain and strain rate profiles of equations (2.1.26) and (2.1.27) are assumed.

The electromagnetic nature of the problem also requires knowledge of the time-dependent current density. As for the strain profile, the sinusoidal pulse current density of equation (2.1.30) is assumed. Experimental observations, as well as fully coupled electromechanical calculations in the ring problem (Triantafyllidis and Waldenmyer, 2004) show that the time duration of the first (and much larger) current pulse is approximately half the duration of the strain rate pulse, thus explaining the reason for the choice in equation (2.1.30).

The characteristic time τ_0, which is half of the measured duration of the main current pulse, and the maximum density J_{max} are available experimentally, according to Table 2.6. These parameter values are obtained from electric current versus time traces taken from tube expansion experiments. An example of one of these traces, here from case (a), is shown in Figure 2.16a. The comparison between experimental and simulation current traces is shown in Figure 2.16b, along with the dimensionless strain versus time trace. The energy used to expand the tube in each configuration is given in Table 2.6, and the pulse time τ_0 and maximum current density J_{max} used in the corresponding simulation are also listed accordingly.

Label	Tube (mm)	Coil	Energy (kJ)	J_{max} (A/m^2)	τ_0 (μsec)
a	31.7	4-turn	6.72	$5.10\ 10^9$	23
b	31.7	10-turn	8.00	$4.82\ 10^9$	36
c	85.1	4-turn	7.52	$2.50\ 10^9$	16
d	85.1	10-turn	13.92	$4.85\ 10^9$	33.5

Table 2.6: Experimentally Determined Parameters

Also note that from several experiments performed, only four (labeled a, b, c, d in Table 2.6) are to be simulated here.

The final issue to be resolved is the choice of the maximum hoop strain ϵ_{max} in equation (2.1.26) for simulating the selected four experiments. The choice adopted stems from
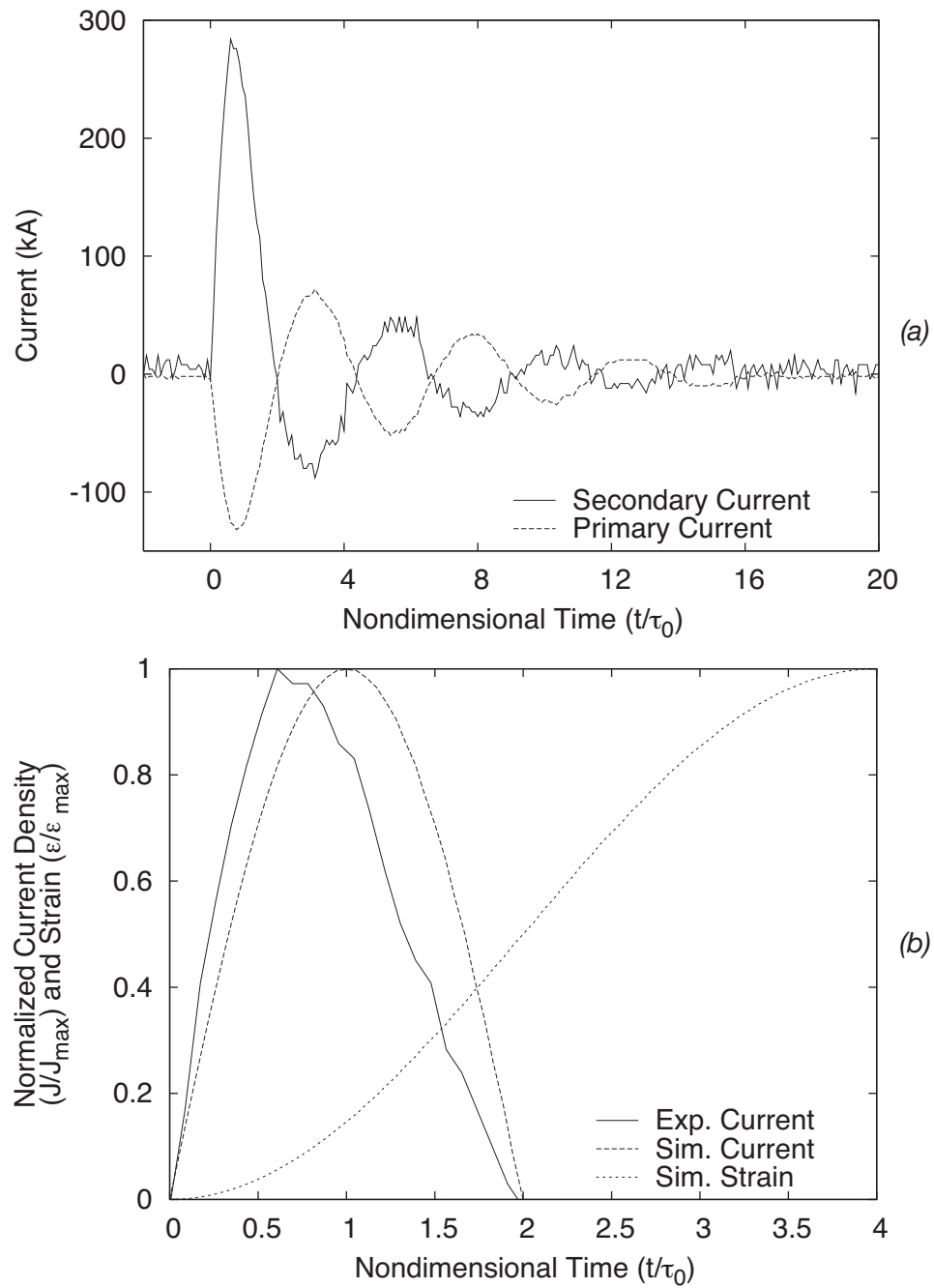
Figure 2.16: a) Example of an experimentally measured current versus time trace for tube and coil. b) Comparison of the experimentally determined current density profile with the simulated current density profile. Simulated dimensionless strain profile also shown in b). These plots correspond to a 31.7 mm tube deformed with a 4-turn coil at 6.72 kJ of energy (case (a)).

the experimental technique of gradually increasing the capacitor energy until tube neck-ing and/or failure is detected. Consequently for each ρ a simulation is run with a certain value of ϵ_{max} for which no necking is detected. A simple forward marching technique gradually tests larger values of ϵ_{max} until necking is achieved at $0.99\epsilon_{max}$. As an example of the forming speeds that result from this technique, for case (a) in Table 2.6 the maxi-mum simulation strain rate ranges from 4932 s^{-1} (plane strain) to 8793 s^{-1} (uniaxial).

2.3.2 Comparison of Results

At the completion of Section 2.3.1 the formulation of the EMF localization problem is fully defined. The numerical algorithm used to solve the governing equations is identical to that discussed in Section 2.2.1. Comparison of simulation and experiment follows.

2.3.2.1 Comparison of Experimental and Theoretical Results

The presentation of experimental results and the corresponding theoretical simula-tions is given in Figures 2.17 to 2.22. More specifically the experimentally obtained FLD's for cases (a) through (d) (see Table 2.6) plus the corresponding theoretical sim-ulation results are presented in Figure 2.17, Figure 2.20, Figure 2.21 and Figure 2.22 respectively. For comparison purposes the conventional quasistatic FLD's for the same cases (calculated in the absence of currents and using much larger pulse duration times τ_0) are also plotted in these figures to show the ductility increase due to the EMF process. Additional information for the first experiment (case (a)) is provided in Figure 2.18 (cur-rent configuration localization angle ϕ versus strain ratio ρ) and Figure 2.19 (temperatures inside θ^B and outside θ^A the band versus strain ratio ρ).

The FLD results for the short tube/short coil combination (case (a)) are presented in Figure 2.17. Notice that the experimental data are all for $\rho < 0$ and clustered about the uniaxial stress path ($\rho = -1/2$), as expected from Figure 2.14a, which shows localization
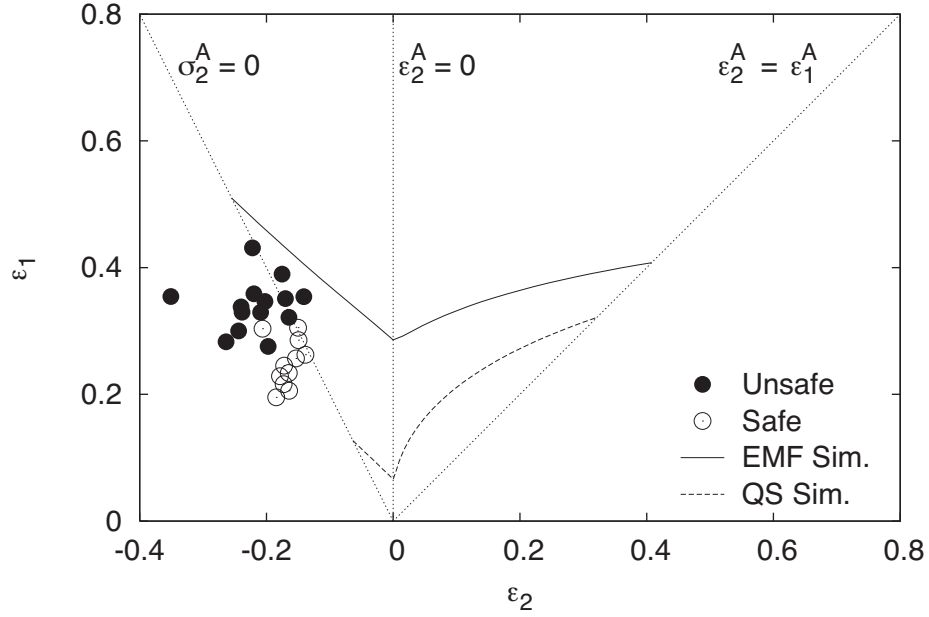
Figure 2.17: Comparison of simulated and experimental forming limits for an AA6063-T6 31.7 mm tube deformed using a 4-turn coil and 6.72 kJ of energy (case (a)).

at the top and bottom ends of the short tube. Both the measured and computed results show a significant increase in ductility in the electromagnetically expanded AA6063-T6 tube compared to the quasistatic curve, although the simulation overestimates the forming limits. Moreover, using Figure 2.15 one can observe that uniaxial quasistatic AA6063-T6 necking and failure occurs approximately at $\epsilon_{neck} = 0.11$. This corresponds with the $\rho = -1/2$ quasistatic forming limit in Figure 2.17 due to the use of rectangular high aspect ratio (width to thickness) samples in the uniaxial quasistatic tests (see Section 2.3.1.1). This observation is an experimental confirmation of the ductility increase in free forming using EMF, which is captured reasonably well by the present simulation.

The theoretically calculated current configuration critical angle ϕ versus the strain ratio ρ for the short tube/short coil experiment modeled in Figure 2.17 is plotted in Figure 2.18. Notice that similar to the quasistatic case, ϕ is a decreasing function of ρ for $-1/2 \leqslant \rho < 0$ while $\phi = 0$ for $\rho \geqslant 0$. Although localization angles are difficult to
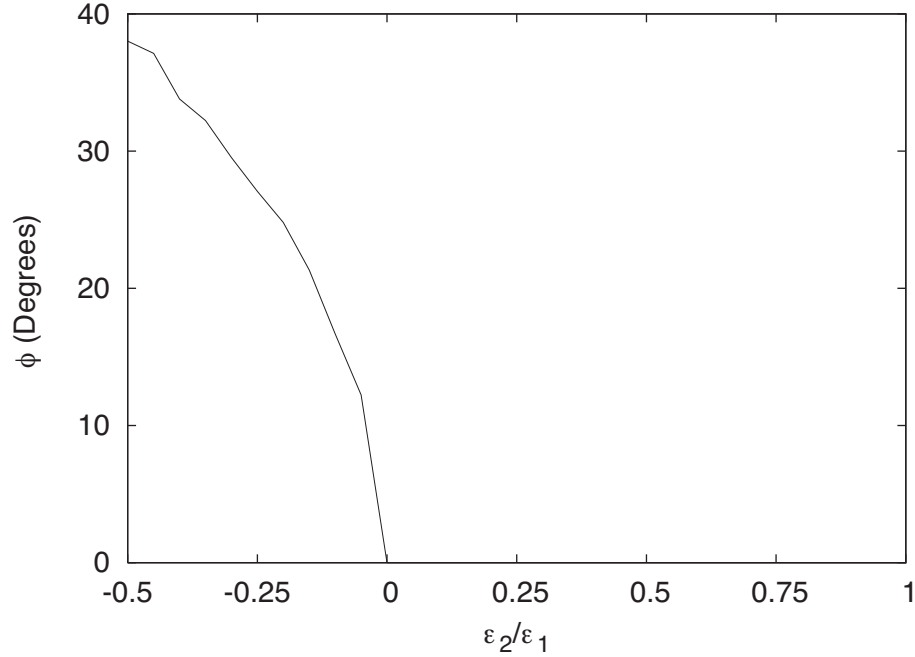
Figure 2.18: The localization angle ϕ in the current configuration as a function of strain ratio ρ, for the simulation of the 31.7 mm tube deformed with a 4-turn coil at 6.72 kJ (case (a)).

measure, where the necking band is visible along the full length of the tube (case (d), corresponding to $\rho = -1/2$) $\phi \approx 40°$.

The theoretically calculated inside θ^B and outside θ^A the band respectively temperatures at localization, as a function of strain ratio ρ for the experiment modeled in Figure 2.17, are plotted in Figure 2.19. Notice that the necking temperature is minimum for $\rho = 0$, as expected from the fact that the critical strain, ϵ_1, is a minimum here. Since τ_0 is kept constant for each case, the minimum critical strain gives the minimum strain rates and lowest flow stresses and thus the lowest amount of plastic dissipation $\sigma_e \dot{\epsilon}^p$. This dissipation contributes somewhat more thermal energy than the ohmic effect to the temperature change (Triantafyllidis and Waldenmyer, 2004).

Figures 2.20 through 2.22 show the results from the remaining three experiments (see Table 2.6 and also Figure 2.14). More specifically Figure 2.20 shows the results for the
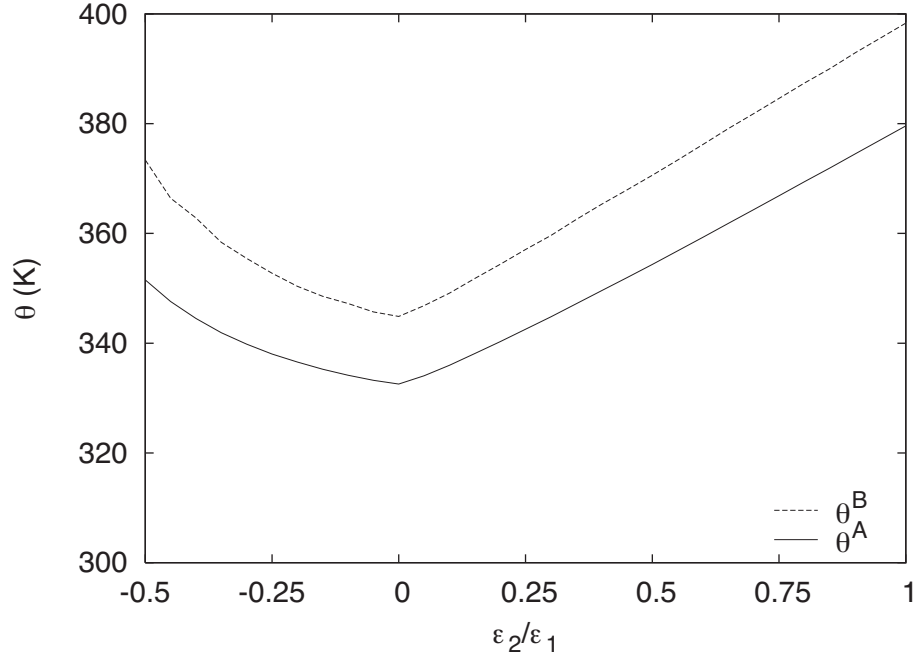
Figure 2.19: The temperature inside θ^B and outside θ^A the band at localization as a function of principal strain ratio ρ, for the simulation of the 31.7 mm tube deformed with a 4-turn coil at 6.72 kJ (case (a)).

shorter tube with the longer coil (case (b)) which shows the largest discrepancy between theory and experiments. This deviation can be explained from the fact that the failed tube in Figure 2.14b is a highly distorted toroidal segment, while the assumptions adopted for the computation of the FLD are based on uniformly expanding tubes.

The FLD in Figure 2.21 corresponds to the only experiment with data in the $\rho > 0$ region, as expected for case (c), in Figure 2.14c, where failure starts at the middle of the tube. Experimental points on $\rho = 0$ show agreement with theoretical predictions while experimental points for $\rho > 0$ show large deviations from theoretical results. This discrepancy is expected from the fact that yield surface parameters and anisotropy of sheet play a crucial role for the determination of $\rho > 0$ part of the FLD, and our simulation's simplified isotropic yield surface can be improved with a more sophisticated anisotropic alloy description. Moreover, as with case (a), despite overestimation of the forming lim-
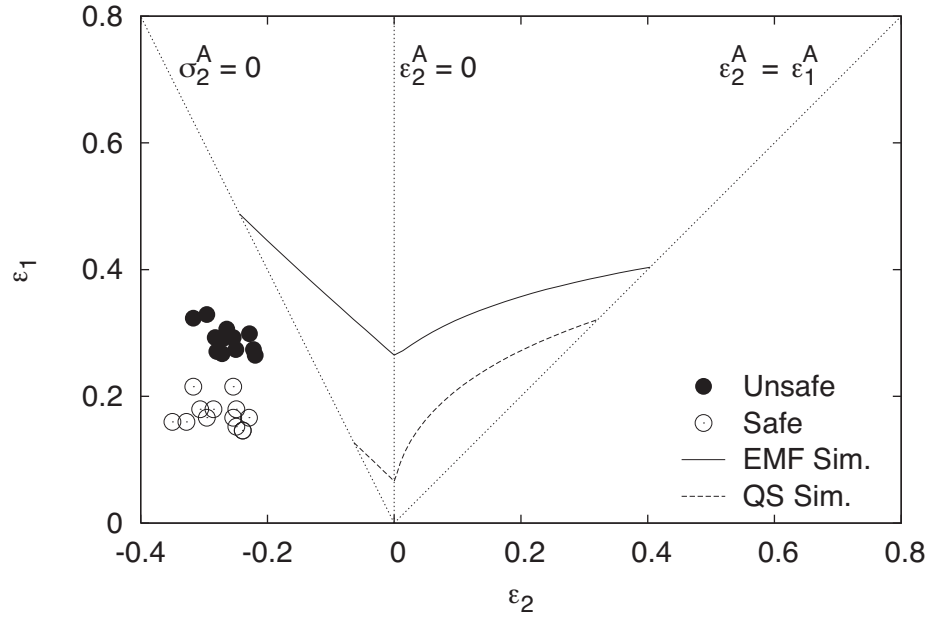
Figure 2.20: Comparison of simulated and experimental forming limits for an AA6063-T6 31.7 mm tube deformed using a 10-turn coil and 8 kJ of energy (case (b)).

its, a free formability increase is clearly shown experimentally.

Finally, Figure 2.22 corresponds to the long tube/long coil combination and the corresponding experimental data are again clustered around the uniaxial stress path $\rho = -1/2$, as expected from Figure 2.14d, which shows failure near the end sections of the tube. This comparison shows the closest agreement between experiment and simulation, with the forming limits minimally overestimated.

It should be noted that the theoretical predictions for all four experiments are predictably close to each other given the proximity of the values of the strain rates, current densities and characteristic times between the four different experiments. A critical discussion of the experimental and theoretical results is given subsequently.
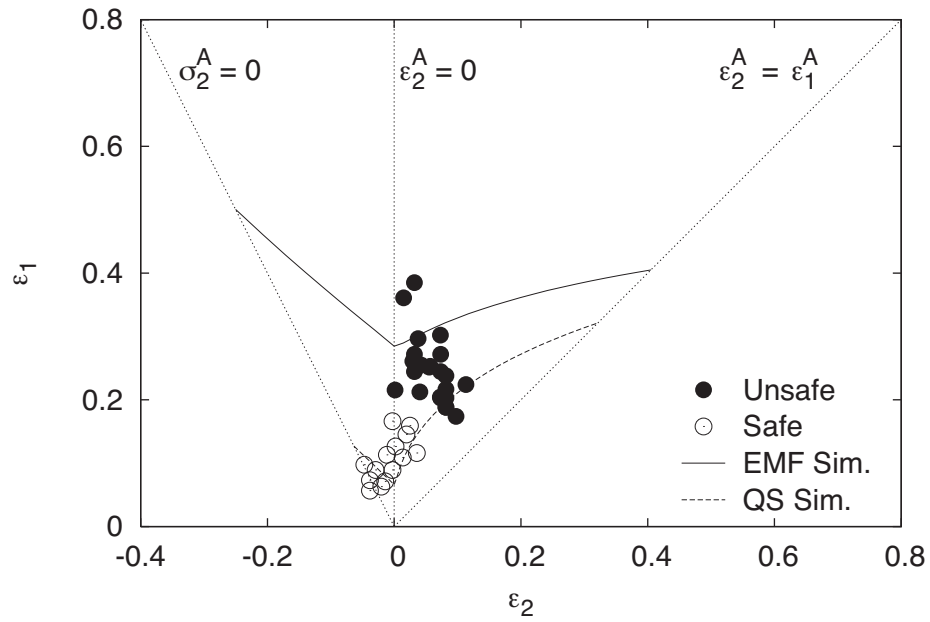
Figure 2.21: Comparison of simulated and experimental forming limits for an AA6063-T6 85.1 mm tube deformed using a 4-turn coil and 7.52 kJ of energy (case (c)).
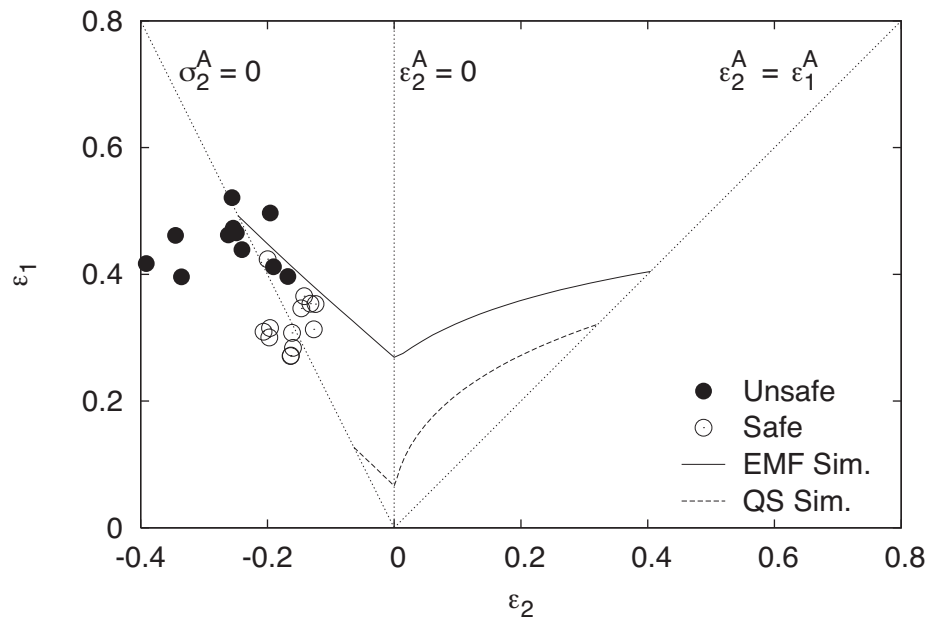
Figure 2.22: Comparison of simulated and experimental forming limits for an AA6063-T6 85.1 mm tube deformed using a 10-turn coil and 13.92 kJ of energy (case (d)).

2.4 Discussion of Results

The present analysis shows a significant increase in ductility from quasistatic to EMF conditions; the greatest difference occurs for strain paths with load path strain ratio $\rho \leqslant 0$. In the case $\rho < 0$, the angle of the weak band at necking in the reference configuration $\Phi_{\text{neck}} \neq 0$. And, when compared to results for $\rho > 0$, the predicted forming limits for $\rho \leqslant 0$ are insensitive to imperfection amplitude ξ and the yield surface choice. The reason for this ductility increase is the high strain rates, compared to conventional forming, inherent in an EMF process, given that the strain-rate sensitivity of the material delays the onset of necking (see Hutchinson and Neale (1977)). The present work shows that the details of the strain time profile do not significantly affect the forming limits, though the strain rate of the loading does. Increasing the electric current density can also increase ductility, though above a certain current density no additional ductility increase is found. However, the influence of the initial temperature θ_i depends on the temperature sensitivity exponent α, which indicates that the influence of electric current density will also vary with the material properties. Moreover, if a temperature-dependent strain-rate sensitivity $m(\theta)$ is implemented, such that m increases with temperature in accordance to existing experimental data, the limit on the ductility increase for increasing current density disappears and strains at the onset of necking for a fixed ρ increase monotonically with increasing current density.

The material constitutive response is of paramount importance in determining forming limits for EMF processes. The anisotropy and yield surface details strongly influence the forming limits in the $\rho > 0$ region, while $\rho \leqslant 0$ is largely unaffected by these aspects. However, the EMF formability is affected for all values of ρ by the hardening exponent n; ductility increases as n increases. Similarly, increasing the strain-rate sensitivity expo-

nent *m* for a fixed forming speed increases the onset of necking strains. The temperature sensitivity exponent α also has the same correlation with ductility. Increasing α increases forming limits.

For the free expansion experiments, the main reason for the increased ductility of aluminum alloys has been shown (Triantafyllidis and Waldenmyer, 2004) to be their strain-rate sensitivity at the high rates associated with the EMF processes. To this end, it is important to obtain an accurate constitutive description of the alloy that has strain rate as well as temperature sensitivity in its mechanical response, given the important heating effects due to the plastic dissipation and the induced currents. Although it was not possible to measure all the required constitutive properties of the experimentally used (AA6063-T6) tube alloy, a careful literature search has given the remaining properties from reliable, independently obtained data of a closely related (AA6061-T6) sheet alloy. Implementing these properties shows an increase in formability due to rate sensitivity in the FLD simulations, which is confirmed experimentally. However, comparing experiment to simulation shows overestimation to varying degrees in each forming limit diagram. A more accurate experimentally based constitutive characterization of the material is necessary for further investigations.

In addition to the influences on formability investigated in the present work, there are a number of other possible factors to be addressed. It is important to recall that all the results here depend on the imperfection parameter ξ, most significantly for strain paths with $\rho > 0$, a rather undesirable – but inevitable under adopted simplifying assumptions – feature of the FLD analysis.

There is also some controversy about the magnitude and/or existence of a free forming EMF ductility increase over conventional techniques. The present work considers only tube free expansion, while others (Imbert et al., 2005b; Oliveira and Worswick, 2003; Oli-

veira et al., 2005; Zhang and Ravi-Chandar, 2006) have considered different geometries. Oliveira and Worswick (2003) and Oliveira et al. (2005) consider forming aluminum sheet into a rectangular die opening. No formability improvement in their electromagnetically free formed parts is reported. Those authors show EMF strains higher than the quasistatic forming limits but attribute them to strain path changes after workpiece failure. However, Imbert et al. (2005b) do show EMF free forming strains above the traditional quasistatic limits of their aluminum alloy on safe (no necking or failure) parts. Those experiments use aluminum sheet free formed into a circular die opening and indicate that EMF may enhance free formability. It should be noted that the electromagnetic process free forming strain rates of Oliveira and Worswick (2003) and Oliveira et al. (2005) are approximately half of the rates encountered in the present experiments, and the aluminum alloy is AA5754, a considerably different alloy than the tube alloy AA6063-T6. Work by Vural et al. (2004) and Yadav et al. (1995) shows a distinct alloy-dependent threshold above which strain-rate sensitivity becomes important, indicating these differences may significantly influence the experiments. This issue should be investigated in the light of complete experimental evidence, especially since the material constitutive response is alloy-dependent (e.g. the transition strain rate varies widely between aluminum alloys (Tirupataiah and Sundararajan, 1994)).

Inertia is ignored in these necking simulations. In previous unpublished work on ring expansion (Triantafyllidis, 2004), an increase in ductility occurred with an increase in ring density (with all other ring properties remaining the same). More sophisticated dynamic stability analyses have been carried out for bars (Fressengeas and Molinari, 1989) and rings (Mercier and Molinari, 2004) that show how inertia selects the critical wave number, influencing (delaying) necking. Other work (Hu and Daehn, 1996; Knoche and Needleman, 1993; Regazzoni et al., 1986; Zhang and Ravi-Chandar, 2006) has shown

similar results, indicating that inertia should be accounted for in dynamic necking calculations. Similarly, contact effects are known to strongly influence high velocity forming (e.g. Balanethiram and Daehn (1994); Imbert et al. (2005b)).

Finally, the present work makes the implicit assumption that the thermal response of the material is the same under quasistatic and EMF forming speeds. At the time scale of EMF forming (i.e. on the order of 50 μsec) the material thermal constitutive response may vary greatly from that observed at conventional speeds. Further experimental evidence is needed to characterize the material's response to temperature changes over these time scales. However, in spite of the adopted simplifying assumptions and given the independence of results of strain profile, the current investigation can provide a useful and fairly accurate predictive tool for making ductility calculations for EMF processes.

2.A Appendix: Justification of Necking Criterion

The necking criterion used in the electromagnetic FLD calculations is a weak band initial imperfection criterion, similar in spirit to the thickness inhomogeneity criterion first introduced by Marciniak and Kuczynski (1967) to account for necking in the biaxial stretching region of an elastoplastic solid within the framework of classical plasticity theory (smooth yield surface and normality). The dependence of the necking strain predictions on the size of the initial imperfection is a rather undesirable feature of this approach, which has lead to the proposition of alternative necking criteria. For the case of rate-independent solids, Stören and Rice (1975) proposed a necking criterion based on the loss of ellipticity in the equations governing the incremental plane stress deformation of the sheet, which are based on a deformation type theory of plasticity, thus predicting necking independently of imperfections. Unfortunately, this approach cannot be generalized for viscoplastic solids, whose incremental response is governed by their elastic

moduli.

To avoid the assumption of an initial imperfection, Triantafyllidis et al. (1997) proposed a linearized perturbation criterion for the stability of elastoviscoplastic solids, which was based on the growth/decay of the perturbation acceleration in response to a velocity perturbation of unit norm. This criterion was expanded upon by Massin et al. (1999) and generalized for continua by Nestorović et al. (2000). Unlike the compressive load cases for which it was conceived, the application of this linearized perturbation criterion to the analysis of necking under tension gives unrealistic results (critical strain decreases for increasing load rates) and hence had to be abandoned as a candidate necking criterion. However, the comparison of the necking predictions for the linearized perturbation and initial imperfection criteria for the case of an elastoviscoplastic bar subjected to uniaxial tension is both novel (to the best of the author's knowledge) and useful and merits a brief presentation.

2.A.1 Kinematic and Constitutive Relations

For simplicity, no thermal effects are considered and the material in the uniaxially loaded bar is treated as incompressible. The latter assumption yields

$$al = AL, \tag{2.A.1}$$

where a (A) is the current (reference) cross section area and l (L) is the current (reference) length. In this finite strain problem the strain, ϵ, is defined as

$$\epsilon \equiv \ln(l/L), \tag{2.A.2}$$

and the first Piola-Kirchhoff stress, Π (force/reference area), can be expressed with the help of equations (2.A.1) and (2.A.2) in terms of the Cauchy stress, σ, and strain, ϵ, by

$$\Pi = \sigma \exp\left(-\epsilon\right). \tag{2.A.3}$$

The uniaxial strain is decomposed into elastic, ϵ^e, and plastic, ϵ^p, parts, and the constitutive response reads

$$\sigma = E\epsilon^e, \quad \epsilon^e = \epsilon - \epsilon^p. \tag{2.A.4}$$

For a viscoplastic material the relation between $\dot{\epsilon}^p$ and the solid's quasistatic uniaxial response $g(\epsilon^p)$ is governed by the function F,

$$\dot{\epsilon}^p = F(\sigma, g(\epsilon^p)). \tag{2.A.5}$$

Here two versions of the function F, namely F_p and F_l, will be used. F_p is the same power law constitutive model that was used for the FLD calculations, i.e.

$$F_p = \dot{\epsilon}_0^p \left[\left(\frac{\sigma}{g(\epsilon^p)} \right)^{1/m} - 1 \right], \tag{2.A.6}$$

where m is the strain-rate sensitivity exponent and $\dot{\epsilon}_0^p$ is the viscoplastic time scale. F_l represents an alternative linear overstress model

$$F_l = \frac{\dot{\epsilon}_0^p}{\sigma_y} \left[\sigma - g(\epsilon^p) \right], \tag{2.A.7}$$

where σ_y is the material's uniaxial yield stress. It is important to note that $\dot{\epsilon}_0^p$ is not equivalent between the two constitutive laws. The uniaxial quasistatic response for both versions of F is

$$g(\epsilon^p) = \sigma_y \left[1 + \frac{\epsilon^p}{\epsilon_y} \right]^n, \tag{2.A.8}$$

where $\epsilon_y = \sigma_y / E$ and n is the hardening exponent. Base case values of material parameters from the FLD simulations (see Tables 2.1 and 2.2) are also used here.

2.A.2 Linearized Perturbation Analysis

For the one dimensional bar model, the linearized perturbation stability criterion, introduced in Triantafyllidis et al. (1997), works as follows: consider that at time t_0 a perturbation in the field quantities of zone B of the bar (see insert in Figure 2.A.1) is introduced
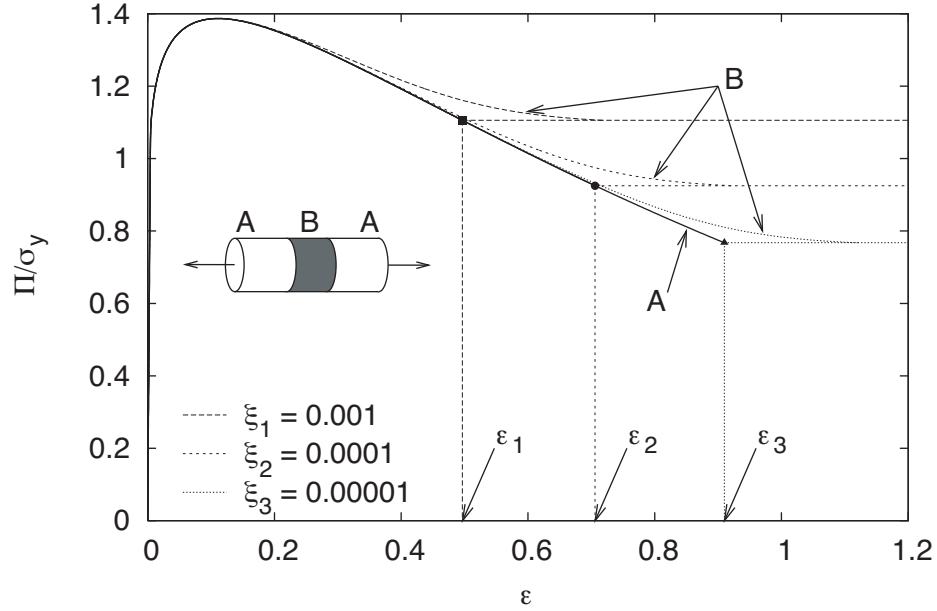
Figure 2.A.1: Nondimensional first Piola-Kirchhoff stress (Π/σ_y) versus logarithmic strain for three values of imperfection parameter ξ based on the power law constitutive model and the sinusoidal strain profile. The force versus strain is plotted both outside (A) and inside (B) the weak band thus illustrating the existence of the necking strain.

and let $\Delta f \equiv f_B - f_A$ denote the difference in the field quantity f between the perturbed (B) and unperturbed (A) parts of the bar. Furthermore assume that the perturbation results in a given $\Delta\dot\epsilon > 0$. In this linearized stability analysis a perturbation is defined to be stable when the resulting $\Delta\ddot\epsilon < 0$, i.e. when the rate of $\Delta\dot\epsilon$ decreases near time t_0. One can thus define $\Lambda \equiv \Delta\ddot\epsilon/\Delta\dot\epsilon$; an unstable bar results in $\Lambda > 0$. Hence, $\Lambda = 0$ signals the onset of a necking instability, and the corresponding critical condition is independent of the size of the perturbation.

Equilibrium of the bar implies

$$\Delta\Pi = 0. \tag{2.A.9}$$

Linearizing about the principal solution (zone A) the response of the bar to a perturbation in $\dot\epsilon$, one obtains from the first and second rate of equation (2.A.9)

$$\Delta\dot\Pi = \mathscr{S}_{11}\Delta\dot\epsilon + \mathscr{S}_{10}\Delta\epsilon = 0 \tag{2.A.10}$$

and

$$\Delta\ddot{\Pi} = \left(\mathscr{S}_{22}\Lambda + \mathscr{S}_{21}\right)\Delta\dot{\epsilon} + \mathscr{S}_{20}\Delta\epsilon = 0, \tag{2.A.11}$$

where the coefficients $\mathscr{S}_{10}$, $\mathscr{S}_{11}$, $\mathscr{S}_{20}$, $\mathscr{S}_{21}$ and $\mathscr{S}_{22}$ are given by

$$\mathscr{S}_{10} = -\left[\left(E - \sigma\right)\dot{\epsilon} + \dot{\sigma} + E^2\frac{\partial F}{\partial\sigma}\right],$$

$$\mathscr{S}_{11} = E - \sigma,$$

$$\begin{aligned}\mathscr{S}_{20} = E^2\frac{\partial F}{\partial\sigma}&\left(E\frac{\partial\dot{F}}{\partial\dot{\sigma}} - \frac{\partial\dot{F}}{\partial\dot{g}}\frac{\partial\dot{g}}{\partial\dot{\epsilon}^p} + 2\dot{\epsilon}\right)\\ &- E^2\frac{\partial\dot{F}}{\partial\sigma} + E\left(\dot{\epsilon}^2 - \ddot{\epsilon}\right) - \left(\ddot{\sigma} - 2\dot{\sigma}\dot{\epsilon} + \sigma\dot{\epsilon}^2 - \sigma\ddot{\epsilon}\right),\end{aligned} \tag{2.A.12}$$

$$\mathscr{S}_{21} = -\left[2\left(E - \sigma\right)\dot{\epsilon} + 2\dot{\sigma} + E^2\frac{\partial\dot{F}}{\partial\dot{\sigma}}\right],$$

$$\mathscr{S}_{22} = E - \sigma.$$

Writing equations (2.A.10) and (2.A.11) in matrix form gives

$$\begin{bmatrix} \mathscr{S}_{11} & \mathscr{S}_{10} \\ \mathscr{S}_{22}\Lambda + \mathscr{S}_{21} & \mathscr{S}_{20} \end{bmatrix}\begin{pmatrix} \Delta\dot{\epsilon} \\ \Delta\epsilon \end{pmatrix} = 0. \tag{2.A.13}$$

Nonzero solutions to the above matrix equation exist only if the determinate of the coefficient matrix is zero, which implies

$$\Lambda = \frac{\mathscr{S}_{11}\mathscr{S}_{20} - \mathscr{S}_{10}\mathscr{S}_{21}}{\mathscr{S}_{10}\mathscr{S}_{22}}. \tag{2.A.14}$$

Notice that Λ is a function of the time-dependent solution of the viscoplastic bar problem, and for a well posed problem at the onset of the bar's loading $\Lambda < 0$. An instability occurs when $\Lambda = 0$, which from equation (2.A.14) gives the following condition at the onset of instability

$$\mathscr{S}_{11}\mathscr{S}_{20} - \mathscr{S}_{10}\mathscr{S}_{21} = 0. \tag{2.A.15}$$

To implement this criterion the principal solution of the elastoviscoplastic bar is formulated as a set of two first order ODE's from the rate of equation $(2.A.4)_1$ and equation $(2.A.5)$, namely

$$\dot{\mathbf{x}} = f(\mathbf{x}, t), \quad \mathbf{x} \equiv [\sigma, \epsilon^p].\tag{2.A.16}$$

These are solved with a fourth order Runge-Kutta algorithm, and numerical precision is ensured by keeping the same time step as used in the FLD calculations. The necking criterion, $\Lambda = 0$, is detected via a simple bisection method.

2.A.3 Initial Imperfection Analysis

The analysis here is the one-dimensional (uniaxial stress) version of the two-dimensional theory presented in Section 2.1. As a strain profile is applied to the bar, the strains outside, ϵ^A, and inside, ϵ^B, the weak band are compared (see the inset diagram in Figure 2.A.1). Necking occurs when the ratio of the plastic strain rate inside the band to that outside the band becomes unbounded, i.e. when $\dot{\epsilon}^p_B / \dot{\epsilon}^p_A \to \infty$. The imperfection is implemented as $\sigma^B_y = (1 - \xi)\sigma^A_y$, with the reference imperfection parameter $\xi = 0.001$ carried over from the FLD calculations.

From the rate of force continuity across the band, i.e. continuity of the first Piola-Kirchhoff stress rate $\dot{\Pi}$, one obtains with the help of equation (2.A.3) the following relation between the stress and strain rates inside and outside the weak band

$$\exp\left(-\epsilon^A\right)\left(\dot{\sigma}^A - \dot{\epsilon}^A \sigma^A\right) = \exp\left(-\epsilon^B\right)\left(\dot{\sigma}^B - \dot{\epsilon}^B \sigma^B\right).\tag{2.A.17}$$

This equation along with the equations $(2.A.4)_1$ and $(2.A.5)$ determine the solution in the weak band. As in the linearized perturbation analysis, the principal solution (outside the band) is formulated from the rate of equation $(2.A.4)_1$ and equation $(2.A.5)$ as two ODE's. Then, these two equations (the rate of equation $(2.A.4)_1$ and equation $(2.A.5)$)

applied inside the band and equation (2.A.17) give three ODE's for the three unknowns σ^B, ϵ^B and ϵ_B^p, i.e.

$$\dot{\mathbf{x}}^B = f(\mathbf{x}^B, t), \quad \mathbf{x}^B \equiv [\sigma^B, \epsilon^B, \epsilon_B^p], \tag{2.A.18}$$

where the t-dependent terms are functions of the principal solution $\mathbf{x}^A(t)$. These ODE's are solved with a fourth order Runge-Kutta algorithm using the same time steps as the FLD calculations. The necking criterion is numerically implemented as when $\dot{\epsilon}_B^p / \dot{\epsilon}_A^p > 10$. This value, 10, is chosen in accordance with the previous FLD calculations and has negligible effect on the computed critical strains.

2.A.4   Strain Profile Selection

The applied strain profile must be specified for the completion of the simulation. Two different profiles are considered, a sinusoidal profile and a linear profile that match the ϵ_1 profiles taken in the FLD calculations, which are given by

$$\epsilon(t) = \frac{\epsilon_{\max}}{2} \left[1 - \cos\left(\frac{\pi t}{4\tau_0} \right) \right], \quad \epsilon(t) = \epsilon_{\max} \frac{t}{4\tau_0}. \tag{2.A.19}$$

Due to the same considerations as in the FLD work, $\epsilon_{\max} = 1$ is used in the present work, and τ_0 is varied through the term $\dot{\epsilon}_0^p \tau_0$, with further discussion following in Section 2.A.5.

2.A.5   Results and Discussion

The section compares the onset of necking predictions from the above introduced two criteria and for the four combinations of two constitutive laws, power law F_p and linear overstress F_l, and two load profiles, sinusoidal and linear.

Figure 2.A.1 presents the dimensionless first Piola-Kirchhoff stress, Π, versus logarithmic strain, ϵ, in the bar with power law viscosity subjected to a sinusoidal strain profile. The initial imperfection model is examined, and Π/σ_y versus ϵ is given for both

outside (A) and inside (B) the band. The rate of deformation is set by the dimensionless measure of characteristic speed $(\dot{\epsilon}_0^p \tau_0)^{-1}$, with $(\dot{\epsilon}_0^p \tau_0)^{-1} = 26.9$. Results for three different values of the imperfection parameter ξ are calculated.

In a quasistatic process necking is predicted at the maximum force (equivalently maximum Π). For a viscoplastic bar the maximum force during a process depends on the loading rate due to its strain-rate sensitivity. From equilibrium the force in the bar outside and inside the weak band must be equal, but due to the relative weakness of the band $\dot{\epsilon}_B^p > \dot{\epsilon}_A^p$. This unequal strain rate allows the weak band to reach higher stresses than the outside zone thus permitting considerable elongation past the point where the maximum force occurs; the strain-rate sensitivity stabilizes the weak band by strengthening the material as the strain rate increases. Necking occurs when for some force Π/σ_y the strain rate inside the band tends to infinity. The imperfection parameter strongly affects the force level at which this necking phenomenon happens.

The dimensionless first Piola-Kirchhoff stress versus strain response of the power law elastoviscoplastic bar subjected to a sinusoidal strain profile and for characteristic speeds $(\dot{\epsilon}_0^p \tau_0)^{-1}$ from 0.159 to 100 is presented in Figure 2.A.2. Necking calculations for the initial imperfection analysis with three different imperfections ($\xi = 10^{-3}$, 10^{-4}, 10^{-5}) and the linearized perturbation method are shown. The initial imperfection calculations, for each fixed ξ value, show higher necking strains for higher speeds. The linearized perturbation criterion shows the opposite trend, agreeing with the initial imperfection model's necking strain prediction at quasistatic speeds (maximum force) and predicting decreasing necking strains from there as the speed increases. Also, as ξ decreases the initial imperfection criterion necking strain prediction increases as noted previously, and for all ξ values an upper limit on the necking strain exists such that above a certain speed further loading rate increases have little influence.
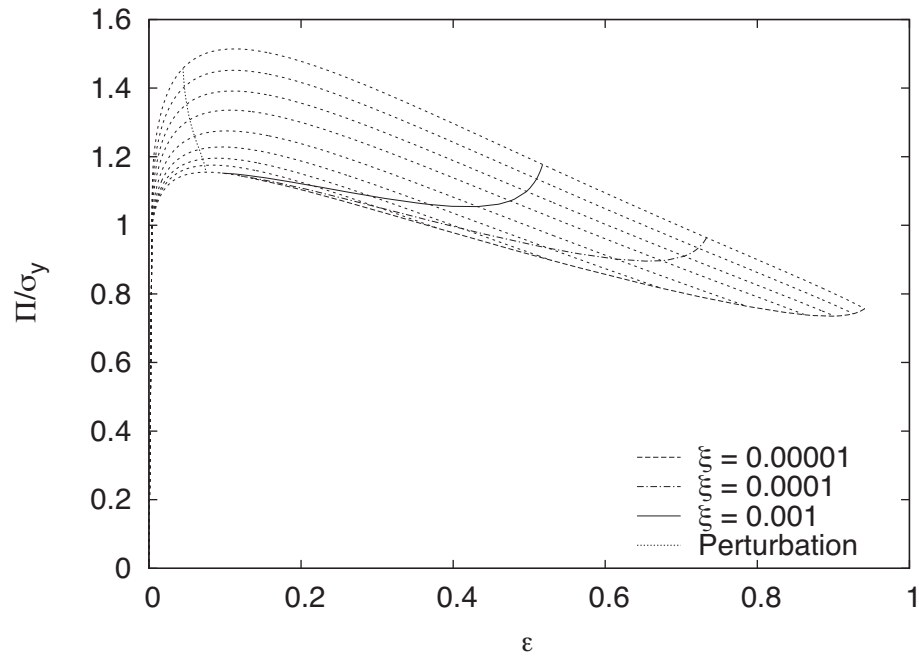
Figure 2.A.2: The nondimensional first Piola-Kirchhoff stress versus logarithmic strain for varying loading rates (the stress increases with increasing loading rate), based on the power law constitutive model and the sinusoidal strain profile. The onset of necking strain prediction from the linearized perturbation criterion is recorded, as is the necking prediction from the initial imperfection analysis for three values of imperfection parameter ξ.
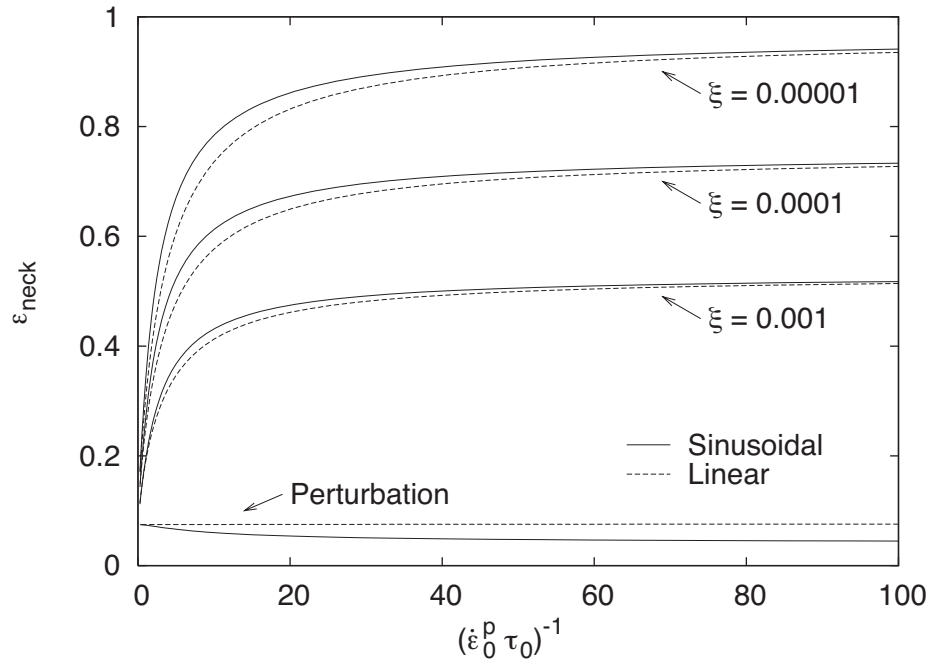
Figure 2.A.3: Onset of necking strain versus nondimensional strain rate based on the power law constitutive model for the sinusoidal and linear strain profiles using initial imperfection and linearized perturbation criteria.

In Figure 2.A.3 the necking strains predicted by each criterion, and calculated for the power law constitutive model, are plotted against the nondimensional characteristic speed. Onset of necking results for both the sinusoidal and linear strain profiles are presented, using three values of the imperfection parameter ξ and the linearized perturbation criterion. The initial imperfection based necking curves show increasing necking strains with increasing speed. The plateau in the onset of necking with respect to deformation rate is also clear, and the influence of the linear strain profile is not pronounced according to these results. Perturbation based results show the opposite trend, i.e. a decrease of necking strain for an increase of loading rate. Note also for the linearized perturbation results that the linear loading profile shows higher necking strains than its sinusoidal counterpart, in contrast to the initial imperfection criterion.

The counterpart to the results in Figure 2.A.3 calculated this time for the linear over-
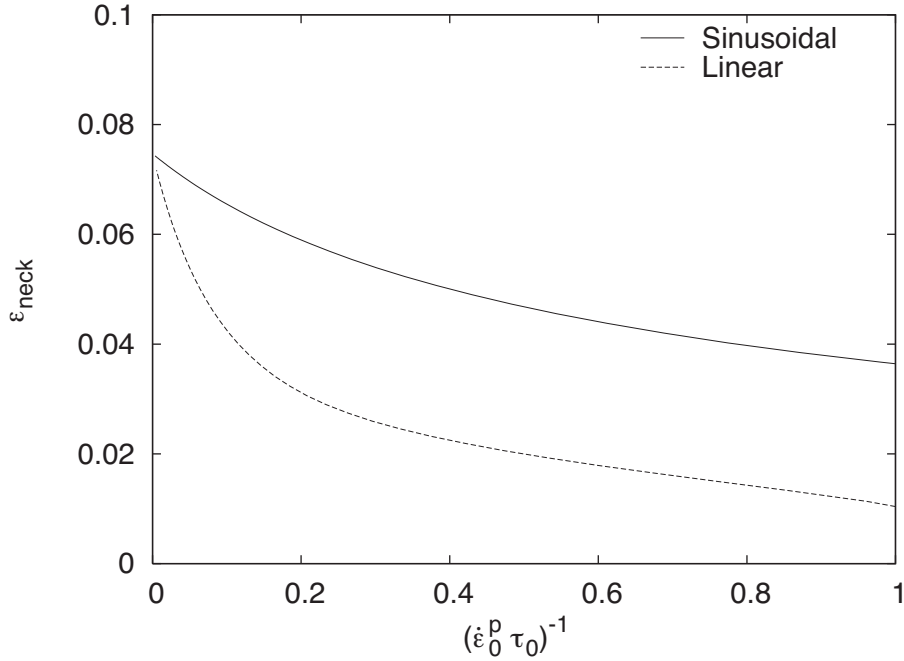
Figure 2.A.4: Onset of necking strain versus nondimensional strain rate using the linearized perturbation criterion and based on the linear overstress constitutive model for the sinusoidal and linear strain profiles.

stress constitutive model are presented in Figures 2.A.4 and 2.A.5. The difference in the magnitude of ϵ_{neck} for the linearized perturbation and initial imperfection criteria necessitates separate plots. A comparable stress-strain response between F_p and F_l requires different $\dot{\epsilon}_0^p$ values, giving unequal speeds $(\dot{\epsilon}_0^p \tau_0)^{-1}$ for processes with the same forming time τ_0.

The strain at necking for the linearized perturbation criterion versus nondimensional loading speed is shown in Figure 2.A.4. Results for both the sinusoidal and linear strain profiles are shown. At quasistatic speeds the onset of necking strain approaches the quasistatic necking value (maximum force) for both strain profiles. Similarly to the results for the power law constitutive model, as $(\dot{\epsilon}_0^p \tau_0)^{-1}$ increases the linearized perturbation necking strain prediction decreases, but in contrast to the power law material (see Figure 2.A.3) the sinusoidal strain profile shows higher necking strains than the linear profile.
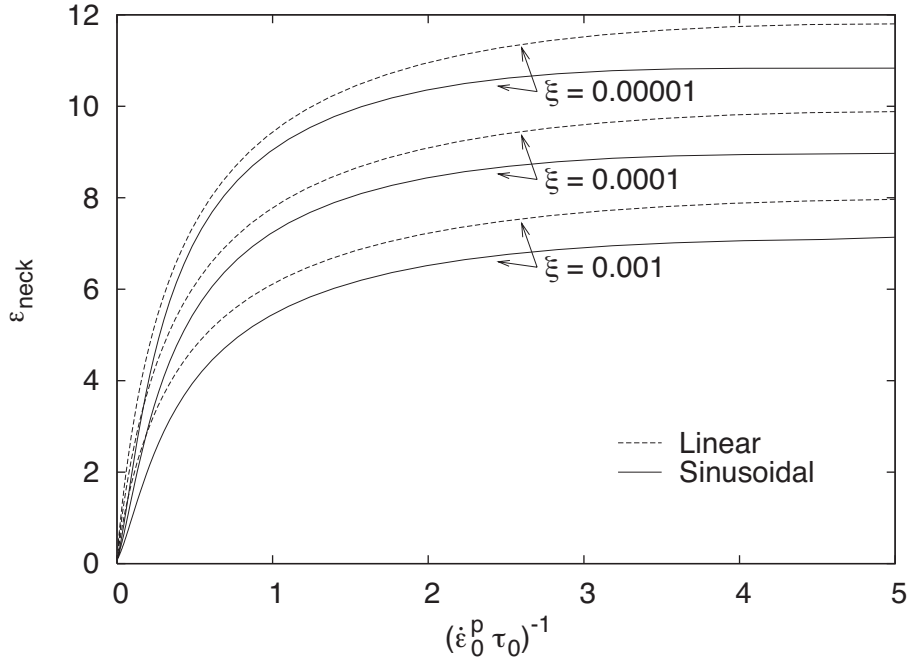
Figure 2.A.5: Onset of necking strain versus nondimensional strain rate using the initial imperfection criterion and based on the linear overstress constitutive model for the sinusoidal and linear strain profiles.

Also noteworthy, the strain at necking for the linear strain profile is no longer constant with respect to forming speed.

Finally, the onset of necking strain for the initial imperfection criterion versus nondimensional characteristic speed for the sinusoidal and linear strain profiles is given in Figure 2.A.5. As expected for all three values of ξ, the imperfection necking strain prediction approaches the quasistatic value as $(\dot{\epsilon}_0^p \tau_0)^{-1} \rightarrow 0$, but it increases considerably at high deformation rates. For loading rates $(\dot{\epsilon}_0^p \tau_0)^{-1} > 1$ the necking stains for the linear overstress model (Figure 2.A.5) are rather (> 4) unrealistic (and much higher than those for the power law model (Figure 2.A.3)). Also, unlike the power law model, the predicted necking strains with the linear overstress model for the linear strain profile are higher than those for the sinusoidal profile. However, as with the power law model, the predicted necking strains increase as ξ decreases, and there is an upper limit on the

necking strains for increasing loading speed.

It is clear from the results presented above that realistic necking predictions are gained only with the initial imperfection criterion. In all the cases considered, the linearized perturbation criterion gives onset of necking strains that decrease from the quasistatic value (maximum force) monotonically with increasing loading rate. This result is in contradiction with experimental evidence from high strain rate free forming results that show formability equal to or greater than that under quasistatic conditions (see Hu and Daehn (1996); Hutchinson and Neale (1977); Oliveira and Worswick (2003)). The initial imperfection criterion is at this point the reasonable choice for ductility calculations of interest in this work.

CHAPTER III

Formulation and Numerical Implementation of EMF Processes in Finitely Strained Solids

The present chapter pertains to the consistent, fully coupled modeling of electromagnetic-mechanical processes, specifically in the context of EMF. The governing equations are Maxwell's equations in deformable solids and the mechanical equation of motion (along with the equations describing thermal effects and internal variable evolution, as necessary). A consistent variational formulation of the electromagnetic problem in deformable solids was introduced by Lax and Nelson (1976), who derived Maxwell's equations, the electromagnetic fields, and the electromagnetic Lagrangian in the reference configuration (i.e. the Lagrangian or material description). This Lagrangian is the reference configuration counterpart of the classical electromagnetic Lagrangian in the current configuration (i.e. the Eulerian or spatial description). Trimarco and Maugin (2001) and Trimarco (2007) combine the electromagnetic Lagrangian terms with the necessary mechanical terms to give an electromagnetic-mechanical reference configuration Lagrangian, from which the Euler-Lagrange equations give Maxwell's equations and the mechanical equation of motion. Their variational technique provides Maxwell's equations in the reference configuration, but for EMF, the eddy current approximation to Maxwell's equations is all that is necessary. The present work proposes a variational technique that consistently provides the governing equations under the eddy current ap-

69

proximation. Following this, through application of a variational integration technique, the resulting numerical scheme is shown to provide a consistent staggered solution algorithm.

The discussion begins in Section 3.1 with a derivation of the coupled electromagnetic-mechanical equations. Section 3.1.1 presents the derivation in the current configuration, following the technique of Kovetz (2000). Having derived the governing equations, Section 3.1.2 turns to the reference configuration form of these equations and the electromagnetic fields, derived using a method similar to that of Lax and Nelson (1976). The resulting relations between current and reference configuration fields allow the introduction of the electromagnetic-mechanical Lagrangian, and the subsequent variational technique based on the least action principle is discussed in Section 3.1.3, completing the general formulation. Section 3.2 proposes the variational principle under the eddy current approximation and discusses the restriction of the numerical implementation to axisymmetric forming cases, adopted to simplify this first application of the general theory. The resulting formulation is numerically implemented with a variational integration technique, as outlined in Section 3.3. Results of relevant ring and tube expansion simulations are presented in Section 3.4. In addition, the novel problem of a tube with a nonconducting outer coating is solved and the effect of the coating quantified. Finally, Section 3.5 is a concluding discussion of the formulation and results.

3.1 Formulation of Fully Coupled Electromagnetic-Thermal-Mechanical Problem

Two methods for deriving the fully coupled governing equations and interface conditions of an electromagnetic-thermal-mechanical process are presented. First is the direct method, which uses conservation principles in the current configuration to derive the

governing equations and boundary conditions. This approach essentially follows Kovetz (2000), where the interested reader is addressed for additional details. Subsequently, kinematic relations from continuum mechanics are applied to transform the governing equations from the current to the reference configuration.

Using the relations between current and reference configuration fields, the second, variational method is presented, namely the classical least-action principle (see Lax and Nelson (1976) for the purely electromagnetic case) in the reference configuration. This method gives the reference configuration governing equations and interface conditions, and it is shown that the two methods agree.

3.1.1   Conservation Law Approach (Current Configuration)

Gauss' law states the electric charge conservation in an arbitrary control volume $v(t)$ that is allowed to move and deform following the material. Electric charge conservation dictates

$$\int_{\partial v(t)} \boldsymbol{d} \bullet \boldsymbol{n} \ \mathrm{d}s = \int_{v(t)} q \, \mathrm{d}v, \qquad (3.1.1)$$

where $\partial v(t)$ is the surface boundary of the control volume $v(t)$, $\boldsymbol{n}$ is the outward normal to the surface $\partial v(t)$, $\boldsymbol{d}$ is the electric displacement, and q is the volumetric charge[1]. The pointwise form of Gauss' equation and the associated interface condition follow from the arbitrariness of the control volume and standard arguments involving Gauss' divergence theorem, namely

$$\triangledown \bullet \boldsymbol{d} = q, \ \boldsymbol{n} \bullet [\![\boldsymbol{d}]\!] = 0, \qquad (3.1.2)$$

where $[\![\ ]\!]$ denotes the jump in a quantity across a surface. For simplicity, and without loss of generality, it is assumed from here on that all electric charges and currents within

---

[1] Here and subsequently Chapter III defines symbols independently of Chapter II, with standard notation used whenever possible.

the problem domain are volumetric.

Faraday's induction law states that the circulation of the electromotive intensity $\mathcal{E}$ about a closed circuit $\partial s(t)$ opposes the change of the flux of the magnetic field $\boldsymbol{b}$ through the surface $s(t)$, i.e.

$$\oint_{\partial s(t)} \mathcal{E} \bullet \boldsymbol{s} \ \mathrm{d}l = -\frac{\mathrm{d}}{\mathrm{d}t} \int_{s(t)} \boldsymbol{b} \bullet \boldsymbol{n} \, \mathrm{d}s, \tag{3.1.3}$$

where $\partial s(t)$ is the line boundary of the control surface $s(t)$, $\boldsymbol{s}$ is the tangent vector to $\partial s(t)$, and $\boldsymbol{n}$ is the normal to the surface directed positively using the right hand rule applied to $\boldsymbol{s}$ on $\partial s(t)$. Again, since the control surface is arbitrary, the pointwise form of Faraday's equation and the associated interface condition follow by using standard arguments involving Stokes' theorem

$$\boldsymbol{\triangledown} \times \mathcal{E} = -\overset{*}{\boldsymbol{b}}, \ \boldsymbol{n} \times [\![\mathcal{E}]\!] = \boldsymbol{0}, \tag{3.1.4}$$

where $\overset{*}{(\ )}$ denotes the flux derivative. Note that since the control volume or surface may move and deform the conservation laws must be written in terms of Galilean invariants. The electric displacement $\boldsymbol{d}$ and magnetic field $\boldsymbol{b}$ are themselves Galilean invariant, as is the electromotive intensity $\mathcal{E}$, which is defined in terms of the non-Galilean invariant electric field $\boldsymbol{e}$, magnetic field $\boldsymbol{b}$, and displacement $\boldsymbol{u}$ by

$$\mathcal{E} \equiv \boldsymbol{e} + \dot{\boldsymbol{u}} \times \boldsymbol{b}, \tag{3.1.5}$$

where $\dot{(\ )} = \mathrm{d}(\ )/\mathrm{d}t$ denotes the material time derivative. The relation between current position $\boldsymbol{x}$, reference position $\boldsymbol{X}$, and displacement $\boldsymbol{u}$ of a material point is

$$\boldsymbol{x} = \boldsymbol{X} + \boldsymbol{u}. \tag{3.1.6}$$

Recall that the flux derivative for any vector field $\boldsymbol{f}$ is defined by

$$\overset{*}{\boldsymbol{f}} \equiv \frac{\partial \boldsymbol{f}}{\partial t} + \dot{\boldsymbol{u}}(\boldsymbol{\triangledown} \bullet \boldsymbol{f}) - \boldsymbol{\triangledown} \times (\dot{\boldsymbol{u}} \times \boldsymbol{f}) = \dot{\boldsymbol{f}} - (\dot{\boldsymbol{u}}\boldsymbol{\triangledown}) \bullet \boldsymbol{f} + \boldsymbol{f}(\boldsymbol{\triangledown} \bullet \dot{\boldsymbol{u}}) \tag{3.1.7}$$

and satisfies

$$\frac{\mathrm{d}}{\mathrm{d}t} \int_{s(t)} \boldsymbol{f} \bullet \boldsymbol{n} \, \mathrm{d}s = \int_{s(t)} \overset{*}{\boldsymbol{f}} \bullet \boldsymbol{n} \, \mathrm{d}s, \tag{3.1.8}$$

thus justifying the pointwise form of Faraday's law in equation $(3.1.4)_1$.

The nonexistence of magnetic charge in integral form is expressed by

$$\int_{\partial v(t)} \boldsymbol{b} \bullet \boldsymbol{n} \, \mathrm{d}s = 0. \tag{3.1.9}$$

The pointwise equation and interface condition follow as in the case of Gauss' law in equation (3.1.2),

$$\boldsymbol{\triangledown} \bullet \boldsymbol{b} = 0, \ \boldsymbol{n} \bullet [\![\boldsymbol{b}]\!] = 0. \tag{3.1.10}$$

The fourth and final electromagnetic conservation law is Ampere's equation, which states that the circulation of the magnetomotive intensity $\mathcal{H}$ about a closed circuit $\partial s(t)$ is equal to the total current flux through the surface $s(t)$ which is bounded by $\partial s(t)$,

$$\oint_{\partial s(t)} \mathcal{H} \bullet \boldsymbol{s} \, \mathrm{d}l = \frac{\mathrm{d}}{\mathrm{d}t} \int_{s(t)} \boldsymbol{d} \bullet \boldsymbol{n} \, \mathrm{d}s + \int_{s(t)} \mathcal{J} \bullet \boldsymbol{n} \, \mathrm{d}s. \tag{3.1.11}$$

The first term on the right hand side of equation (3.1.11) is the displacement current flux through $s(t)$ while the second term accounts for the induction current. Note that the magnetomotive intensity $\mathcal{H}$ and the conduction current density $\mathcal{J}$ are both Galilean invariant. Similar arguments to those used for the Faraday law in equation 3.1.4 lead to the pointwise form of Ampere's equation and the associated interface condition, namely

$$\boldsymbol{\triangledown} \times \mathcal{H} = \overset{*}{\boldsymbol{d}} + \mathcal{J}, \ \boldsymbol{n} \times [\![\mathcal{H}]\!] = \boldsymbol{0}. \tag{3.1.12}$$

Note that according to the simplifying assumption discussed at the beginning of this subsection there is no surface electric current taken into account. The magnetomotive intensity $\mathcal{H}$ and conduction current density $\mathcal{J}$ are defined as

$$\mathcal{H} \equiv \boldsymbol{h} - \dot{\boldsymbol{u}} \times \boldsymbol{d}, \ \mathcal{J} \equiv \boldsymbol{j} - q\dot{\boldsymbol{u}}, \tag{3.1.13}$$

where $\boldsymbol{h}$ is the H field and $\boldsymbol{j}$ is the electric current density.[2]

In addition to the four electromagnetic conservation laws, five additional principles are needed, three from mechanics and two from thermodynamics. First is conservation of mass, which in integral form states

$$\frac{\mathrm{d}}{\mathrm{d}t} \int_{v(t)} \rho \, \mathrm{d}v = 0, \tag{3.1.14}$$

where ρ is the mass density. The arbitrariness of the control volume, which always follows the same set of material points, yields the pointwise equation

$$\dot{\rho} + \rho(\boldsymbol{\triangledown} \bullet \dot{\boldsymbol{u}}) = 0. \tag{3.1.15}$$

For simplicity, it is assumed here and subsequently that all discontinuities propagate at the speed of the material. Consequently no jump condition is needed for mass conservation.

The next mechanics principle is that of conservation of linear momentum, generalized for the electromagnetic-mechanical system. In integral form this is given by

$$\frac{\mathrm{d}}{\mathrm{d}t} \int_{v(t)} \rho \boldsymbol{g} \, \mathrm{d}v = \int_{v(t)} \rho \boldsymbol{f} \, \mathrm{d}v + \int_{\partial v(t)} \boldsymbol{t} \, \mathrm{d}s, \tag{3.1.16}$$

where $\boldsymbol{g}$ is the generalized electromagnetic-mechanical momentum (to be specified subsequently), $\boldsymbol{f}$ is the mechanical body force, and $\boldsymbol{t}$ is the generalized electromagnetic-mechanical traction on the surface of the control volume (also to be specified subsequently). It is further assumed that Cauchy's formula relates the electromagnetic-mechanical surface traction $\boldsymbol{t}$ to $\boldsymbol{\sigma}$, the generalized electromagnetic-mechanical (Maxwell) stress,

$$\boldsymbol{t} = \boldsymbol{n} \bullet \boldsymbol{\sigma}. \tag{3.1.17}$$

---

[2]The fields $\boldsymbol{b}$ and $\boldsymbol{h}$ are denoted here as the magnetic field and H field, respectively. In the literature they are also referred to as the magnetic flux and magnetic field, respectively, and $\boldsymbol{h}$ is often denoted as the current potential (Kovetz, 2000).

The pointwise form of the conservation of linear momentum and the associated interface condition follow from the arbitrariness of the control volume, by using standard arguments which involve Gauss' divergence theorem,

$$\rho \dot{\boldsymbol{g}} = \boldsymbol{\nabla} \bullet \boldsymbol{\sigma} + \rho \boldsymbol{f}, \ \boldsymbol{n} \bullet [\![\boldsymbol{\sigma}]\!] = \boldsymbol{t}, \tag{3.1.18}$$

where $\boldsymbol{t}$ in the jump condition is the applied mechanical surface traction.

The third mechanics principle is the conservation of angular momentum, generalized for the electromagnetic-mechanical system, which states[3]

$$\frac{\mathrm{d}}{\mathrm{d}t} \int_{v(t)} \boldsymbol{x} \wedge \rho \boldsymbol{g} \, \mathrm{d}v = \int_{v(t)} \boldsymbol{x} \wedge \rho \boldsymbol{f} \, \mathrm{d}v + \int_{\partial v(t)} \boldsymbol{x} \wedge \boldsymbol{t} \, \mathrm{d}s. \tag{3.1.19}$$

The pointwise form follows from the arbitrariness of the control volume and the use of mass and linear momentum conservation in equations (3.1.15) and (3.1.18)

$$\rho \dot{\boldsymbol{u}} \wedge \boldsymbol{g} = \boldsymbol{\sigma}^T - \boldsymbol{\sigma}. \tag{3.1.20}$$

Note that no associated interface condition is needed since all interfaces propagate at the speed of the material.

The first thermodynamic principle pertains to the balance of power, which states that the rate of change of the control volume's internal energy is equal to the power supplied externally, i.e.

$$\begin{aligned}
\frac{\mathrm{d}}{\mathrm{d}t} \int_{v(t)} \rho \epsilon \, \mathrm{d}v = {}& \int_{v(t)} \rho \boldsymbol{f} \bullet \dot{\boldsymbol{u}} \, \mathrm{d}v + \int_{\partial v(t)} \boldsymbol{t} \bullet \dot{\boldsymbol{u}} \, \mathrm{d}s \\
& + \int_{v(t)} \rho h \, \mathrm{d}v + \int_{\partial v(t)} (-\boldsymbol{q}) \bullet \boldsymbol{n} \, \mathrm{d}s \\
& + \int_{\partial v(t)} (-\boldsymbol{\mathcal{E}} \times \boldsymbol{\mathcal{H}}) \bullet \boldsymbol{n} \, \mathrm{d}s,
\end{aligned} \tag{3.1.21}$$

---

[3]Recall that the wedge product is defined as $\boldsymbol{a} \wedge \boldsymbol{b} = \boldsymbol{ab} - \boldsymbol{ba}$.

where ϵ is the specific internal energy. The first line in the right hand side of equation (3.1.21) is the supplied mechanical power, where the first term is the body force contribution and the second term is the surface traction contribution. The second line in the right hand side of equation (3.1.21) is the supplied thermal power, where the first term accounts for internal heating and the second term accounts for surface heating. The specific rate of heating, i.e. the rate of heating per mass, is denoted by h and the heat flux through the surface is denoted by q and is oriented such that a positive value indicates heat flux out of the control volume.[4] Finally, the third line in the right hand side of equation (3.1.21) is the supplied electromagnetic power through the surface. The electromagnetic energy flux is given by the Poynting vector $\mathcal{E} \times \mathcal{H}$, again oriented such that a positive value indicates energy flux out of the control volume. The pointwise form of the energy balance and the associated interface condition follow once again from the arbitrariness of the control volume using standard arguments involving Gauss' divergence theorem, namely

$$\rho\dot{\epsilon} = \rho(f \bullet \dot{u} + h) + \triangledown \bullet (\sigma \bullet \dot{u} - q - \mathcal{E} \times \mathcal{H}),$$

$$n \bullet [\![-\sigma \bullet \dot{u} + q + \mathcal{E} \times \mathcal{H}]\!] = 0. \tag{3.1.22}$$

The second thermodynamic principle is the entropy production inequality, which states that the rate of change of the control volume's entropy must be greater than or equal to the entropy supplied to it, i.e.

$$\frac{\mathrm{d}}{\mathrm{d}t} \int_{v(t)} \rho s \, \mathrm{d}v \geqslant \int_{v(t)} \rho \frac{h}{T} \, \mathrm{d}v + \int_{\partial v(t)} \left(\frac{-q}{T}\right) \bullet n \, \mathrm{d}s, \tag{3.1.23}$$

where s is the specific entropy[5] and T is the absolute temperature. The first term in the

---

[4]The reader must not confuse the scalar specific rate of heating h with the vector H field h nor the vector heat flux q with the scalar volumetric charge q.

[5]The reader must not confuse the scalar specific entropy s with the line tangent vector s.

right hand side of equation (3.1.23) accounts for the entropy supplied by the internal heating, and the second term accounts for the entropy supplied by the heat flux through the surface of the control volume. The integral form provides, through the same arguments used for the energy balance in equation (3.1.22), the pointwise entropy production inequality and associated jump condition,

$$\rho \dot{s} \geqslant \frac{\rho h}{T} + \nabla \bullet \left(\frac{-\boldsymbol{q}}{T} \right), \ \boldsymbol{n} \bullet \left[\!\left[\frac{\boldsymbol{q}}{T} \right]\!\right] \geqslant 0. \tag{3.1.24}$$

With the necessary balance laws in place, the method of Coleman and Noll (Coleman and Noll, 1963) is used to find the material's constitutive laws. In order to do so, one needs first the electromagnetic constitutive laws in the current configuration. For simplicity, and motivated by the EMF applications of interest, it is assumed that the magnetization and polarization of the material are negligible and hence

$$\boldsymbol{d} = \epsilon_0 \boldsymbol{e}, \ \boldsymbol{h} = \frac{1}{\mu_0} \boldsymbol{b}, \tag{3.1.25}$$

where ϵ_0 is the permittivity of free space and μ_0 is the permeability of free space. The next piece of information required pertains to the specific free energy ψ, which is defined by (see Kovetz (2000))

$$\begin{aligned} \rho \psi \equiv{}& \rho \epsilon - T \rho s - \rho(\boldsymbol{g} \bullet \dot{\boldsymbol{u}}) + \frac{\rho}{2}(\dot{\boldsymbol{u}} \bullet \dot{\boldsymbol{u}}) \\ & - \frac{\epsilon_0}{2}(\boldsymbol{e} \bullet \boldsymbol{e}) - \frac{1}{2\mu_0}(\boldsymbol{b} \bullet \boldsymbol{b}) + (\boldsymbol{d} \times \boldsymbol{b}) \bullet \dot{\boldsymbol{u}}. \end{aligned} \tag{3.1.26}$$

This states that ψ equals the total specific internal energy less the energy due to thermal, kinetic, and electromagnetic sources (the expression in equation (3.1.26) also assumes that there is no polarization or magnetization in the material).

For the case of non-dissipative, non-magnetizable, and non-polarizable materials, it

is assumed that the specific free energy[6]

$$\psi = \psi(\boldsymbol{F}, \, T), \tag{3.1.27}$$

where $\boldsymbol{F}$ is the deformation gradient, $\boldsymbol{F} = \partial \boldsymbol{x} / \partial \boldsymbol{X}$. From the pointwise energy balance in equation (3.1.22) the expression for ρh is substituted into the entropy production inequality. Rearranging the result using equations (3.1.15), (3.1.25), and (3.1.26), the pointwise entropy production inequality (3.1.24) can be rewritten as

$$
\begin{aligned}
&\left[\boldsymbol{\sigma}^T - \rho \left(\frac{\partial \psi}{\partial \boldsymbol{F}} \right) \bullet \boldsymbol{F}^T + \epsilon_0 \left(\frac{1}{2} (\boldsymbol{e} \bullet \boldsymbol{e}) \boldsymbol{I} - \boldsymbol{e}\boldsymbol{e} \right) \right.\\
&\left. + \frac{1}{\mu_0} \left(\frac{1}{2} (\boldsymbol{b} \bullet \boldsymbol{b}) \boldsymbol{I} - \boldsymbol{b}\boldsymbol{b} \right) - (\boldsymbol{d} \times \boldsymbol{b}) \dot{\boldsymbol{u}} \right] \overset{\bullet}{\underset{\bullet}{\cdot}} (\dot{\boldsymbol{u}} \boldsymbol{\nabla}) \\
&- \rho \left[\frac{\partial \psi}{\partial T} + s \right] \dot{T} - [\rho \boldsymbol{g} - \rho \dot{\boldsymbol{u}} - \boldsymbol{d} \times \boldsymbol{b}] \bullet \ddot{\boldsymbol{u}} \\
&+ \boldsymbol{\mathcal{J}} \bullet \boldsymbol{\mathcal{E}} + \left(\frac{-\boldsymbol{q}}{T} \right) \bullet \boldsymbol{\nabla} T \geqslant 0.
\end{aligned}
\tag{3.1.28}
$$

This inequality must hold for any admissible thermodynamic process, i.e. for arbitrary $\dot{\boldsymbol{u}}\boldsymbol{\nabla}$, $\dot{T}$, and $\ddot{\boldsymbol{u}}$, which implies that the terms grouped in brackets must be zero. The vanishing of the term multiplying $\dot{\boldsymbol{u}}\boldsymbol{\nabla}$ provides the electromagnetic-mechanical stress expression sought

$$
\begin{aligned}
\boldsymbol{\sigma} = \rho \boldsymbol{F} \bullet \left(\frac{\partial \psi}{\partial \boldsymbol{F}} \right)^T + \epsilon_0 \left(\boldsymbol{e}\boldsymbol{e} - \frac{1}{2} (\boldsymbol{e} \bullet \boldsymbol{e}) \boldsymbol{I} \right) \\
+ \frac{1}{\mu_0} \left(\boldsymbol{b}\boldsymbol{b} - \frac{1}{2} (\boldsymbol{b} \bullet \boldsymbol{b}) \boldsymbol{I} \right) + \dot{\boldsymbol{u}} (\boldsymbol{d} \times \boldsymbol{b}).
\end{aligned}
\tag{3.1.29}
$$

The electromagnetic-mechanical stress can be divided into mechanical, $\boldsymbol{\sigma}_m$, and electro-

---

[6]In general ψ is taken as a function of $\boldsymbol{F}$, T, $\dot{\boldsymbol{u}}$, $\boldsymbol{\mathcal{E}}$, $\boldsymbol{B}$, and $\boldsymbol{\nabla} T$. For details, see Kovetz (2000).

magnetic, σ_{em}, parts

$$\sigma = \sigma_m + \sigma_{em}$$

$$\sigma_m \equiv \rho \boldsymbol{F} \cdot \left(\frac{\partial \psi}{\partial \boldsymbol{F}}\right)^T \tag{3.1.30}$$

$$\sigma_{em} \equiv \epsilon_0 \left(\boldsymbol{ee} - \frac{1}{2}(\boldsymbol{e} \cdot \boldsymbol{e})\boldsymbol{I}\right) + \frac{1}{\mu_0}\left(\boldsymbol{bb} - \frac{1}{2}(\boldsymbol{b} \cdot \boldsymbol{b})\boldsymbol{I}\right) + \dot{\boldsymbol{u}}(\boldsymbol{d} \times \boldsymbol{b}).$$

Although for simplicity (and without loss of generality) it is assumed that the material is hyperelastic, in general the mechanical stress may be given in rate form, as a function of $\boldsymbol{F}$ and T and some internal variables. Evolution laws for the internal variables would be necessary to complete the mechanical constitutive description.

The vanishing of the term multiplying $\dot{T}$ in equation (3.1.28) provides the entropy relation

$$s = -\frac{\partial \psi}{\partial T}, \tag{3.1.31}$$

while the vanishing of the term multiplying $\ddot{\boldsymbol{u}}$ in equation (3.1.28) provides the electromagnetic-mechanical momentum relation

$$\boldsymbol{g} = \dot{\boldsymbol{u}} + \frac{1}{\rho}(\boldsymbol{d} \times \boldsymbol{b}). \tag{3.1.32}$$

One can now verify using equations (3.1.29) and (3.1.32) that the angular momentum balance in equation (3.1.20) is satisfied.

Upon taking into account equations (3.1.29), (3.1.31), and (3.1.32), the final form of the entropy inequality equation (3.1.28) is

$$\mathcal{J} \cdot \mathcal{E} + \left(\frac{-\boldsymbol{q}}{T}\right) \cdot \nabla T \geqslant 0. \tag{3.1.33}$$

Substituting for $\boldsymbol{g}$ from equation (3.1.32) into the pointwise linear momentum equation (3.1.18) one obtains

$$\nabla \cdot \sigma + \rho \boldsymbol{f} = \rho \frac{\mathrm{d}}{\mathrm{d}t}\left(\frac{1}{\rho}(\boldsymbol{d} \times \boldsymbol{b})\right) + \rho \ddot{\boldsymbol{u}}. \tag{3.1.34}$$

Using the definition of $\boldsymbol{\sigma}$ from equation (3.1.29), and Maxwell's equations (3.1.2), (3.1.4), (3.1.10), and (3.1.12), the above equation of motion may be further simplified to the more physically transparent form

$$\nabla \bullet \boldsymbol{\sigma}_m + \boldsymbol{j} \times \boldsymbol{b} + q\boldsymbol{e} + \rho\boldsymbol{f} = \rho\ddot{\boldsymbol{u}}, \tag{3.1.35}$$

which shows that the divergence of the mechanical stress $\boldsymbol{\sigma}_m$ plus the Lorentz force terms, $\boldsymbol{j} \times \boldsymbol{b} + q\boldsymbol{e}$, plus the mechanical body force $\rho\boldsymbol{f}$ equal the inertia term $\rho\ddot{\boldsymbol{u}}$. It is worth noting that the Lorentz force terms have appeared as a result of the generalized electromagnetic-mechanical stress, without assuming their existence a priori.

3.1.2 Transformation of Field Quantities from Current to Reference Configuration

Kinematic relations from continuum mechanics are now used to obtain the relations between current and reference configuration fields and to transform the previous conservation laws to their reference configuration counterpart. To this end, one needs the three equations relating volume elements, oriented line elements, and oriented surface elements in the reference and current configurations (the last of which is Nanson's formula), namely[7]

$$\mathrm{d}v = J \, \mathrm{d}V, \ \boldsymbol{s} \, \mathrm{d}l = \left(\boldsymbol{F} \bullet \boldsymbol{S}\right) \mathrm{d}L, \ \boldsymbol{n} \, \mathrm{d}s = J\left(\boldsymbol{N} \bullet \boldsymbol{F}^{-1}\right) \mathrm{d}S; \ J = \det(\boldsymbol{F}) \tag{3.1.36}$$

where $\boldsymbol{S}$ is the tangent to the line element $\mathrm{d}L$ in the reference configuration and $\boldsymbol{N}$ is the normal to the surface element $\mathrm{d}S$ in the reference configuration.

Beginning with conservation of charge, equation (3.1.1), and using equation (3.1.36) to transform the integration from current to reference configuration yields

$$\int_{\partial V} \left(J\boldsymbol{F}^{-1} \bullet \boldsymbol{d}\right) \bullet \boldsymbol{N} \, \mathrm{d}S = \int_V Jq \, \mathrm{d}V. \tag{3.1.37}$$

---

[7]Here and subsequently capital letters will be used to designate field quantities in the reference configuration corresponding to the lowercase field in the current configuration.

This implies the definitions

$$D \equiv JF^{-1} \bullet d, \; Q \equiv Jq, \tag{3.1.38}$$

where D is the reference configuration electric displacement and Q is the reference configuration volume charge density. The pointwise Gauss' equation in the reference configuration and the interface condition follow from the arbitrariness of the reference configuration control volume using standard arguments as in the current configuration case in equation (3.1.2), namely

$$\nabla \bullet D = Q, \; N \bullet [\![D]\!] = 0. \tag{3.1.39}$$

Note that whereas $\mathbf{v}$ is the gradient operator in the current configuration, ∇ is the gradient operator in the reference configuration.

Next, the kinematic relations in equation (3.1.36) are applied to Faraday's law in equation (3.1.3), which yields

$$\oint_{\partial S} (\mathcal{E} \bullet F) \bullet S \, \mathrm{d}L = -\frac{\mathrm{d}}{\mathrm{d}t} \int_{S} (JF^{-1} \bullet b) \bullet N \, \mathrm{d}S. \tag{3.1.40}$$

This leads to the definitions

$$E \equiv \mathcal{E} \bullet F, \; B \equiv JF^{-1} \bullet b, \tag{3.1.41}$$

where E is the electromotive intensity in the reference configuration and B is the magnetic field in the reference configuration. The pointwise Faraday's equation and associated interface condition in the reference configuration follow, similarly to the current configuration case,

$$\nabla \times E = -\dot{B}, \; N \times [\![E]\!] = 0. \tag{3.1.42}$$

Note also that the reference configuration relations are simple to derive since the reference configuration is independent of time.

Attention is focused next to the non-existence of magnetic charge, equation (3.1.9), which with the help of equation (3.1.36) gives in the reference configuration

$$\int_{\partial V} \left(J\boldsymbol{F}^{-1} \bullet \boldsymbol{b} \right) \bullet \boldsymbol{N} \, \mathrm{d}S = 0. \tag{3.1.43}$$

Using the previous definition for $\boldsymbol{B}$ in equation (3.1.41) leads to the pointwise statement and associated interface condition in the reference configuration,

$$\boldsymbol{\nabla} \bullet \boldsymbol{B} = 0, \ \boldsymbol{N} \bullet [\![\boldsymbol{B}]\!] = 0. \tag{3.1.44}$$

The transformation of Ampere's law in the reference configuration comes from applying equation (3.1.36) to equation (3.1.11), yielding

$$\oint_{\partial S} (\boldsymbol{\mathcal{H}} \bullet \boldsymbol{F}) \bullet \boldsymbol{S} \, \mathrm{d}L = \frac{\mathrm{d}}{\mathrm{d}t} \int_S \left(J\boldsymbol{F}^{-1} \bullet \boldsymbol{d} \right) \bullet \boldsymbol{N} \, \mathrm{d}S + \int_S \left(J\boldsymbol{F}^{-1} \bullet \boldsymbol{\mathcal{J}} \right) \bullet \boldsymbol{N} \, \mathrm{d}S. \tag{3.1.45}$$

This leads to the definitions

$$\boldsymbol{H} \equiv \boldsymbol{\mathcal{H}} \bullet \boldsymbol{F}, \ \boldsymbol{J} \equiv J\boldsymbol{F}^{-1} \bullet \boldsymbol{\mathcal{J}}, \tag{3.1.46}$$

where $\boldsymbol{H}$ is the magnetomotive intensity in the reference configuration and $\boldsymbol{J}$ is the conduction electric current density in the reference configuration.[8] With these definitions, the pointwise Ampere's equation and interface condition in the reference configuration follow in a similar fashion as for the current configuration case, equation (3.1.12),

$$\boldsymbol{\nabla} \times \boldsymbol{H} = \dot{\boldsymbol{D}} + \boldsymbol{J}, \ \boldsymbol{N} \times [\![\boldsymbol{H}]\!] = \boldsymbol{0}. \tag{3.1.47}$$

Having established Maxwell's equations in the reference configuration attention is turned next to the mechanical conservation laws. The statement of conservation of mass, equation (3.1.14), is transformed to the reference configuration using equation (3.1.36),

$$\frac{\mathrm{d}}{\mathrm{d}t} \int_V J\rho \, \mathrm{d}V = 0, \tag{3.1.48}$$

---

[8]The reader must not confuse the vector conduction electric current density in the reference configuration $\boldsymbol{J}$ with the scalar density for volume change $J = \det(\boldsymbol{F})$.

which leads to the definition

$$\rho_0 \equiv J\rho, \tag{3.1.49}$$

where ρ_0 is the mass density in the reference configuration. The pointwise mass conservation equation in the reference configuration, counterpart of equation (3.1.15), is therefore

$$\dot{\rho}_0 = 0. \tag{3.1.50}$$

To find the relations between current and reference configuration stress and traction fields, one needs the conservation of linear momentum and Cauchy tetrahedron argument equation (3.1.17). Transforming equations (3.1.16) and (3.1.17) with the help of equation (3.1.36) yields

$$\frac{\mathrm{d}}{\mathrm{d}t} \int_V J\rho \boldsymbol{g} \, \mathrm{d}V = \int_V J\rho \boldsymbol{f} \, \mathrm{d}V + \int_{\partial V} \boldsymbol{t} \frac{\mathrm{d}s}{\mathrm{d}S} \, \mathrm{d}S \tag{3.1.51}$$

and

$$\boldsymbol{T} = \boldsymbol{N} \bullet \boldsymbol{\Pi}. \tag{3.1.52}$$

This implies the definitions

$$\boldsymbol{T} \equiv \boldsymbol{t} \frac{\mathrm{d}s}{\mathrm{d}S}, \ \boldsymbol{\Pi} \equiv J\boldsymbol{F}^{-1} \bullet \boldsymbol{\sigma}, \tag{3.1.53}$$

where $\boldsymbol{T}$ is the surface traction in the reference configuration and $\boldsymbol{\Pi}$ is the electromagnetic-mechanical first Piola-Kirchhoff stress.[9] Cauchy's formula (equation (3.1.17)) and Nanson's formula (equation (3.1.36)) lead to the second part of equation (3.1.52). With these definitions, the pointwise equation of motion and corresponding interface condition in the reference configuration which follow from equations (3.1.51), (3.1.52), and

---

[9]The reader must not confuse the vector surface traction in the reference configuration $\boldsymbol{T}$ with the scalar temperature T.

(3.1.53), in a similar fashion that equation (3.1.18) followed from equations (3.1.16) and (3.1.17), are

$$\rho_0 \dot{\boldsymbol{g}} = \boldsymbol{\nabla} \bullet \boldsymbol{\Pi} + \rho_0 \boldsymbol{f}, \ \boldsymbol{N} \bullet [\![\boldsymbol{\Pi}]\!] = \boldsymbol{T}. \tag{3.1.54}$$

The above derived reference configuration expressions for the current configuration field quantities introduced in Section 3.1.1 are the indispensable ingredients for the variational approach that follows.

3.1.3 Variational Approach (Reference Configuration)

One of the most efficient ways to obtain Maxwell's equations, in the current configuration, through a variational approach (Hamilton's principle, see Lazzari and Nibbi (2000)) is based on a potential formulation such that Faraday's equation, equation (3.1.4), and the statement of no magnetic charges, equation (3.1.10), are satisfied identically. A vector potential, $\boldsymbol{a}$, and scalar potential, ϕ, are defined such that

$$\boldsymbol{b} = \boldsymbol{\nabla} \times \boldsymbol{a}, \ \boldsymbol{e} = -\boldsymbol{\nabla}\phi - \frac{\partial \boldsymbol{a}}{\partial t}. \tag{3.1.55}$$

The potentials in this formulation are not uniquely determined. A gauge condition must be applied for unique potentials, which will be discussed subsequently.

This potential formulation reduces the number of non-automatically satisfied Maxwell's equations to two. A purely electromagnetic Lagrangian density exists in terms of the generalized coordinates $\boldsymbol{a}$ and ϕ such that the Euler-Lagrange equations of the corresponding (Hamilton's) variational principle are Gauss' and Ampere's equations. This Lagrangian density is

$$\ell \equiv \frac{\epsilon_0}{2}(\boldsymbol{e} \bullet \boldsymbol{e}) - \frac{1}{2\mu_0}(\boldsymbol{b} \bullet \boldsymbol{b}) + \boldsymbol{j} \bullet \boldsymbol{a} - q\phi, \tag{3.1.56}$$

where $\boldsymbol{e}$ and $\boldsymbol{b}$ are in terms of $\boldsymbol{a}$ and ϕ through equation (3.1.55).

In order to transform the current configuration electromagnetic Lagrangian density to its reference configuration counterpart, the vector and scalar potentials must be trans-

formed accordingly. Substituting equation (3.1.41) into equation (3.1.55) yields after
some manipulation (see Nelson (1979) for details)

$$\boldsymbol{B} = \boldsymbol{\nabla} \times \boldsymbol{A}$$

$$\boldsymbol{E} = -\boldsymbol{\nabla}\Phi - \dot{\boldsymbol{A}}, \tag{3.1.57}$$

where the reference configuration vector potential $\boldsymbol{A}$ and reference configuration scalar
potential Φ are given in terms of their current configuration counterparts by

$$\boldsymbol{A} = \boldsymbol{a} \bullet \boldsymbol{F}$$

$$\Phi = \phi - \dot{\boldsymbol{u}} \bullet \boldsymbol{a}. \tag{3.1.58}$$

As in the current configuration, the reference configuration potential formulation iden-
tically satisfies Faraday's equation, equation (3.1.42), and the statement of no magnetic
charges, equation (3.1.44). Notice that these reference configuration potentials are still
not unique, requiring a gauge condition.

With this formulation, the reference configuration Lagrangian for the full electromag-
netic-mechanical case can now be obtained by adding the mechanical energy component
to the electromagnetic part in equation (3.1.56). To achieve this one first needs to define
the auxiliary term $\boldsymbol{E}^*$ as

$$\boldsymbol{E}^* \equiv \boldsymbol{E} - \left(\boldsymbol{F}^{-1} \bullet \dot{\boldsymbol{u}}\right) \times \boldsymbol{B} \tag{3.1.59}$$

(where $\boldsymbol{E}^*$ is not to be confused with a flux derivative term). Then, given that the la-
grangian density ℓ transforms to the reference configuration as $J\ell$, adding the necessary
mechanical energy terms, and substituting for the current configuration fields in terms
of the reference configuration fields with equations (3.1.5), (3.1.38), (3.1.41), (3.1.46),

(3.1.57), and (3.1.59) yields the reference configuration Lagrangian

$$
\mathcal{L} \equiv \int_{\mathbb{R}^3} \left(J\ell + \rho_0 \left(\frac{1}{2}(\dot{u} \bullet \dot{u}) - \psi(C) + f \bullet u \right) \right) \, dV + \int_{\partial\Omega} T \bullet u \, dS
$$

$$
= \int_{\mathbb{R}^3} \left(\frac{\epsilon_0 J}{2} \left(E^* \bullet C^{-1} \bullet E^* \right) - \frac{1}{2\mu_0 J} \left(B \bullet C \bullet B \right) \right. \tag{3.1.60}
$$

$$
\left. + J \bullet A - Q\Phi + \rho_0 \left(\frac{1}{2} \left(\dot{u} \bullet \dot{u} \right) - \psi(C) + f \bullet u \right) \right) \, dV + \int_{\partial\Omega} T \bullet u \, dS,
$$

where the independent fields are Φ, A, and u and $C = F^T \bullet F$ is the right Cauchy-Green tensor. Here Ω is the domain occupied by the body, and $\partial\Omega$ is the surface of this body. Notice that the density $\rho_0(X) \neq 0$ for $X \in \Omega$ and $\rho_0(X) = 0$ for $X \in \mathbb{R}^3 - \Omega$. Integration over $\mathbb{R}^3$ is necessary since electric and magnetic fields exist not only in the solid ($X \in \Omega$) but also in its surrounding space ($X \in \mathbb{R}^3 - \Omega$). Moreover, note that Φ and u are assumed continuous throughout $\mathbb{R}^3$, but only the tangent component of A, i.e. A_t, is assumed continuous across an interface.

Hamilton's principle states that the action integral $\mathcal{F}$, defined as the integral of the Lagrangian defined in equation (3.1.60) over the time interval $[t_1, t_2]$, is stationary[10]

$$
\delta\mathcal{F} = 0, \ \mathcal{F} \equiv \int_{t_1}^{t_2} \mathcal{L} \, dt, \tag{3.1.61}
$$

where $\delta\Phi = 0$, $\delta A = 0$, and $\delta u = 0$ at $t = t_1$ and $t = t_2$. The resulting Euler-Lagrange equations are the governing equations of the electromagnetic-mechanical system. More specifically:

---

[10]Here and subsequently δ denotes the variation of a functional.

Taking the variation of $\mathscr{F}$ with respect to Φ yields

$$\mathscr{F}_{,\Phi}[\delta\Phi] = \int\limits_{t_1}^{t_2} \left\{ \int\limits_{\mathbb{R}^3} \left(\boldsymbol{\nabla} \bullet \left(\epsilon_0 J \boldsymbol{E}^* \bullet \boldsymbol{C}^{-1} \right) - Q \right) \delta\Phi \, \mathrm{d}V \right.$$
$$\left. - \int\limits_{\partial\Omega} [\![\left(\boldsymbol{N} \bullet \left(\epsilon_0 J \boldsymbol{E}^* \bullet \boldsymbol{C}^{-1} \right) \right) \delta\Phi]\!] \, \mathrm{d}S \right\} \mathrm{d}t = 0, \qquad (3.1.62)$$

where integration by parts and Gauss' divergence theorem have been used. Using equations (3.1.5), (3.1.25), (3.1.38), (3.1.41), and (3.1.59) the reference configuration electromagnetic constitutive relation one observes that the group of terms appearing in parenthesis and brackets in equation (3.1.62) is the reference configuration electric displacement

$$\boldsymbol{D} = \epsilon_0 J \boldsymbol{E}^* \bullet \boldsymbol{C}^{-1}. \qquad (3.1.63)$$

Consequently equation (3.1.62) implies

$$\boldsymbol{\nabla} \bullet \boldsymbol{D} = Q, \ \boldsymbol{N} \bullet [\![\boldsymbol{D}]\!] = 0, \qquad (3.1.64)$$

that is Gauss' equation and interface condition in the reference configuration, equation (3.1.39), as expected.

Taking the variation of $\mathscr{F}$ with respect to $\boldsymbol{A}$ gives

$$\mathscr{F}_{,A}[\delta\boldsymbol{A}] = \int\limits_{t_1}^{t_2} \left\{ \int\limits_{\mathbb{R}^3} \left(\frac{\mathrm{d}}{\mathrm{d}t} \left(\epsilon_0 J \boldsymbol{E}^* \bullet \boldsymbol{C}^{-1} \right) - \boldsymbol{\nabla} \times \left(\left(\epsilon_0 J \boldsymbol{E}^* \bullet \boldsymbol{C}^{-1} \right) \right. \right. \right.$$
$$\left. \times \left(\boldsymbol{F}^{-1} \bullet \dot{\boldsymbol{u}} \right) + \frac{1}{\mu_0 J} \left(\boldsymbol{B} \bullet \boldsymbol{C} \right) \right) + \boldsymbol{J} \right) \bullet \delta\boldsymbol{A} \, \mathrm{d}V$$
$$- \int\limits_{\partial\Omega} [\![\left(\boldsymbol{N} \times \left(\left(\epsilon_0 J \boldsymbol{E}^* \bullet \boldsymbol{C}^{-1} \right) \times \left(\boldsymbol{F}^{-1} \bullet \dot{\boldsymbol{u}} \right) \right. \right. \qquad (3.1.65)$$
$$\left. \left. \left. + \frac{1}{\mu_0 J} \left(\boldsymbol{B} \bullet \boldsymbol{C} \right) \right) \right) \bullet \delta\boldsymbol{A}]\!] \, \mathrm{d}S \right\} \mathrm{d}t = 0,$$

where integration by parts, identities for triple products, and Stoke's theorem have been used. Similarly to equation (3.1.63), using equations (3.1.13), (3.1.25), (3.1.38), (3.1.41),

and (3.1.46) one observes that the group of terms appearing in parenthesis and brackets in equation (3.1.65) is the reference configuration H field

$$H = \frac{1}{\mu_0 J} (B \bullet C) - \left(F^{-1} \bullet \dot{u}\right) \times D. \tag{3.1.66}$$

Consequently equation (3.1.65) yields[11]

$$\nabla \times H = \dot{D} + J, \; N \times [\![H]\!] = 0, \tag{3.1.67}$$

which is Ampere's equation and the related interface condition, equation (3.1.47), in the reference configuration, again as expected.

Finally, the variation of $\mathscr{F}$ with respect to u will yield the equation of motion and surface traction condition in terms of the electromagnetic-mechanical momentum g and stress σ. Applying integration by parts and Gauss' divergence theorem gives the stationary condition

$$\mathscr{F}_{,u}[\delta u] = \int\limits_{t_1}^{t_2} \left\{ \int\limits_{\mathbb{R}^3} \left(\nabla \bullet \Pi - \frac{\mathrm{d}}{\mathrm{d}t} \left(\left(\left(\epsilon_0 J E^* \bullet C^{-1}\right) \times B\right) \bullet F^{-1}\right) \right. \right.$$
$$\left. - \rho_0 \ddot{u} + \rho_0 f \right) \bullet \delta u \; \mathrm{d}V \tag{3.1.68}$$
$$\left. - \int\limits_{\partial \Omega} \left(N \bullet [\![\Pi]\!] - T\right) \bullet \delta u \; \mathrm{d}S \right\} \mathrm{d}t = 0,$$

where the reference electromagnetic-mechanical first Piola-Kirchoff stress Π is given by

$$\Pi = \rho_0 \left(\frac{\partial \psi}{\partial F}\right)^T + \epsilon_0 J \left(\left(E^* \bullet C^{-1}\right)\left(C^{-1} \bullet E^*\right) \bullet F^T - \frac{1}{2}\left(E^* \bullet C^{-1} \bullet E^*\right) F^{-1}\right)$$
$$+ \frac{1}{\mu_0 J}\left(BB \bullet F^T - \frac{1}{2}\left(B \bullet C \bullet B\right) F^{-1}\right) + \left(F^{-1} \bullet \dot{u}\right)\left(D \times B\right) \bullet F^{-1}. \tag{3.1.69}$$

Consequently from equations (3.1.68) and (3.1.69) one obtains

$$\nabla \bullet \Pi + \rho_0 f = \frac{\mathrm{d}}{\mathrm{d}t}\left(\left(D \times B\right) \bullet F^{-1}\right) + \rho_0 \ddot{u} = \rho_0 \dot{g}, \; N \bullet [\![\Pi]\!] = T, \tag{3.1.70}$$

---

[11]By the definitions of N and A_t one has $[\![(N \times H) \bullet \delta A]\!] = (N \times [\![H]\!]) \bullet \delta A_t$.

which are the reference configuration equation of motion and interface condition of equation (3.1.54) as expected.

A final note is in order at this point. To complete the variational formulation presentation one must show that equation (3.1.70) transforms to their current configuration counterparts. Using the $\boldsymbol{\sigma}$-$\boldsymbol{\Pi}$ relation in equation (3.1.53) one has

$$\boldsymbol{\nabla} \bullet \boldsymbol{\Pi} = J(\boldsymbol{\triangledown} \bullet \boldsymbol{\sigma}). \tag{3.1.71}$$

Considering in addition equations (3.1.5), (3.1.25), (3.1.36), (3.1.38), (3.1.41), (3.1.50), and (3.1.59), the reference configuration equation and interface conditions of motion transform to equation (3.1.34) and the interface condition in equation (3.1.18), their current configuration counterparts derived with the direct method. It is thus shown that the variational method agrees with the direct method for Maxwell's equations and the equation of motion.

3.2   Eddy Current Formulation

For the EMF processes of interest the problem formulation may be simplified considerably by applying the eddy current approximation. Following the description of the eddy current approximation for the general 3-D case, the section proceeds with the axisymmetric version of this approximation and ends by presenting the modeling of the coil under a given current.

3.2.1   General Case in 3-D

The aspects typical of EMF processes that make this simplification appropriate: the material velocities are much less than the speed of light, the effective electric current frequencies are on the order of 10 kHz, the geometry is on the order of 1 cm, and the material electrical conductivities are large. Detailed discussion of this approximate formulation

may be found in the literature, e.g. in Hiptmair and Ostrowski (2005) and references cited therein. From the above assumptions follows that the eddy current approximation essentially consists of neglecting electric energy from the lagrangian ℓ in equation (3.1.56). Imposing the eddy current approximation implies displacement currents are neglected, which means volumetric charges are not accounted for and charge conservation must be imposed separately. The resulting approximate Lagrangian does not depend on Φ and Gauss' equation is no longer a result of the variational procedure.

With this approximation, the Lagrangian may be divided into kinetic energy, $\mathscr{K}$, and potential energy, $\mathscr{P}$, as

$$\mathscr{L} \equiv \mathscr{K} - \mathscr{P}, \tag{3.2.1}$$

where $\mathscr{K}$ and $\mathscr{P}$ are given by

$$\mathscr{K} \equiv \int_{\mathbb{R}^3} \frac{\rho_0}{2} \left(\dot{\boldsymbol{u}} \bullet \dot{\boldsymbol{u}} \right) \, \mathrm{d}V$$

$$\mathscr{P} \equiv \int_{\mathbb{R}^3} \left(\frac{1}{2\mu_0 J} \left(\boldsymbol{B} \bullet \boldsymbol{C} \bullet \boldsymbol{B} \right) - \boldsymbol{J} \bullet \boldsymbol{A} + \rho_0 \left(\Psi \left(\boldsymbol{C} \right) - \boldsymbol{f} \bullet \boldsymbol{u} \right) \right) \, \mathrm{d}V \tag{3.2.2}$$

$$- \int_{\partial\Omega} \boldsymbol{T} \bullet \boldsymbol{u} \, \mathrm{d}S.$$

The action integral $\mathscr{F}$ is formed by integrating $\mathscr{L}$ over a time interval $[t_1, t_2]$ and Hamilton's principle is applied as previously (see equation (3.1.61)). Taking the variation of $\mathscr{F}$ with respect to $\boldsymbol{A}$ gives

$$\mathscr{F}_{,A}[\delta \boldsymbol{A}] = \int_{t_1}^{t_2} \left\{ \int_{\mathbb{R}^3} \left(\boldsymbol{\nabla} \times \left(\frac{1}{\mu_0 J} \left(\boldsymbol{B} \bullet \boldsymbol{C} \right) \right) + \boldsymbol{J} \right) \bullet \delta \boldsymbol{A} \, \mathrm{d}V \right.$$

$$\left. - \int_{\partial\Omega} \left\llbracket \left(\boldsymbol{N} \times \left(\frac{1}{\mu_0 J} \left(\boldsymbol{B} \bullet \boldsymbol{C} \right) \right) \right) \bullet \delta \boldsymbol{A} \right\rrbracket \, \mathrm{d}S \right\} \mathrm{d}t = 0. \tag{3.2.3}$$

The eddy current simplification implies that the terms in parentheses in equation (3.2.3) are the reference configuration H field. From equation (3.1.66) and since $\mu_0 \epsilon_0 \ll 1$ one

can define the approximate H field by

$$H \equiv \frac{1}{\mu_0 J} \left(B \bullet C \right).$$ (3.2.4)

Thus the variation with respect to A results in the reference configuration approximate Ampere's equation and interface condition, given by

$$\nabla \times H = J, \ N \times [\![H]\!] = 0,$$ (3.2.5)

which agrees with equation (3.1.67) once the displacement current $\dot{D}$ is neglected.

Taking the variation of $\mathscr{F}$ with respect to u, one has

$$\mathscr{F}_{,u}[\delta u] = \int_{t_1}^{t_2} \left\{ \int_{\mathbb{R}^3} (\nabla \bullet \Pi - \rho_0 \ddot{u} + \rho_0 f) \bullet \delta u \ \mathrm{d}V \right.$$
$$\left. - \int_{\partial \Omega} (N \bullet [\![\Pi]\!] - T) \bullet \delta u \ \mathrm{d}S \right\} \mathrm{d}t = 0,$$ (3.2.6)

where the approximate nominal stress field Π has now been defined by

$$\Pi \equiv \rho_0 \left(\frac{\partial \Psi}{\partial F} \right)^T + \frac{1}{\mu_0 J} \left(BB \bullet F^T - \frac{1}{2} (B \bullet C \bullet B) F^{-1} \right).$$ (3.2.7)

Equation (3.2.6) implies the pointwise equation of motion and interface condition in the reference configuration,

$$\nabla \bullet \Pi + \rho_0 f = \rho_0 \ddot{u}, \ N \bullet [\![\Pi]\!] = T.$$ (3.2.8)

which results from equation (3.1.70) when electric displacement terms are neglected.

To complete the formulation charge conservation must be imposed separately, since it cannot follow from Hamilton's principle with the eddy current simplification. The reference configuration charge conservation equation and interface condition are

$$\nabla \bullet J = 0, \ N \bullet [\![J]\!] = 0$$ (3.2.9)

and must be imposed in addition to Hamilton's principle for the eddy current approxima-

tion.

To solve the governing equations (3.2.5), (3.2.8), and (3.2.9) the constitutive law for

J is needed. Here an isotropic Ohm's law with constant conductivity is assumed, given

by

$$j = \sigma(e + \dot{u} \times b) \Rightarrow J = \sigma J C^{-1} \bullet E. \tag{3.2.10}$$

3.2.2 Axisymmetric Processes

Implementing the aforementioned general theoretical formulation for axisymmetric

problems significantly simplifies the resulting formulation by reducing the independent

variables on the (*R,Z*) space to three (A_Θ, u_R, u_Z),[12] as it will be shown in the first sub-

section. However, special care must be taken with the axisymmetric formulation in the

forming coil under a given current, and this is the object of the second subsection.

3.2.2.1 Axisymmetric Formulation

The forming process of interest is assumed rotationally symmetric (in the z-direction),

implying that no field depends on the θ coordinate. The corresponding symmetry group

is C_∞, i.e. when the solution is invariant to coordinate transformations corresponding to

solid body rotations around the z-axis. From the assumed symmetry it is expected that

there is no hoop displacement ($u_\theta = 0$) and the only nonzero component of the current

density and electric field is the hoop component, i.e. $j = j_\theta i_\theta$ and $e = e_\theta i_\theta$. Also from

---

[12]Here and subsequently r, θ, and z are the current configuration cylindrical coordinates with respective unit vectors i_r, i_θ, and i_z, and R, Θ, and Z are the reference configuration cylindrical coordinates with respective unit vectors i_R, i_Θ, i_Z. Subscripts of r, θ, and z indicate fields in terms of current configuration coordinates, and subscripts of R, Θ, and Z indicate fields in terms of reference configuration coordinates.

symmetry, there is no hoop component of the magnetic field ($b_\theta = 0$). To summarize,

$$\frac{\partial(\ )}{\partial \theta} = 0; \ u_r, \ u_z \neq 0, \ u_\theta = 0; \ e_r, \ e_z = 0, \ e_\theta \neq 0;$$

$$b_r, \ b_z \neq 0, \ b_\theta = 0; \ j_r, \ j_z = 0, \ j_\theta \neq 0. \tag{3.2.11}$$

The above results are consistent with Ohm's law, equation (3.2.10). Moreover from the electric field - potential relation, equation (3.1.55), combined with equation (3.2.11), one obtains that

$$a_r, \ a_z = 0, \ a_\theta \neq 0; \frac{\partial \phi}{\partial r} = \frac{\partial \phi}{\partial z} = \frac{\partial \phi}{\partial \theta} = 0, \tag{3.2.12}$$

i.e. the only independent fields are a_θ, u_r, and u_z. Using the relations between current and reference configuration electric current and potentials, equations (3.1.46) and (3.1.58) respectively, one has in the reference configuration

$$\boldsymbol{u} = u_R \boldsymbol{i}_R + u_Z \boldsymbol{i}_Z, \ \boldsymbol{A} = A_\Theta \boldsymbol{i}_\Theta, \ \Phi = 0, \ \boldsymbol{J} = J_\Theta \boldsymbol{i}_\Theta, \tag{3.2.13}$$

where Φ may be chosen as any arbitrary constant and is here set to zero.

With this formulation in place, it is straightforward to show that the Coulomb gauge condition, charge conservation, and two associated interface conditions in the reference configuration are identically satisfied, that is

$$\boldsymbol{\nabla} \bullet \boldsymbol{A} = 0$$

$$\boldsymbol{N} \bullet [\![\boldsymbol{A}]\!] = 0$$

$$\boldsymbol{\nabla} \bullet \boldsymbol{J} = 0 \tag{3.2.14}$$

$$\boldsymbol{N} \bullet [\![\boldsymbol{J}]\!] = 0.$$

Note that whereas equations $(3.2.14)_3$ and $(3.2.14)_4$ must hold in 3-D processes as well, equations $(3.2.14)_1$ and $(3.2.14)_2$ are here a result of axisymmetry. In general, other gauge conditions may be chosen, and nonzero jumps in the normal of the vector potential may occur.

3.2.2.2 Forming Coil

Though the forming process of interest is assumed to be geometrically axisymmetric, the forming coil in reality must be a continuous spiral. In order to model such a coil in the axisymmetric framework, the formulation must include the driving electric field. The approach here is similar to that in Stiemer et al. (2006). Each coil turn is approximated as a stationary torus, unconnected geometrically from the other turns. It is required that the electric current density remain axisymmetric, which implies in each coil turn

$$\boldsymbol{J} = J_\Theta(R, Z)\boldsymbol{i}_\Theta. \tag{3.2.15}$$

Using equations (3.1.57) and (3.2.10) and recalling that the coil does not deform (reference and current configuration are the same), one has

$$J_R = 0 \Rightarrow \frac{\partial \Phi}{\partial R} = A_R = 0$$
$$J_Z = 0 \Rightarrow \frac{\partial \Phi}{\partial Z} = A_Z = 0. \tag{3.2.16}$$

Thus Φ is not a function of R or Z, and from equation (3.2.15) J_Θ is not a function of Θ. Since $J_\Theta = -\sigma \left(\left(\frac{1}{R} \right) \frac{\partial \Phi}{\partial \Theta} + \dot{A}_\Theta \right)$, $\frac{\partial \Phi}{\partial \Theta}$ must in view of equation (3.2.16) be a constant. Given ΔU_k, the change in the electric potential Φ over coil turn k,

$$\frac{\partial \Phi}{\partial \Theta} = \frac{\Delta U_k}{2\pi} \Rightarrow \boldsymbol{\nabla}\Phi = \left(\frac{\Delta U_k}{2\pi R} \right)\boldsymbol{i}_\Theta. \tag{3.2.17}$$

With this formulation, the electric potential drops in all the coils, ΔU_k, can be expressed in terms of the coil current $I(t)$ and the magnetic vector potential A_Θ as follows: Recall from Ohm's law, equation (3.2.10), that since the coil does not deform, $\boldsymbol{J} = \boldsymbol{j} = \sigma\boldsymbol{e} = \sigma\boldsymbol{E}$. Integrating over the cross section in the R-Z plane of a coil turn gives the total current in the coil, $I(t)$. Assuming the coil has a rectangular cross section in the

R-Z plane aligned with the *R-Z* axes

$$
\begin{aligned}
I(t) &= \int_{S_k} \boldsymbol{J} \bullet \boldsymbol{n}_k \, \mathrm{d}S \\
&= -\sigma \int_{S_k} (\boldsymbol{\nabla}\Phi + \dot{\boldsymbol{A}}) \bullet \boldsymbol{i}_\Theta \, \mathrm{d}S \\
&= -\sigma \int_{S_k} \left(\dot{A}_\Theta + \frac{\Delta U_k}{2\pi R} \right) \, \mathrm{d}S \\
&= -\sigma \int_{S_k} \dot{A}_\Theta \, \mathrm{d}S - \frac{\sigma h}{2\pi} \ln\left(\frac{b_k}{a_k} \right) \Delta U_k,
\end{aligned}
\tag{3.2.18}
$$

where S_k is the surface of the coil's cross section, $\boldsymbol{n}_k = \boldsymbol{i}_\Theta$ is the normal to the cross-section, h is the height of the cross section, b_k is the outside radius of the cross section, and a_k is the inside radius of the cross section. This equation may be solved for ΔU_k in terms of $I(t)$ and $\dot{A}_\Theta$, and using equations (3.1.57), (3.2.10), and (3.2.17) the hoop component electric current density in coil turn k is given by

$$
J_\Theta = \frac{\sigma}{hR} \left(\ln\frac{b_k}{a_k} \right)^{-1} \left(\frac{I(t)}{\sigma} + \int_{S_k} \dot{A}_\Theta \, \mathrm{d}S \right) - \sigma\dot{A}_\Theta.
\tag{3.2.19}
$$

This expression for the electric current density in the coil is substituted into the variational formulation, equation (3.2.1), to yield a boundary value problem dependent only on A_Θ. However, the integral in equation (3.2.19) is over the entire cross section of the coil turn, which introduces non-local relations into the subsequent finite element formulation.

3.3   Numerical Implementation

The numerical implementation of the general theory employs the variational integration approach. According to this method space and time interpolation schemes are concurrently applied to the Lagrangian, followed by the variational principle applied on the discrete nodal variables for each time step (Marsden and West, 2001; Sanyal et al., 2005).

In the axisymmetric cases discussed here, the independent variables, functions of R and Z, are: nonzero displacements u_R and u_Z and nonzero magnetic vector potential component A_Θ. All the independent variables are continuous functions of the space variables, as discussed in Section 3.2.2. Therefore, employing nodal finite elements one has the discretization in space, given by

$$A_e(R,Z;t) \approx M(R,Z) \bullet q_e(t)$$

$$u_e(R,Z;t) \approx N(R,Z) \bullet p_e(t), \tag{3.3.1}$$

where A_e is the vector potential A inside an element, u_e is the displacement u inside an element, M is the spatial interpolation matrix of element basis functions for A, N is the spatial interpolation matrix of element basis functions for u, q_e are the nodal degrees of freedom for A in the element, and p_e are the nodal degrees of freedom for u in the element. Four node bilinear quadrilateral elements are used to discretize the reference configuration, with the same mesh being employed for A and u. These linear elements are appropriate since the Lagrangian, equation (3.2.1), involves only up to first derivatives of A and u.

Using the backward Euler approximation for time discretization, one has

$$\dot{A}_e(R,Z;t_i) \approx M(R,Z) \bullet \dot{q}_e(t_i), \ \dot{q}_e(t_i) \approx \frac{q_e^i - q_e^{i-1}}{\Delta t}$$

$$\dot{u}_e(R,Z;t_i) \approx N(R,Z) \bullet \dot{p}_e(t_i), \ \dot{p}_e(t_i) \approx \frac{p_e^i - p_e^{i-1}}{\Delta t}, \tag{3.3.2}$$

where q_e^i and p_e^i are the degrees of freedom in an element at time t_i and $\Delta t \equiv t_i - t_{i-1}$.

With the above space and time discretization and using the trapezoidal rule for time

integration of $\mathscr{F}$, a discrete action $\mathscr{F}^d$ is defined by

$$
\begin{aligned}
\mathscr{F} &\equiv \int_{t_0}^{t_M} \mathscr{L}(\boldsymbol{A}, \boldsymbol{u}, \dot{\boldsymbol{u}}, t) \, \mathrm{d}t \\
&\approx \frac{\Delta t}{2} \mathscr{L}_0 + \Delta t \sum_{i=1}^{M-1} \mathscr{L}_i + \frac{\Delta t}{2} \mathscr{L}_M \\
&\approx \frac{\Delta t}{2} \mathscr{L}_0^d + \Delta t \sum_{i=1}^{M-1} \mathscr{L}_i^d + \frac{\Delta t}{2} \mathscr{L}_M^d \equiv \mathscr{F}^d,
\end{aligned}
\tag{3.3.3}
$$

where the Lagrangian is from equation (3.2.1) and approximated discretely by using equations (3.3.1) and (3.3.2),

$$
\begin{aligned}
\mathscr{L}_i &\equiv \mathscr{L}(\boldsymbol{A}(t_i), \boldsymbol{u}(t_i), \dot{\boldsymbol{u}}(t_i), t_i) \\
&\approx \mathscr{L}_i^d(\boldsymbol{q}^i, \boldsymbol{p}^i, \boldsymbol{p}^{i-1}, t_i).
\end{aligned}
\tag{3.3.4}
$$

The degrees of freedom at time t_i throughout the domain of integration in space are given by $\boldsymbol{q}^i$ and $\boldsymbol{p}^i$. Upon application of Hamilton's variational principle with respect to these discrete degrees of freedom, the discrete governing equations are

$$
\mathscr{F}_{,\boldsymbol{q}^i}^d \left[\delta \boldsymbol{q}^i\right] = 0, \ \mathscr{F}_{,\boldsymbol{p}^i}^d \left[\delta \boldsymbol{p}^i\right] = 0,
\tag{3.3.5}
$$

where $\delta \boldsymbol{q}^0 = \delta \boldsymbol{q}^M = \boldsymbol{0}$ and $\delta \boldsymbol{p}^0 = \delta \boldsymbol{p}^M = \boldsymbol{0}$. These equations provide the time stepping routine to solve for the degrees of freedom at each time step, that is given $[\boldsymbol{q}^i, \boldsymbol{q}^{i-1}, \boldsymbol{p}^i, \boldsymbol{p}^{i-1}]$ one calculates $[\boldsymbol{q}^{i+1}, \boldsymbol{p}^{i+1}]$. The choice of the approximations to the time derivatives and integral in equations (3.3.2) and (3.3.3), respectively, allows for the coupled problem to be solved efficiently. One may calculate $\boldsymbol{p}^{i+1}$ independent of $\boldsymbol{q}^{i+1}$, since there are no $\dot{\boldsymbol{A}}$ terms in $\mathscr{L}$ and thus no coupling terms between $\dot{\boldsymbol{A}}$ and $\dot{\boldsymbol{u}}$. Then $\boldsymbol{q}^{i+1}$ is given in terms of $\boldsymbol{q}^i$, $\boldsymbol{p}^i$, and $\boldsymbol{p}^{i+1}$, thus justifying a staggered solution algorithm for the fully coupled problem.

To complete the implementation the initial and boundary conditions are needed. The initial conditions are given by

$$
\boldsymbol{q}^0 = \boldsymbol{0}, \ \boldsymbol{p}^0 = \boldsymbol{0}.
\tag{3.3.6}
$$

Note that the problem is driven by the time dependent input electric current $I(t)$, as discussed in Section 3.2.2.2.

The problem also requires application of the essential boundary conditions. In addition to axisymmetry, the processes discussed subsequently will all have mirror symmetry around $Z = 0$. This implies the essential boundary conditions for A are

$$\{R = 0\} \Rightarrow \{A_\Theta = 0\}$$

$$\{R^2 + Z^2 \to \infty\} \Rightarrow \{A_\Theta \to 0\}. \tag{3.3.7}$$

$R = 0$ is the axis of rotational symmetry, implying $A_\Theta = 0$, and the electromagnetic fields decay to zero at infinity. For simplicity, the latter boundary condition is implemented by taking a large area of meshed air and applying $A_\Theta = 0$ at the edges. In the following calculations it has been confirmed that the size of the air mesh is large enough as to accurately model the infinity boundary condition. For u, one need impose only the boundary condition

$$\{Z = 0\} \Rightarrow \{u_Z = 0\}, \tag{3.3.8}$$

which is dictated by mirror symmetry.

Note that outside the workpiece the displacements are not determined by the variational procedure. The coil is stationary, and in the surrounding air the equation of motion is satisfied identically, as expected. However, it is necessary to assume a distribution of displacement in the air in order to ensure the mapping between reference and current configurations remains invertible. Moreover, this distribution affects the numerical solution and if not carefully chosen can cause the simulation to give poor results. In the present work, a simple distribution of displacements in the air is implemented that adjusts with the displacements in the workpiece as necessary.

It is also important to note the influence of the forming coil on the finite element ma-

trices. Equation (3.2.19) implies that each degree of freedom in a coil turn cross section is directly coupled to every other one, through the integral over the cross section. This introduces non-local relations into the finite element method, and the resulting stiffness matrices are no longer symmetric.

The numerical techniques detailed above are implemented using the finite element program FEAP[13]. Moreover, the choice of the numerical integration techniques will be discussed further in a subsequent publication. Details of the solution algorithm will be given there, along with an analysis of the technique and possible alternatives.

3.4 Results

One can now turn to simulations of electromagnetic forming processes, and the numerical simulation is employed to model two types of processes. First is that of ring expansion, compared with the semi-analytical solution of Triantafyllidis and Waldenmyer (2004) that uses known integration forms and inductance formulas. The ring expansion test problem provides a check on the accuracy of the simulation.

Second is the process of tube expansion, inspired by the experiments of Section 2.3. Figure 2.13a shows a bare four turn coil from the experiments, and Figure 2.13b shows that same coil, potted in epoxy, with a tube fitted around the coil before deformation. Figures 1.3 and 2.14 show examples of deformed tubes from such experiments. Accounting for axisymmetry and mirror symmetry, along the $Z = 0$ plane, as discussed in Section 3.3, an FEM mesh for tube expansion is shown in Figure 3.1, including a close-up view of the coil and tube. The coil and tube are denoted in grey and the air is the meshed area in white.

---

[13]Finite Element Analysis Program http://www.ce.berkeley.edu/~rlt/feap/
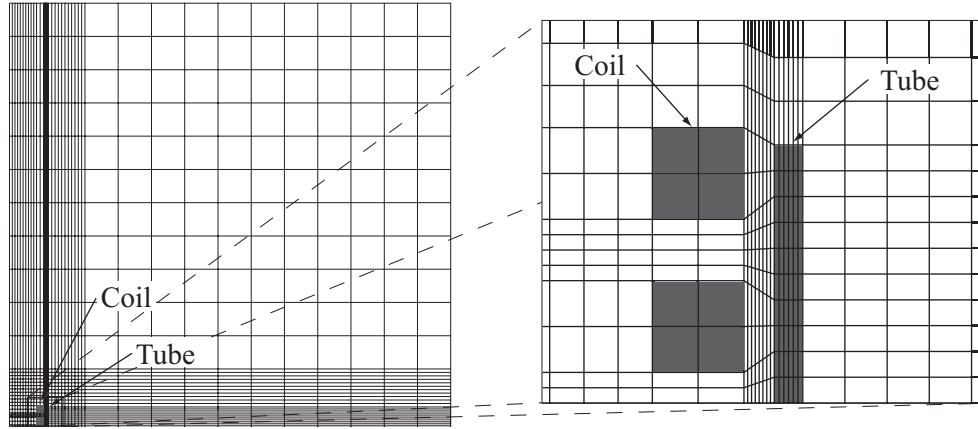
Figure 3.1: Example FEM mesh for axisymmetric tube expansion.

In the following simulations, a cylindrical four turn coil expands three tubes of varying height: one taller than the coil, one of approximately even height with the coil, and one shorter than the coil. The first two are based directly on the geometry of the experimental tubes (Section 2.3) while the third is chosen as a representative process with a tube shorter than the forming coil. Finally, motivated by Zhang et al. (2008) the expansion of the tall tube with a non-conductive coating applied to the outside is addressed, which to the best of the author's knowledge is the first simulation of this problem in the literature.

The basic dimensions of the axisymmetric ring and tube expansion problems are shown in Figure 3.2, where the origin O is at the intersection of the axisymmetry axis, i.e. the Z-axis, and the plane of mirror symmetry, i.e. the $Z = 0$ plane. The midlines of the coil turns and workpiece are denoted with solid dots, and the midplane of the workpiece is denoted with a dashed line. The relevant dimensions are: radius of the coil midlines, R_c; radius of workpiece midline, R_w; pitch of the coil, P_c; height of the workpiece, Z_w; coil turn cross section thickness, T_c; and workpiece cross section thickness, T_w, where for a ring $Z_w = T_w/2$.

In the subsequent simulations, unless otherwise noted, the overall finite element mesh is chosen to give a result corresponding to the converged solution, based on simulation
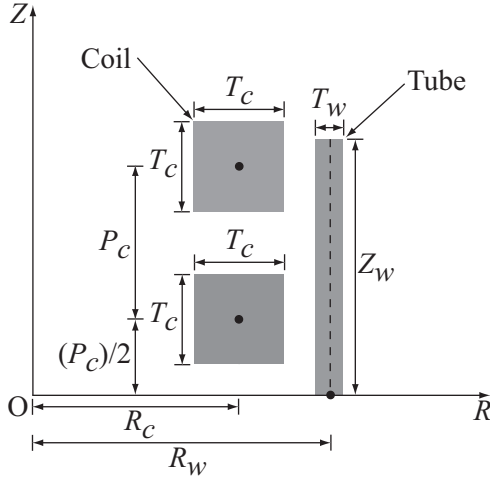
Figure 3.2: Dimensions of ring and tube expansion problems.

runs with varying meshes and time steps. An example of the relative mesh density is shown in Figure 3.1, where the area in and near the workpiece and coil are meshed more finely than the air farther away. The space between the coil and workpiece is meshed very finely to provide adequate mesh density as the workpiece expands, and the convergence study established the adequacy of a relatively coarse mesh of four elements in each square coil turn, which is used throughout the following work and simplifies the implementation (see the discussion of non-local coupling between coil elements in Section 3.3).

Furthermore, there are two regions of air mesh: one with displacements (necessary near the workpiece, see Section 3.3) and one stationary. The region of air with non-zero displacements is the air with radius greater than the outside radius of the coil, up to a distance R^d_{mesh} in the R direction from the outside of the workpiece and up to a distance Z^d_{mesh} in the Z direction from the top of the coil or workpiece, whichever is taller. The air mesh without displacements extends beyond this distances of R_{mesh} and Z_{mesh} in the R and Z directions, respectively. In all cases, the extension of the air mesh is chosen relative to the inner radius of the workpiece, i.e. $R^{\mathrm{in}}_w = R_w - T_w/2$. In the first test problem of the ring expansion, $R^d_{\mathrm{mesh}} = Z^d_{\mathrm{mesh}} = 2R^{\mathrm{in}}_w$ and $R_{\mathrm{mesh}} = Z_{\mathrm{mesh}} = 10R^{\mathrm{in}}_w$. The second

ring expansion test problem modifies this to $R^d_{\text{mesh}} = Z^d_{\text{mesh}} = R^{\text{in}}_w$ and shows no loss of accuracy. Therefore, the subsequent tube expansion simulations use $R^d_{\text{mesh}} = Z^d_{\text{mesh}} = R^{\text{in}}_w$ and $R_{\text{mesh}} = Z_{\text{mesh}} = 10R^{\text{in}}_w$.

The time step Δt is chosen for convergence, which is verified using the ring expansion simulations, and is set to $\Delta t = 10^{-8}$ s. In general decreasing the time step below that required for stability showed negligible change in the solution. The choice of mesh and time step will be explored in detail in a subsequent publication.

In addition, the input electric current is necessary. Since in typical EMF processes the electric current in the forming coil is very close to an exponentially decaying sinusoid (see for example Figure 2.16a), the general form taken in the present work is

$$I(t) = I_{\text{max}} \sin\left(\frac{\pi t}{2t_0}\right) \exp\left(\ln(k)\left(\frac{t}{2t_0}\right) - \frac{\ln(k)}{2}\right), \tag{3.4.1}$$

where t_0 is the characteristic time of the current pulse, I_{max} is the electric current at $t = t_0$, and k is a decay parameter, $k = I(3t_0)/I_{\text{max}}$. This general form is fit to the individual forming processes.

3.4.1 Material Constitutive Behavior

For this first implementation of the general theory, temperature effects are ignored, so the thermal dependence of the constitutive behavior is unnecessary. The electromagnetic and mechanical material response are discussed subsequently.

3.4.1.1 Electromagnetic Constitutive Response

Since the applications of interest involve metals under high current density, magnetization and polarization can be safely ignored, and equation (3.1.25) gives the constitutive relations between the electric field and electric displacement and between the magnetic field and H field. Only Ohm's law is required to relate electric current with electric field,

and Ohm's law with constant conductivity is given in equation (3.2.10). See Table 3.1 for the values of the electromagnetic constitutive parameters, which are the same throughout the following simulations. These values are chosen because copper is a typical actuator material and in the experiments of Section 2.3 the tubes were made of AA6063-T6 aluminum alloy. The parameters μ_0 and ϵ_0 are the permeability and permittivity of vacuum, respectively, and these values along with those of the resistivity of aluminum, r_{Al}, and copper, r_{Cu}, are available in standard references. Also, note that the coatings applied to the tall tube are assumed to have zero conductivity.

$\mu_0 = 1.26 \ 10^{-6}$ N/A^2	$\epsilon_0 = 8.85 \ 10^{-12}$ F/m	$r_{Al} = 2.65 \ 10^{-8}$ Ωm	$r_{Cu} = 1.68 \ 10^{-8}$ Ωm

Table 3.1: Electromagnetic constitutive parameter values

3.4.1.2 Mechanical Constitutive Response

As a first implementation, the mechanical constitutive response of each material can be approximated by a hyperelastic strain energy function. Two mechanical constitutive laws are employed. One is a formulation based on J$_2$ deformation theory of plasticity (see Abeyaratne and Triantafyllidis (1981) and references cited therein). For metals undergoing moderate deformations with nearly proportional loading and neglecting rate effects, J$_2$ deformation theory of plasticity can be used for initially isotropic materials (Anand, 1979). Moreover, this formulation can be fit to any uniaxial strain hardening response. Because of this, it is also a good constitutive law to model the first coating of interest, polyurea, which is assumed isotropic with no rate effects. In general however, rate effects are more important in polyurea than the metals of interest, and future work should consider the rate dependence of the polyurea constitutive response. The second mechanical constitutive law is a compressible Mooney-Rivlin formulation (Hallquist, 2006) that is

implemented to model a potential alternative coating on the tall tube. The Mooney-Rivlin material is also used in the ring expansion simulations.

The hyperelastic strain energy density function is defined by

$$W(\lambda_1, \lambda_2, \lambda_3) \equiv \rho_0 \psi, \tag{3.4.2}$$

where λ_1, λ_2, and λ_3 are the principal stretch ratios. In the case of a strain hardening material it is assumed the mechanical response is governed under loading by

$$\frac{\epsilon_e}{\epsilon_y} = \frac{\tau_e}{\tau_y} \text{ for } \tau_e \leqslant \tau_y, \quad \frac{\epsilon_e}{\epsilon_y} = \left(\frac{\tau_e}{\tau_y}\right)^m \text{ for } \tau_e > \tau_y, \tag{3.4.3}$$

where ϵ_e is the equivalent logarithmic strain, ϵ_y is the yield logarithmic strain, τ_e is the equivalent Krichoff stress , τ_y is the Kirchoff yield stress, and m is the hardening exponent. The Kirchoff stress tensor τ is related to the Cauchy stress tensor σ by $\tau = J\sigma$, and the yield logarithmic strain ϵ_y is related to the Krichoff yield stress τ_y by $\epsilon_y = \tau_y/E$, where E is Young's modulus. The strain energy density function based on J_2 deformation theory of plasticity that models this strain hardening under loading is given by

$$W = E\epsilon_y^2 \left[\frac{\chi}{\chi+1} \left(\frac{\tau_e}{\tau_y}\right)^{\chi+1} - \frac{1-2\nu}{6}\left(\frac{\tau_e}{\tau_y}\right)^2 \right] + \frac{E}{6(1-2\nu)}(\epsilon_1 + \epsilon_2 + \epsilon_3)^2 + C, \tag{3.4.4}$$

where ν is Poisson's ratio and C is a constant, and τ_e is related to ϵ_e by

$$\frac{\epsilon_e}{\epsilon_y} = \left(\frac{\tau_e}{\tau_y}\right)^\chi - \frac{1-2\nu}{3}\left(\frac{\tau_e}{\tau_y}\right), \quad \chi = \begin{cases} 1 & \text{for } \epsilon_e \leqslant \dfrac{2(1+\nu)}{3}\epsilon_y \\[2mm] m & \text{for } \epsilon_e > \dfrac{2(1+\nu)}{3}\epsilon_y. \end{cases} \tag{3.4.5}$$

The consant C is constructed to assure the continuity of W at $\epsilon_e = \frac{2(1+\nu)}{3}\epsilon_y$. Also, the equivalent logarithmic strain ϵ_e is given by

$$\epsilon_e = \frac{2}{3}(\epsilon_1^2 + \epsilon_2^2 + \epsilon_3^2 - \epsilon_1\epsilon_2 - \epsilon_2\epsilon_3 - \epsilon_3\epsilon_1)^{1/2}, \tag{3.4.6}$$

where $\epsilon_i = \ln(\lambda_i)$.
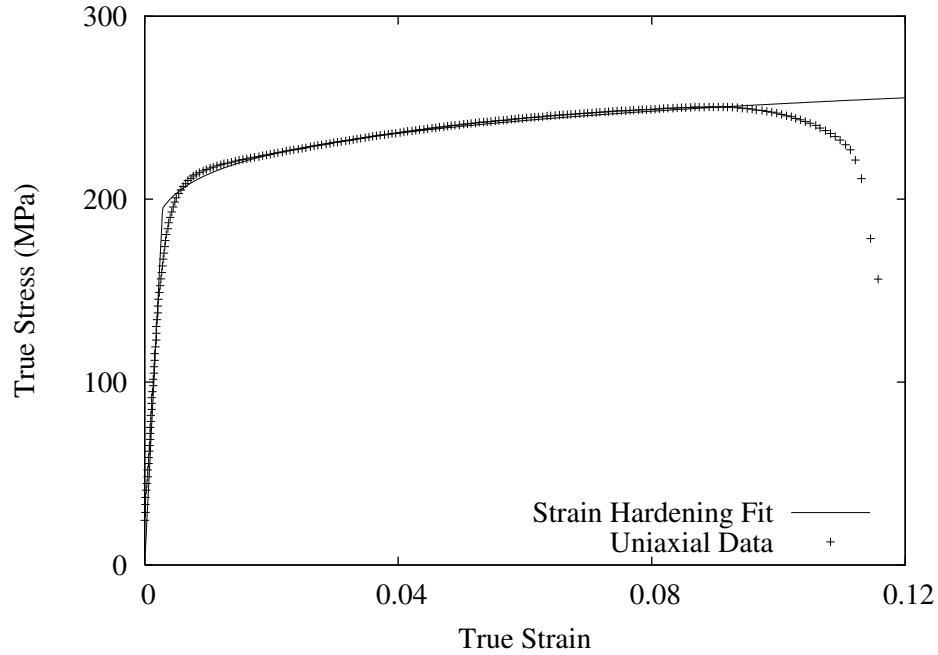
Figure 3.3: Comparison of uniaxial data and strain hardening constitutive response for AA6063-T6.

The strain hardening law in equation (3.4.5) is matched to the quasistatic uniaxial data in Section 2.3 for the tube alloy used in the experiments, AA6063-T6. This gives Young's modulus, the Kirchoff yield stress, and the hardening exponent, and a comparison of the strain hardening curve and uniaxial data is given in Figure 3.3. Poisson's ratio is then chosen to give a nearly incompressible material (an accurate assumption for metals at large plastic strains) while not producing numerical difficulties related to incompressibility, and the mass density, ρ, is obtained from standard references on Aluminum (it is not alloy sensitive). The resulting parameter values are given in Table 3.2.

$E = 69\ 10^9$ Pa	$\tau_y = 195\ 10^6$ Pa	$m = 1/0.072$	$\nu = 0.45$	$\rho = 2700$ kg/m^3

Table 3.2: AA6063-T6 uniaxial mechanical constitutive parameter values

In addition, uniaxial compression data for polyurea (see the sprayed polyurea material from Chakkarapani et al. (2006), and the behavior in tension is assumed to be

similar to that in compression) is used to determine its strain hardening behavior. The resulting Young's modulus, Kirchoff yield stress, and hardening exponent are given in Table 3.3, along with Poisson's ratio (chosen as for AA6063-T6) and the mass density of the polyurea coating, obtained from Zhang and Ravi-Chandar (2008).

| $E = 0.25 \ 10^9$ Pa | $\tau_y = 8.7 \ 10^6$ Pa | $m = 1/0.12$ | $\nu = 0.45$ | $\rho = 1200 \ \text{kg/m}^3$ |

Table 3.3: Polyurea uniaxial mechanical constitutive parameter values

To investigate alternative coatings for the tall tube and as a simple material model for the ring expansion simulations, a compressible Mooney-Rivlin material response is implemented. The strain energy density function is given by

$$W(\lambda_1, \lambda_2, \lambda_3) = A(I_1 - 3) + B(I_2 - 3) + C(I_3^{-2} - 1) + D(I_3 - 1)^2, \qquad (3.4.7)$$

where I_1, I_2, and I_3 are the strain invariants and A, B, C, and D are material constants given by

$$A = \frac{E}{8(1 + \nu)}$$

$$B = A$$

$$C = \frac{1}{2}A + B \qquad (3.4.8)$$

$$D = \frac{A(5\nu - 2) + B(11\nu - 5)}{2(1 - 2\nu)}.$$

E and ν for the Mooney-Rivlin coating are assumed to be the same as for the strain hardening polyurea and are given in Table 3.3. A comparison of the uniaxial data, strain hardening curve, and Mooney-Rivlin curve is given in Figures 3.4a and 3.4b, where Figure 3.4b is a close-up picture of the uniaxial data.

For the ring expansion simulations, the compressible Mooney-Rivlin response parameters are taken as in Table 3.4. These values are carried over from aluminum, with the
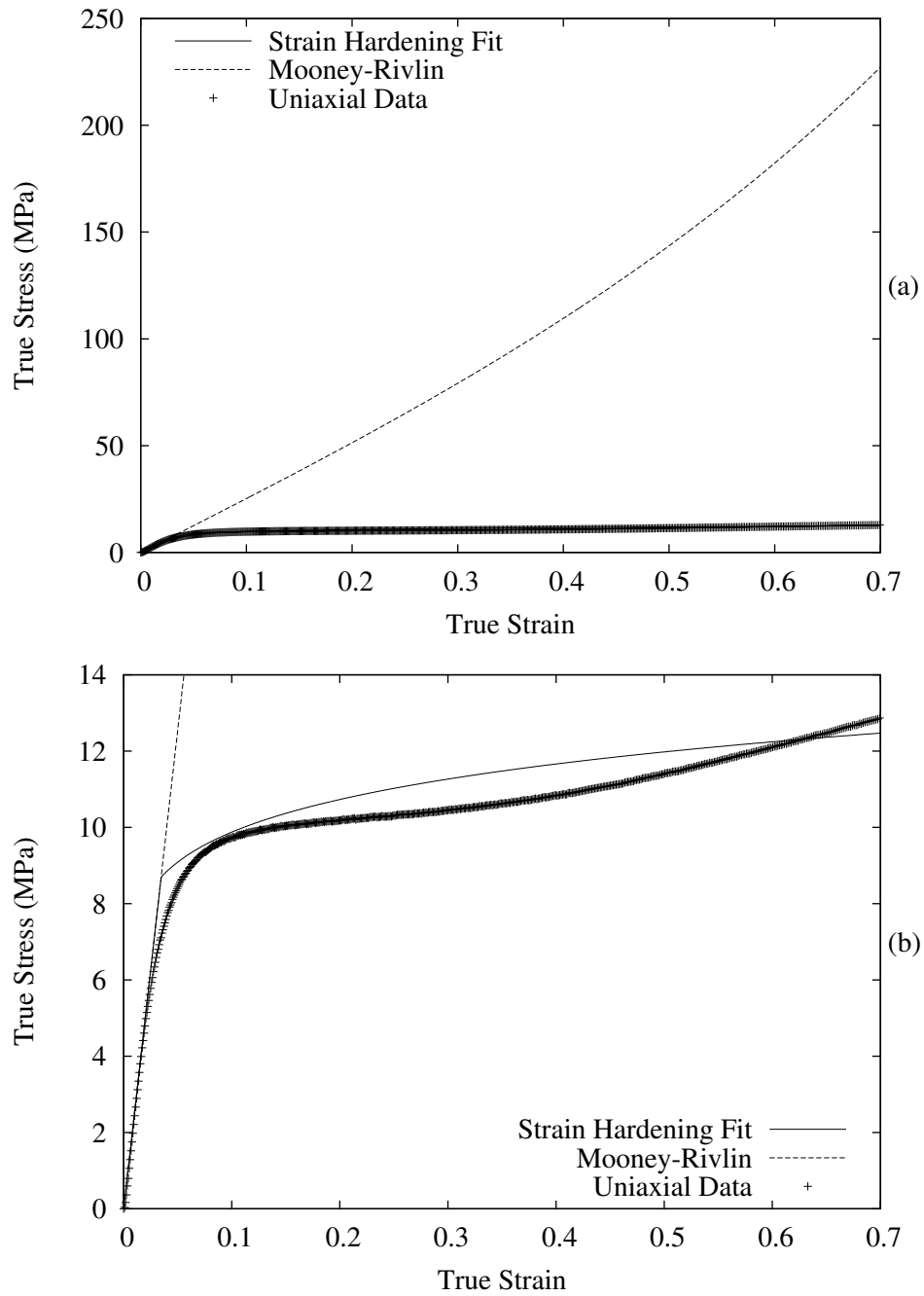
Figure 3.4: Mechanical constitutive response of coatings. a) Comparison of uniaxial polyurea data with strain hardening and Mooney-Rivlin constitutive responses. b) Close-up view of uniaxial polyurea data and strain hardening response.

exception that E is chosen to give strains similar to those that would result from strain hardening AA6063-T6 aluminum.

$$E = 1.725 \ 10^9 \ \text{Pa} \quad \nu = 0.45 \quad \rho = 2700 \ \text{kg/m}^3$$

Table 3.4: Ring expansion mechanical constitutive parameter values

With the material constitutive response detailed the numerical implementation is complete. One may now move to simulations of electromagnetic forming processes.

3.4.2 Comparison with 1-D Ring Expansion

A check on the accuracy of the simulation is obtained from the results for a thin ring being expanded by a four turn coil with small cross section turns. The FEM results here are compared with results from the 1-D semi-analytical technique in Triantafyllidis and Waldenmyer (2004), modified to accept an input coil current and the compressible Mooney-Rivlin material of Section 3.4.1.2. The Mooney-Rivlin material is chosen for the test ring expansion problems due to its simple formulation and implementation.

The geometry of the ring expansion process is chosen such that the filament assumptions inherent in Triantafyllidis and Waldenmyer (2004) are accurate, and thus the ratio of cross section size to separation distance is kept at 0.1 or less. A test problem is set up that is inspired by the results in Triantafyllidis and Waldenmyer (2004) but uses a four turn coil similar to that in the tube expansion experiments of Section 2.3. The dimensions of the problem are given in Table 3.5 under Test Problem 1. The coil turns and the ring have square cross sections, and the ring is fitted on the coil symmetrically around $Z = 0$.

In addition, the input electric current parameters in equation 3.4.1 are chosen such that for the Mooney-Rivlin material discussed above the strains are on the order of those in Section 2.3 and such that the electric current decays by half at the second pulse. These values are given in Table 3.6. The magnitude of the resulting electric current is about

	Test Problem 1	Test Problem 2
R_c	0.02205 m	0.02205 m
R_w	0.03195 m	0.03195 m
P_c	0.0099 m	0.0099 m
Z_w	0.00045 m	0.000225 m
T_c	0.0009 m	0.00045 m
T_w	0.0009 m	0.00045 m

Table 3.5: Geometry of ring expansion test problems

twice that calculated in Triantafyllidis and Waldenmyer (2004) while the characteristic time closely matches those ring results.

	Test Problem 1	Test Problem 2
I_{max}	$60 \ 10^3$ A	$60 \ 10^3$ A
t_0	$12.6 \ 10^{-6}$ s	$12.6 \ 10^{-6}$ s
k	0.5	0.5

Table 3.6: Ring expansion applied electric current parameters

Results of this simulation are plotted in Figure 3.5, where the nondimensional radial position of the ring midline is plotted against nondimensional time. The 1-D solution uses the 1-D analysis of Triantafyllidis and Waldenmyer (2004), and the FEM solutions are from the 2-D FEM simulation introduced in this work. The coil impact radius is the radius of the ring midline at which the inner radius of the ring is equal to the outer radius of the coil. Since there is no interest in modeling impact, the simulation is terminated just before this event.

In Figure 3.5 the FEM solution begins with 36 elements in the ring and with increasing mesh density shows convergence of the solution to a result with a slightly greater maximum deformation than that of the 1-D solution. Though they are close, the difference in the results is intriguing. Because Triantafyllidis and Waldenmyer (2004) calculate mutual inductances on the assumption of interacting filaments, the results can be expected
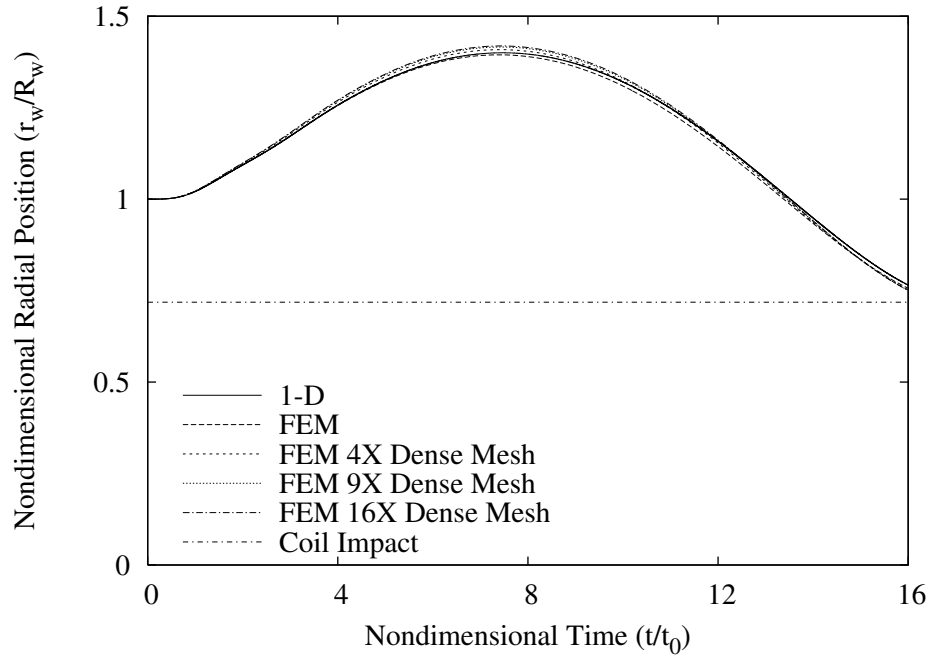
Figure 3.5: Midline radial position of ring expanded by four turn coil.

to differ for problems with significant cross section size relative to separation distance. As discussed, the first test problem here has a small cross section to separation distance ratio, but this ratio may still influence the result.

To test the influence of the cross section size, a second test problem is set up with smaller cross section coil turns and ring, where all the other dimensions are the same as in the first test problem. The geometry of this problem is given in Table 3.5 under Test Problem 2. The coil turns and the ring have square cross sections with one quarter the area of those in the first test problem. The results of this simulation are shown in Figure 3.6, where again the nondimensional ring midline radial position is plotted against nondimensional time. The reference mesh has 16 elements in the ring but is much denser in the air than the reference mesh in the first test problem. The denser mesh of the second test problem has nine elements for every four in the reference mesh. Compared to the first test problem, the displacements are larger but the 1-D and FEM results are closer together, and there is only a small change between meshes indicating the dense mesh is
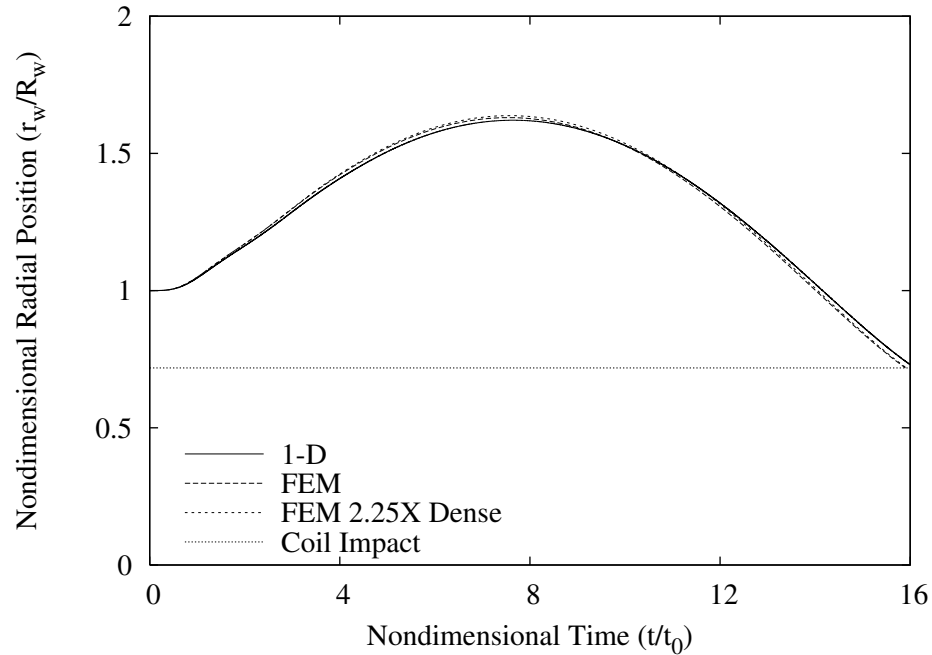
Figure 3.6: Midline radial position of ring expanded by four turn coil: Smaller cross sections.

close to the converged solution.

The maximum discrepancy between the 1-D and the densest mesh FEM results for the first ring expansion case is 4.9% of the maximum deformation, and it occurs near the point of maximum deformation. The second ring expansion case has a maximum discrepancy between the 1-D and the densest mesh FEM results of 3.5% of the maximum deformation, but this occurs near $t/t_0 = 16$. The maximum discrepancy for the portion of the results with positive displacement is 3.1%. This shows that for the geometry here the cross section size has a small effect on the difference between the two simulations.

The electric current for the second test case for the 1-D and densest mesh FEM results is plotted in Figure 3.7. This provides another check on the accuracy of the solution. The input coil electric current is the same in each solution, and the induced ring electric currents are plotted as dashed curves. The results show very good agreement, with the discrepancy less than 2% of the maximum induced current making the dashed lines
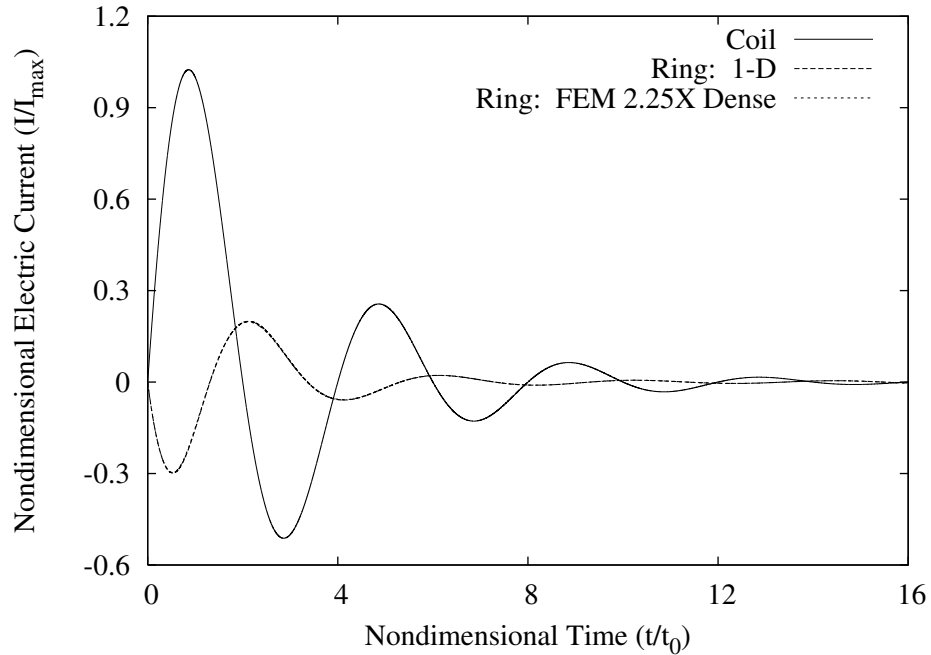
Figure 3.7: Electric currents in four turn coil and expanding ring: Smaller cross sections.

indistinguishable in the figure.

Figures 3.5, 3.6, and 3.7 show close agreement between the FEM formulation discussed here and the 1-D formulation of Triantafyllidis and Waldenmyer (2004). This indicates the FEM simulation correctly solves the coupled electromagnetic-mechanical problem of ring expansion, and thus the following section turns to tube expansion processes.

3.4.3 Tube Expansion

For the tube expansion simulations, the geometry is matched as closely as possible to that of the experiments in Section 2.3. The geometry of the four cases is given in Table 3.7, where only the tube height varies between simulations. A minor change from the experiments is the substitution of square cross section coil turns for the circular cross section turns, thus avoiding meshing difficulty for the coil. Each coil turn has a square cross section with the same area as the circular ones in the experiments, and the tubes are

placed on the coil symmetrically around $Z = 0$. Also, the height of the short tube is taken as two thirds that of the even tube (as previously noted, the height of the short tube is not directly based on an experiment), and the coated tube is simply the tall tube with coating applied to the outside surface.

	Tall Tube	Even Tube	Short Tube	Coated Tall Tube
R_c	0.023825 m	0.023825 m	0.023825 m	0.023825 m
R_w	0.029375 m	0.029375 m	0.029375 m	0.029375 m
P_c	0.0094 m	0.0094 m	0.0094 m	0.0094 m
Z_w	0.085 m	0.0317 m	0.02113 m	0.085 m
T_c	0.0056275 m	0.0056275 m	0.0056275 m	0.0056275 m
T_w	0.00175 m	0.00175 m	0.00175 m	0.00175 m

Table 3.7: Geometry of tube expansion processes

In the first two tube expansion simulations, that of a tube taller than the coil and a tube even with the coil, the driving input electric current in the coil is measured from the corresponding experiments in Section 2.3. The short tube process uses the same input electric current as the even tube, and the same input electric current is applied to the coated tubes as to the uncoated tall tube. The analytical form of input electric current in equation (3.4.1) is matched to the measured electric current, and the resulting parameter values are given in Table 3.8.

	Tall Tube	Even Tube	Short Tube	Coated Tall Tube
I_{max}	137 10^3 A	130 10^3 A	130 10^3 A	137 10^3 A
t_0	17 10^{-6} s	26.6 10^{-6} s	26.6 10^{-6} s	17 10^{-6} s
k	0.3	0.3	0.3	0.3

Table 3.8: Tube expansion applied electric current parameters

3.4.3.1 Expanded Tubes without Coating

The first tube expansion process is that of a tube taller than the forming coil. Expanding the tube until just before significant unloading occurs results in the deformed tube
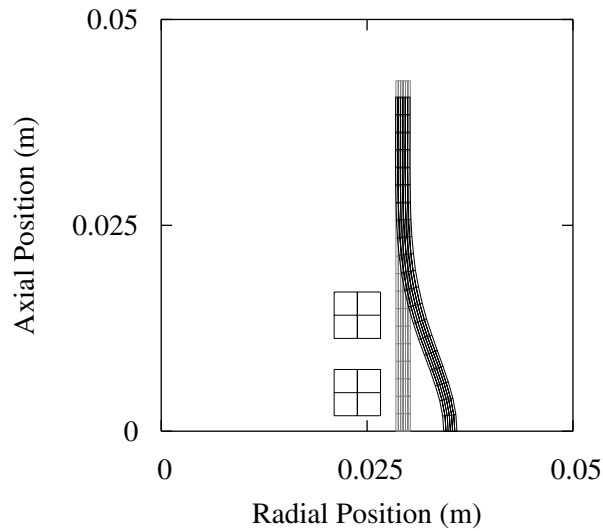
Figure 3.8: Deformed configuration at maximum midline displacement of tall tube deformed by four turn coil: $t/t_0 = 3.9$

in Figure 3.8, where light grey denotes the undeformed tube and black denotes the coil and deformed tube. Comparing the final deformed shape of the simulated tube with that in the corresponding experiment of Section 2.3 (allowing for necking and failure) shows that the deformed configuration is captured reasonably well.

There are two major differences between the experiments of Section 2.3 and the simulations here. First is the presence of necking and failure in the experimentally expanded tubes. The major strain in every case is in the hoop, i.e. Θ, direction. Thus for necking and/or failure to occur axisymmetry must be broken, which is not incorporated into the model here. However, the goal of the experiments was to deform the tubes up to the onset of necking or failure and no further. Therefore, the deformations in the simulations and in the experiments are expected to be reasonably similar, as the tall tube expansion demonstrates.

The second major difference is the hyperelastic formulation that causes the material

to return to its reference configuration during unloading, which is not the case with the plastic deformation in the experiments. To mitigate this difference one looks at the deformed tubes before unloading. For the first two tubes simulated (i.e. those taller than and even with the coil height) the final deformed configuration before significant unloading corresponds with the first maximum of the displacement of the tube midline. However, the third tube (i.e. the one shorter than the coil) shows dramatic shape changes in the tube before this maximum, which will be addressed subsequently.

A closer look at the deformation of the tall tube with respect to time is given in Figure 3.9 where the nondimensional radius of the tube midline is plotted with respect to nondimensional time. The first pulse of the electric current causes a pulse in the displacment up to $t/t_0 = 3.9$, at which point the nondimensional radius peaks, and this is when the deformed tube shape in Figure 3.8 is plotted. Moreover, the input coil and induced tube electric currents are shown, plotted with the nondimensional radius to show the relative timing. These results agree with the discussion in Section 2.3 of the timing of strain and electric current history. However, since a hyperelastic material is implemented the tube attempts to contract after loading, and the plateau of midline radius from $t/t_0 = 4$ to $t/t_0 = 7$ is a result of the contraction of other parts of the tube. The simulation is terminated before coil impact.

An examination of the electric current density in the deforming tube is given in Figures 3.10, 3.11, and 3.12. These figures are the electric current density at three relevant times showing the initial current and subsequent current reversal. Note that the scales on the x-axis and y-axis have been adjusted to show the electric current density more clearly, which has the effect of distorting the tube shape and deformation.

In Figure 3.10 the electric current density at $t/t_0 = 0.5$ is plotted, which is approximately halfway through the initial coil electric current pulse. As expected, the electric
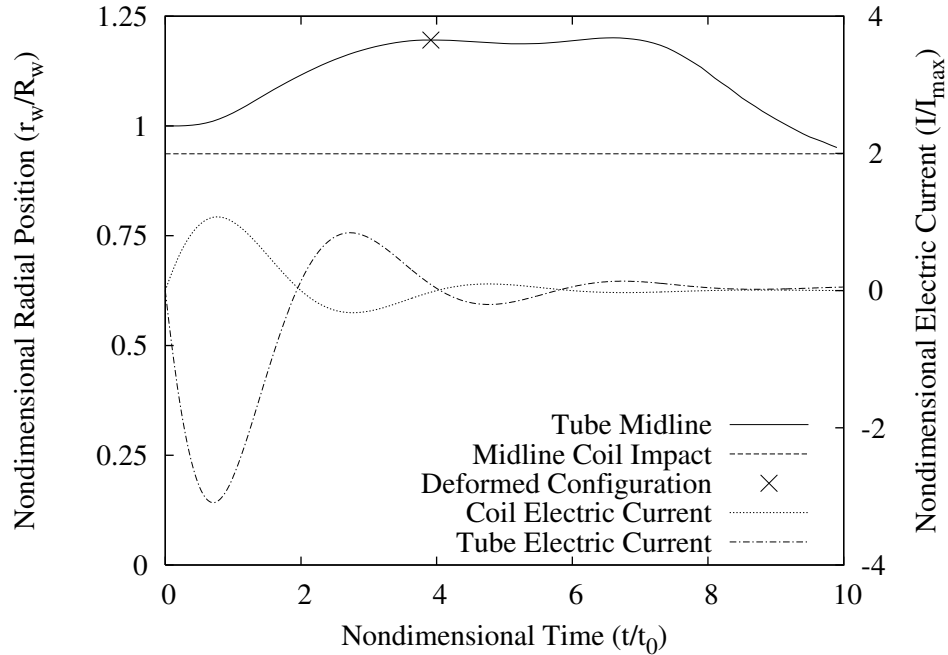
Figure 3.9: Midline radial position and electric currents of tall tube deformed by four turn coil.

current is concentrated on the inside surface of the tube, near the coil. Note that the electric current density here is negative because the initial coil electric current is positive.

Figure 3.11 shows the electric current density at $t/t_0 = 1.25$, just after the peak of the first pulse of coil electric current. The peak electric current density has moved from the inside surface to the middle of the tube and has dissipated in maximum intensity, indicated by the scale.

In Figure 3.12 the tall tube electric current density is shown at $t/t_0 = 2$, when the coil electric current is equal to zero. The electric current density in the tube has already reversed from what it was initially, with Figure 3.12 almost an inverse image of Figure 3.10 (allowing for deformation). Note, however, that the maximum current density is significantly less as the coil electric current decays and the separation between coil and tube increases.
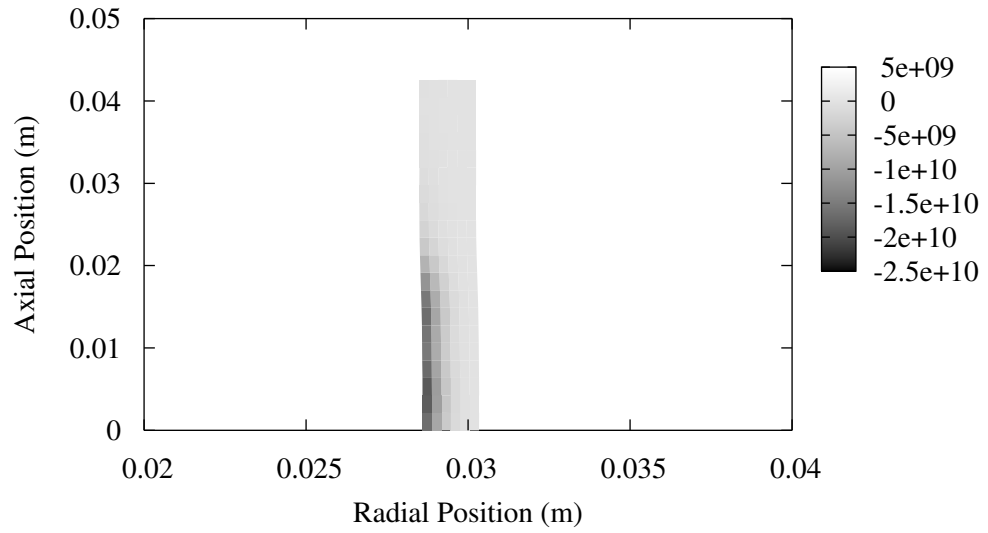
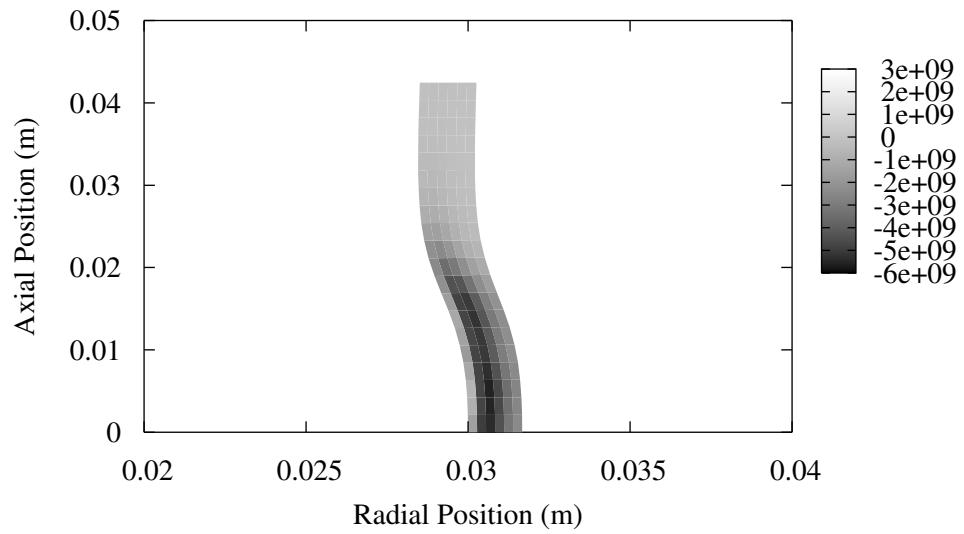Figure 3.10: Electric current density (A/m^2) distribution in the cross section of tall tube: $t/t_0 = 0.5$

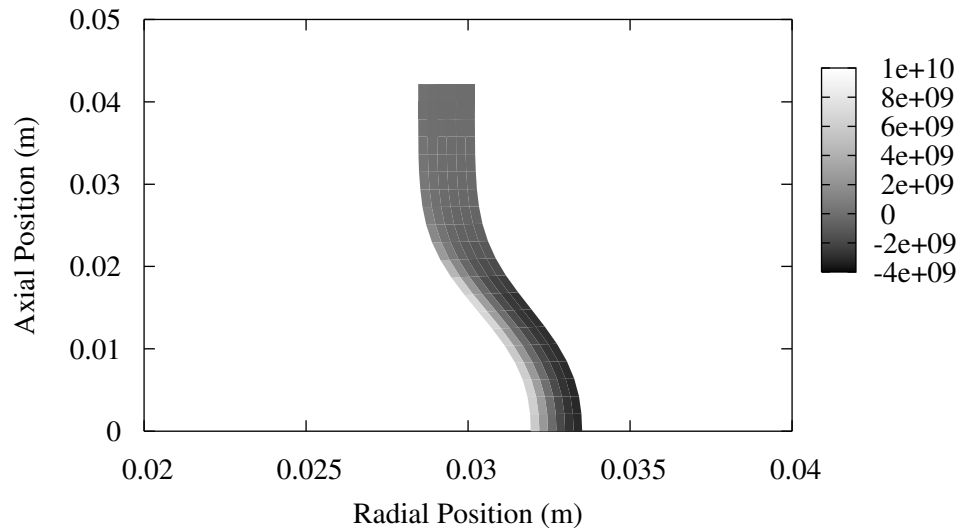Figure 3.11: Electric current density (A/m^2) distribution in the cross section of tall tube: $t/t_0 = 1.25$

Figure 3.12: Electric current density (A/m^2) distribution in the cross section of tall tube: $t/t_0 = 2$

The second tube expansion process is that of a tube approximately the same height as the forming coil. Expansion until significant unloading starts to occur results in the deformed configuration shown in Figure 3.13, where light grey denotes the undeformed configuration and black the deformed shape. Again, in Figure 3.14 the tube midline radial position versus time is plotted along with the electric current versus time for the coil and tube. The time at which the deformed configuration of Figure 3.13 occurs is denoted, which corresponds with the maximum midline displacement. This simulation also shows good qualitative agreement with the corresponding experimentally expanded tube.

The third tube expansion process is that of a tube shorter than the forming coil expanded using the same electric current input as for the tube of even height with the coil. In this process unloading significantly changes the character of the deformed configuration, so there is not a close relationship between max deformation and the configuration before significant unloading occurs, the latter of which corresponds to the experimental results.
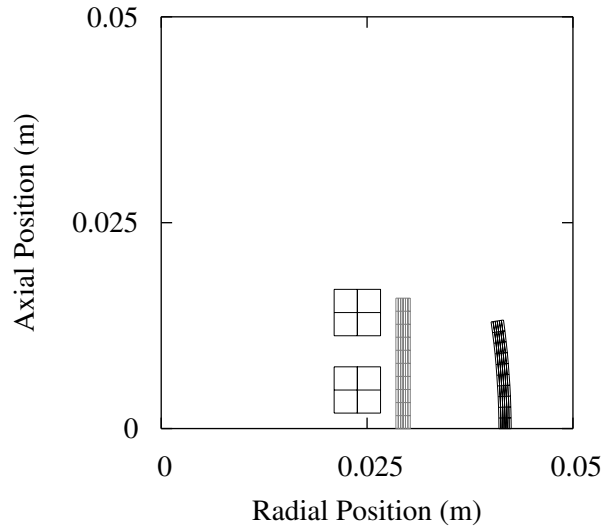
Figure 3.13: Deformed configuration at maximum midline displacement of tube deformed by four turn coil of equal height: $t/t_0 = 5$
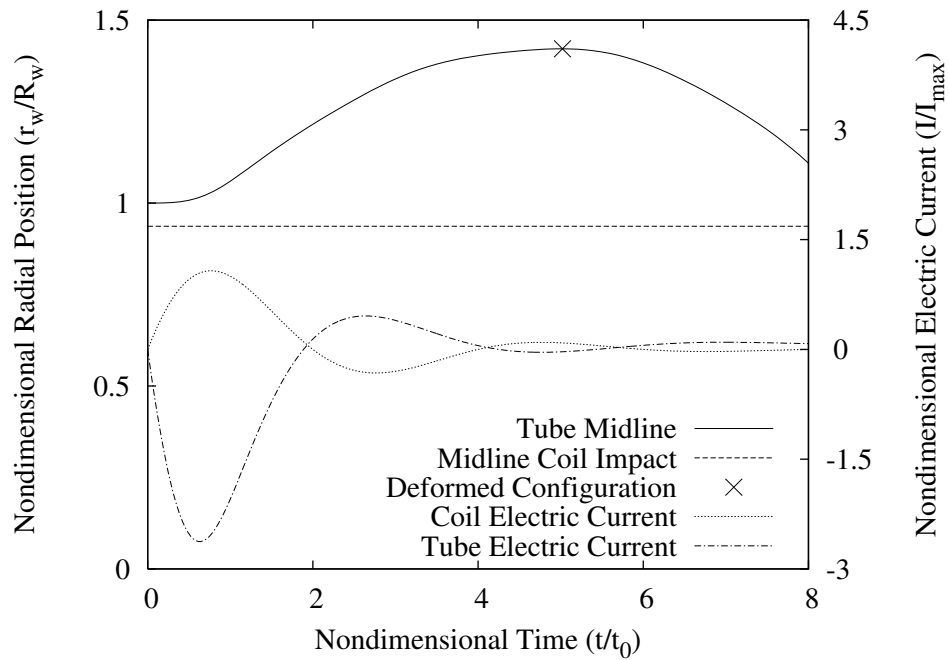

Figure 3.14: Midline radial position and electric currents of tube deformed by four turn coil of equal height.
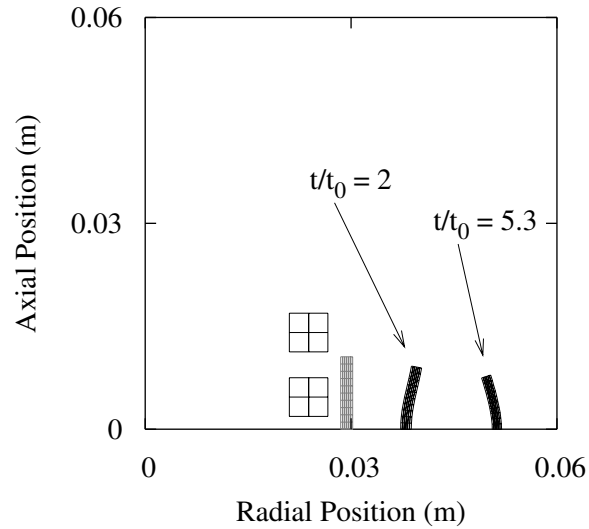
Figure 3.15: Deformed configurations of short tube deformed by four turn coil.

Therefore Figure 3.15 shows two deformed configurations. The first, at $t/t_0 = 2$, occurs before significant unloading and qualitatively matches with the experimentally obtained toroidal shape in the case where the tube is shorter than the coil. The configuration at $t/t_0 = 5.3$ corresponds with the maximum midline displacement and has a significantly different shape than that at $t/t_0 = 2$. The corresponding points on the midline radial position versus time curve are denoted in Figure 3.16, where the radial position and electric current are given together. The exact geometry of the simulation does not match that in the experiments, but the relationship between tube and coil is similar and thus the character of the results agrees.

The three tube expansion processes discussed above are in qualitative agreement with experimental results. This indicates the simulation correctly models the electromagnetic-mechanical interactions, and the next section discusses the solution of the problem of an electromagnetically expanded tube with a nonconducting coating applied to the outside.
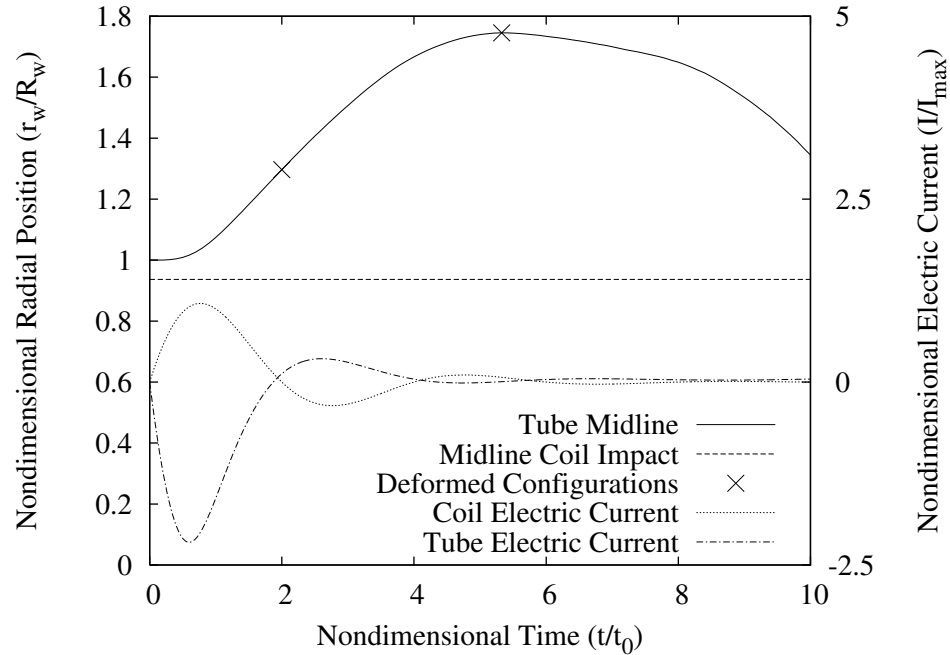
Figure 3.16: Midline radial position and electric currents of short tube deformed by four turn coil.

3.4.3.2 Expanded Tubes with Coating

Recent work by Zhang et al. (2008) examines the effect of a polymer coating applied to the outside surface of an electromagnetically expanded ring or tube. Therefore, the present work now turns to the electromagnetic expansion of the tall tube with a coating applied to the outside, a novel EMF simulation problem that is easily handled by the general theory presented here. An example FEM mesh of such a problem is given in Figure 3.17. As before the coil and tube are shown in grey and the air in white, and the coating, which is twice the thickness of the tube, is shown in light grey. Coatings of varying thickness are simulated, and the coating is modeled as either strain hardening polyurea or a material that follows the Mooney-Rivlin type response discussed previously.

As an example of the effect, in Figure 3.18 the midplane of the tube (excluding coating) is plotted for the case of no coating and of a polyurea coating twice the thickness of
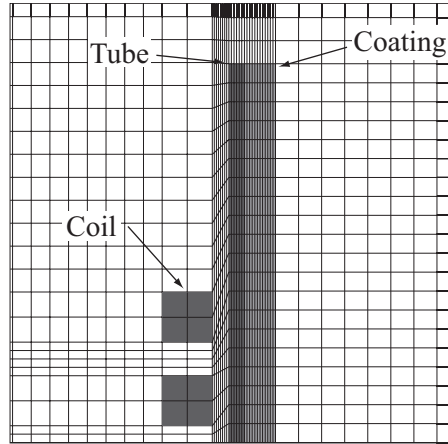
Figure 3.17: Example FEM mesh for axisymmetric expansion of tube with coating.

the tube itself. The deformed shape is plotted at the maximum displacement of the mid-line before unloading, which corresponds to approximately $t/t_0 = 3.9$ for both the un-coated and coated cases. The maximum displacement at $Z = 0$ is significantly decreased, but surprisingly the overall shape of the deformed tube is not impacted significantly.

A plot of the maximum displacement of the tube midline (nondimensionalized with respect to the maximum deformation without coating) against the coating thickness (nondi-mensionalized by the tube wall thickness) for each coating material quantifies the effect of the coating. This result is given in Figure 3.19. As expected, increasing the coating thickness decreases the deformation. Also, the Mooney-Rivlin material has a more pronounced effect on the deformation, due to its stronger stiffening with increasing dis-placement.

3.5 Discussion of Results

The previous sections of Chapter III present a consistent formulation of electromag-netic-thermal-mechanical processes. The result is a variational formulation incorporating the eddy current approximation that is appropriate for modeling EMF processes. This consistent variational formulation combined with variational integration justifies a stag-

Figure 3.18: Effect of polyurea coating twice the thickness of the tube on the deformed configuration at maximum midline displacement of tall tube deformed by four turn coil: $t/t_0 = 3.9$
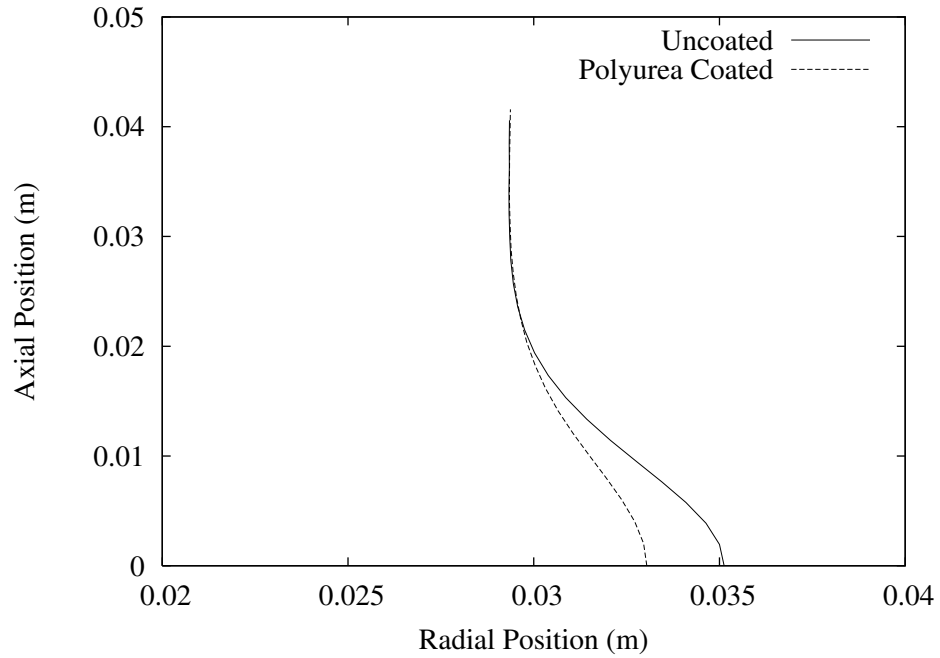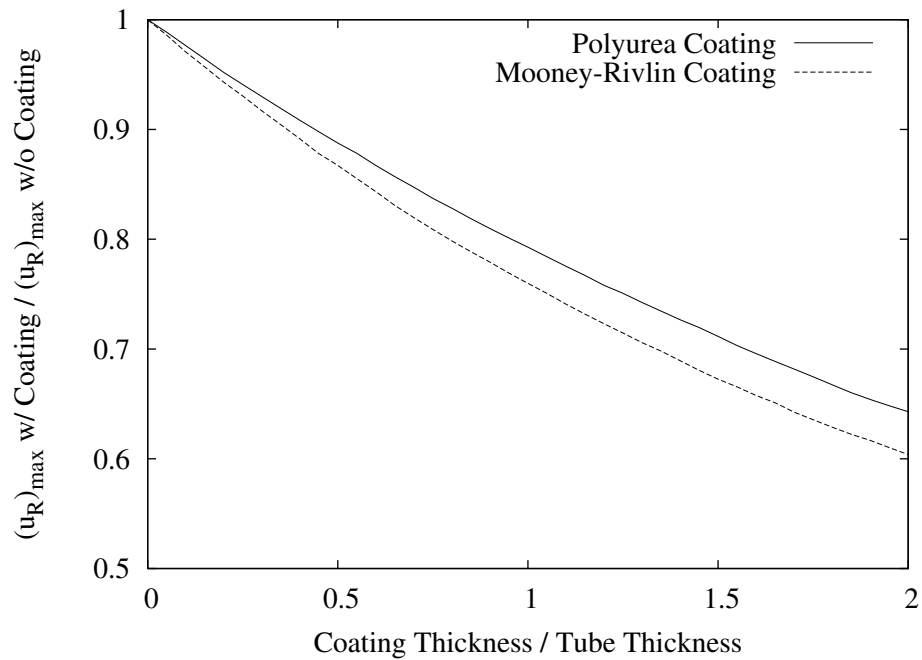

Figure 3.19: Effect of coating materials on the maximum midline displacement of tall tube deformed by four turn coil.

gered solution algorithm that efficiently solves the fully coupled system. This algorithm is implemented for axisymmetric problems, and a range of problems is solved, including ring expansion processes, which are compared with known solutions, and tube expansion processes, which are inspired by the experiments of Section 2.3. Finally, the novel problem of a tube with a non-conducting outer coating is addressed, quantifying the coating's effect.

The general theory presented in Section 3.1 is applicable to any electromagnetic-thermal-mechanical process, and the 3-D theory of Section 3.2 is applicable to any such process that admits the eddy current approximation. Sections 3.2.2, 3.3, and 3.4 specialize this theory to the processes of interest in this work. Axisymmetry is introduced and allows a wide array of practical EMF processes to be simulated while also simplifying the implementation. However, a 3-D implementation will be important to analyze general EMF processes of industrial interest and should be pursued. Also an input electric current, assumed to be known a priori, is employed. Though this is an accurate way to simulate experiments, modeling the forming circuit would be useful for predictive simulations. Implementing a capacitor circuit coupled to the FEM solution is straightforward, and the author has produced results with a capacitor circuit for limited cases. Full implementation of this capability is underway.

In addition, the work here is specialized to hyperelastic materials. The actual plastic response of the workpiece and coatings may be more accurately modeled by elasto-plastic, elasto-visco-plastic, or thermo-visco-plastic material constitutive responses. The third choice would entail the modeling of heat generation as well. Implementing these constitutive models would be complicated by the lack of constitutive data on materials under the forming conditions of EMF, as discussed in Chapter II, though fully coupled modeling such as presented here can help illuminate these issues. Moreover, with more

accurate constitutive modeling one can make quantitative comparisons with experiments, and the author is currently working with experimental researchers to do so.

The work here also presents many opportunities. One may implement the strain localization discussion of Chapter II and/or relevant inertial effects into the coupled electro-magnetic-thermal-mechanical formulation of Chapter III to produce more accurate predictions of ductility in EMF expansion processes. In addition, other forms of failure can be explored, in particular those under electromagnetic compression of tubes, which involve stability analyses. The consistent variational formulation is well suited for stability and energy calculations.

Moreover, the formulations discussed here have application in many other areas besides EMF. One such area is microelectromechanical devices, to which related formulations have been applied (Li and Aluru, 2002). Another area of interest is electroactive materials with magnetization and/or polarization. Implementing magnetization in a numerical implementation similar to that here to solve problems involving magnetic field-responsive polymers and elastomers (Filipcsei et al., 2007; Kankanala and Triantafyllidis, 2004, 2008) is a particularly interesting direction of inquiry.

CHAPTER IV

Conclusion

The electromagnetic-thermal-mechanical process of EMF has the distinct advantage over conventional forming techniques of an increase in ductility for some metal alloys of industrial interest. The FLD is a useful design tool in the prediction of ductility limits for conventional forming techniques. Thus, in the present work, the classical free-expansion FLD concept for flat sheets is extended to include electromagnetic forming operations. In particular, a flat sheet of strain hardening, strain-rate sensitive, and temperature sensitive material, which is subjected to in-plane electric currents and a high strain rate biaxial loading, is modeled using a Marciniak-Kuczynski type weak band analysis. The imposed forming conditions are chosen to correspond with those of actual axisymmetric EMF processes. Though the solution of a fully coupled EMF boundary value problem is required to exactly model the behavior of the metal workpiece under EMF conditions, the present FLD analysis provides significant insight into the formability of the aluminum sheet for EMF processes by focusing on conditions for the onset of a localized necking. The influence of strain hardening, strain-rate sensitivity, temperature sensitivity, yield stress, yield surface, and process characteristics on the forming limits is found and discussed.

This work follows with the quantitative comparison between theoretical calculations for the onset of necking in sheets and experimental results obtained from the free ex-

pansion of electromagnetically loaded aluminum alloy tubes on which strain-measuring grids have been etched. The electromagnetic generalization of the FLD concept is used to study the ductility of aluminum sheets, as measured locally in the necked regions of the failed tubes. Given the approximations inherent in the FLD concept (essentially the assumed strain and current paths that can differ substantially from the actual ones at the necked zone) there is agreement between theory and experiment, showing that the ductility increases in free forming due to the use of an EMF process. The present comparison between theory and experiments shows that the EMF-based FLD concept is a useful tool to predict ductility limits of metal sheet in free expansion experiments.

Also addressed is the solution of fully coupled EMF boundary value problems for predictive modeling of EMF processes. This involves the solution of a coupled electromagnetic-mechanical (and thermal, as necessary) problem. The governing equations are Maxwell's equations in deformable solids and the mechanical equation of motion, both under the eddy current approximation. This implies the need for a consistent, fully coupled variational formulation and an efficient numerical algorithm. Past work in modeling EMF processes has not been based on such a variational framework nor provided such a solution algorithm.

The present work provides a consistent variational formulation that is shown to agree with the known governing equations of coupled electromagnetic-mechanical systems. The variational technique includes the eddy current approximation, so it is appropriate for modeling EMF processes. Moreover, variational integration applied to this formulation justifies a consistent and efficient staggered solution algorithm. The resulting numerical implementation is validated against the known solution of a small cross section ring expanded by a coil composed of small cross section turns. Subsequently, the simulation of the free electromagnetic expansion of tubes is shown to produce results in agreement

with experimental evidence. Following this, the novel problem of an electromagnetically expanded tube with a non-conducting outer coating is addressed, and the effect of the coating is quantified. The validation of the simulation and subsequent results show that the present formulation and implementation provide a fully coupled solution to electro-magnetic-mechanical problems, particularly in the context of EMF.

BIBLIOGRAPHY

Abeyaratne, R., Triantafyllidis, N., 1981. On the emergence of shear bands in plane strain. International Journal of Solids and Structures 17 (12), 1113–1134.

Al-Hassani, S. T. S., Duncan, J. L., Johnson, W., 1967. Analysis of the electro-magnetic metal forming process. In: International Conference on Manufacturing Technology. pp. 853–882, University of Michigan.

Al-Hassani, S. T. S., Duncan, J. L., Johnson, W., 1974. On the parameters of the magnetic forming process. Journal of Mechanical Engineering Science 16 (1), 1–9.

Anand, L., 1979. On H. Hencky's approximate strain-energy function for moderate deformations. ASME Journal of Applied Mechanics 46, 78–82.

Baines, K., Duncan, J. L., Johnson, W., 1965. Electromagnetic metal forming. Proceedings of the Institution of Mechanical Engineers 180 Pt. 1 (4), 93–110.

Balanethiram, V., Daehn, G., 1992. Enhanced formability of interstitial free iron at high strain rates. Scripta Metallurgica et Materialia 27, 1783–1788.

Balanethiram, V., Daehn, G., 1994. Hyperplasticity: Increased forming limits at high workpiece velocity. Scripta Metallurgica et Materialia 31, 515–520.

Barlat, F., Becker, R. C., Hayashida, Y., Maeda, Y., Yanagawa, M., Chung, K., Brem, J. C., Lege, D. J., Matsui, K., Murtha, S. J., Hattori, S., 1997a. Yielding description

for solution strengthened aluminum alloys. International Journal of Plasticity 13 (4), 385–401.

Barlat, F., Maeda, Y., Chung, K., Yanagawa, M., Brem, J., Hayashida, Y., Lege, D., Matsui, K., Murtha, S., Hattori, S., Becker, R., Makosey, S., 1997b. Yield function development for aluminum alloy sheets. Journal of the Mechanics and Physics of Solids 45, 1727–1763.

Becker, R., 2002. Ring fragmentation predictions using the gurson model with material stability conditions as failure criteria. International Journal of Solids and Structures 39, 3555–3580.

Belyy, I. V., Fertik, S. M., Khimenko, L. T., 1977. Electromagnetic Metal Forming Handbook. Hyperplastic Forming Consortium at The Ohio State University, translated by M. M. Altynova, 1996.

Birdsall, D. H., Ford, F. C., Furth, H. P., Riley, R. E., 1961. Magnetic forming. American Machinist 105, 117–121.

Butuc, M. C., Gracio, J. J., Barata da Rocha, A., 2003. A theoretical study on forming limit diagrams prediction. Journal of Materials Processing Technology 142, 714–724.

Chakkarapani, V., Ravi-Chandar, K., Liechti, K. M., 2006. Characterization of multiaxial constitutive properties of rubbery polymers. Journal of Engineering Materials and Technology 128 (4), 489–494.

Coleman, B. D., Noll, W., 1963. The thermodynamics of elastic materials with heat conduction and viscosity. Archive for Rational Mechanics and Analysis 13 (1), 167–178.

Daehn, G. S., Vohnout, V. J., DuBois, L., 1999. Improved formability with electromagnetic forming: fundamentals and a practical example. In: Sheet Metal Forming Technology. pp. 105–115, San Diego, CA; 28 Feb. - 4 Mar.

El-Azab, A., Garnich, M., Kapoor, A., 2003. Modeling of the electromagnetic forming of sheet metals: state-of-the-art and future needs. Journal of Materials Processing Technology 142, 744–754.

Fenton, G. K., Daehn, G. S., 1998. Modeling of electromagnetically formed sheet metal. Journal of Materials Processing Technology 75, 6–16.

Filipcsei, G., Csetneki, I., Szilágyi, A., Zrínyi, M., 2007. Magnetic field-responsive smart polymer composites. In: Advances in Polymer Science. Vol. 206. Springer, pp. 137–189.

Fressengeas, C., Molinari, A., 1989. Tensile instability at high strain rate: Inertial and multiaxial effects. Institute of Physics Conference Series 102, 57–64.

Furth, H. P., Levine, M. A., Waniek, R. W., 1957. Production and use of high transient magnetic fields. II. Review of Scientific Instruments 28 (11), 949–958.

Furth, H. P., Waniek, R. W., 1956. Production and use of high transient magnetic fields. I. Review of Scientific Instruments 27 (4), 195–203.

Gourdin, W. H., 1989. Analysis and assessment of electromagnetic ring expansion as a high-strain-rate test. Journal of Applied Physics 65 (2), 411–422.

Grady, D. E., Benson, D. A., 1983. Fragmentation of metal rings by electromagnetic loading. Experimental Mechanics 23 (4), 393–400.

Hallquist, J. O. (Ed.), 2006. LS-Dyna Theory Manual. Livermore Software Technology Corp., Available at `http://www2.lstc.com/pdf/ls-dyna_theory_manual_2006.pdf`.

Hill, R., 1952. On discontinuous plastic states, with special reference to localized necking in thin sheets. Journal of the Mechanics and Physics of Solids 1, 19–30.

Hiptmair, R., Ostrowski, J., 2005. Coupled boundary-element scheme for eddy-current computation. Journal of Engineering Mathematics 51, 231–250.

Hu, X. Y., Daehn, G. S., 1996. Effect of velocity on flow localization in tension. Acta Materialia 44 (3), 1021–1033.

Hutchinson, J. W., Neale, K. W., 1977. Influence of strain-rate sensitivity on necking under uniaxial tension. Acta Metallurgica 25, 839–846.

Imbert, J., Worswick, M., Winkler, S., Golovashchenko, S., Dmitriev, V., 2005a. Analysis of the increased formability of aluminum alloy sheet formed using electromagnetic forming. In: Sheet/Hydro/Gas Forming Technology and Modeling 2005. SAE International.

Imbert, J. M., Winkler, S. L., Worswick, M. J., Oliveira, D. A., Golovashchenko, S. F., 2005b. The effect of tool-sheet interaction on damage evolution in electromagnetic forming of aluminum alloy sheet. Journal of Engineering Materials and Technology-Transactions of the ASME 127, 145–153.

Kankanala, S. V., Triantafyllidis, N., 2004. On finitely strained magnetorheological elastomers. Journal of the Mechanics and Physics of Solids 52, 2869–2908.

Kankanala, S. V., Triantafyllidis, N., 2008. Magnetoelastic buckling of a rectangular block in plane strain. Journal of the Mechanics and Physics of Solids 56, 1147–1169.

Karch, C., Roll, K., 2005. Transient simulation of electromagnetic forming of aluminum tubes. Advanced Materials Research 6–8, 639–648.

Kleiner, M., Brosius, A., Blum, H., Suttmeier, F., Stiemer, M., Svendsen, B., Unger, J., Reese, S., 2004. Benchmark simulation for coupled electromagnetic-mechanical metal forming processes. Annals of the German Society for Production Technology XI/1, 85–90.

Knoche, P., Needleman, A., 1993. The effect of size on the ductility of dynamically loaded tensile bars. European Journal of Mechanics. A. Solids 12 (4), 585–601.

Kovetz, A., 2000. Electromagnetic Theory. Oxford University Press, Oxford, UK.

Krajewski, P., 2005. The warm ductility of commercial aluminum sheet alloys. In: Lightweight Castings and Aluminum Alloys for Advanced Automotive Applications. SAEI, Warrendale, PA.

Lax, M., Nelson, D., 1976. Maxwell equations in material form. Physical Review B 13 (4), 1777–1784.

Lazzari, B., Nibbi, R., 2000. Variational principles in electromagnetism. IMA Journal of Applied Mathematics 65, 45–95.

L'Eplattenier, P., Cook, G., Ashcraft, C., Burger, M., Shapiro, A., Daehn, G., Seth, M., 2006. Introduction of an electromagnetism module in LS-DYNA for coupled mechanical-thermal-electromagnetic simulations. In: Proceedings from 9th

International LS-DYNA Users Conference. Livermore Software Technology Corp., Dearborn, MI.

LeRoy, G., Embury, J. D., 1978. The utilization of failure maps to compare the fracture modes occurring in aluminum alloys. In: Hecker, S. S., Ghosh, A. K., Gegel, H. L. (Eds.), Formability Analysis, Modeling, and Experimentation. AIME, New York, NY, pp. 183–207.

Li, G., Aluru, N. R., 2002. A lagrangian approach for electrostatic analysis of deformable conductors. Journal of Microelectromechanical Systems 11 (3), 245–254.

Marciniak, Z., Kuczynski, K., 1967. Limit strains in the processes of stretch-forming sheet metal. International Journal of Mechanical Sciences 9 (9), 609–620.

Marsden, J. E., West, M., 2001. Discrete mechanics and variational integrators. Acta Numerica 10, 357–514.

Massin, P., Triantafyllidis, N., Leroy, Y. M., 1999. On the stability of strain-rate dependent solids. I–Structural examples. Journal of the Mechanics and Physics of Solids 47 (8), 1737–1779.

Meagher, T. F., 1964. The conversion of shock energy into shock pulses. ISA Transactions 3, 313–321.

Mercier, S., Molinari, A., 2004. Analysis of multiple necking in rings under rapid radial expansion. International Journal of Impact Engineering 30 (4), 403–419.

Moon, F. C., 1984. Magneto-solid Mechanics. Wiley, New York.

Needleman, A., Triantafyllidis, N., 1978. Void growth and local necking in biaxially

stretched sheets. Journal of Engineering Materials and Technology–Transactions of the ASME 100, 164–169.

Nelson, D. F., 1979. Electric, Optic, and Acoustic Interactions in Dielectrics. Wiley, New York, NY.

Nestorović, M. D., Leroy, Y. M., Triantafyllidis, N., 2000. On the stability of rate-dependent solids with application to the uniaxial plane strain test. Journal of the Mechanics and Physics of Solids 48, 1467–1491.

Ogawa, K., 2001. Temperature and strain rate effects on the tensile strength of 6061 aluminum alloy. In: Chiba, A., Tanimura, S., Hokamoto, K. (Eds.), Impact Engineering and Application. Elsevier Science Ltd., pp. 99–104.

Oliveira, D. A., Worswick, M. J., 2003. Electromagnetic forming of aluminium alloy sheet. Journal de Physique IV 110, 293–298.

Oliveira, D. A., Worswick, M. J., Finn, M., Newman, D., 2005. Electromagnetic forming of aluminum alloy sheet: Free-form and cavity fill experiments and model. Journal of Materials Processing Technology 170, 350–362.

Oosterkamp, L. D., Ivankovic, A., Venizelos, G., 2000. High strain rate properties of selected aluminium alloys. Materials Science and Engineering A278, 225–235.

Pandolfi, A., Krysl, P., Ortiz, M., 1999. Finite element simulation of ring expansion and fragmentation: The capturing of length and time scales through cohesive models of fracture. International Journal of Fracture 95 (1–4), 279–297.

Reese, S., Svendsen, B., Stiemer, M., Unger, J., Schwarze, M., Blum, H., 2005. On a

new finite element technology for electromagnetic metal forming processes. Archive of Applied Mechanics 74, 834–845.

Regazzoni, G., Johnson, J. N., Follansbee, P. S., 1986. Theoretical study of the dynamic tension test. Journal of Applied Mechanics-Transactions of the ASME 53 (3), 519–528.

Rieben, R., Wallin, B., White, D., 2006. Arbitrary lagrangian eulerian electromechanics in 3D. In: Proceedings from Progress In Electromagnetics Research Symposium. pp. 265–269, Cambridge, MA.

Rittel, D., Ravichandran, G., Lee, S., 2002. Large strain constitutive behavior of OFHC copper over a wide range of strain rates using the shear compression specimen. Mechanics of Materials 34 (10), 627–642.

Sanyal, A., Shen, J., McClamroch, N. H., 2005. Variational integrators for mechanical systems with configuration dependent inertia, Preprint, available at `http://math.asu.edu/~sanyal/research/dELmech_pap.pdf`.

Seth, M., 2006. High velocity formability and factors affecting it. Ph.D. thesis, The Ohio State University, Materials Science and Engineering Department, Columbus, OH.

Seth, M., Daehn, G. S., 2005. Effect of aspect ratio on high velocity formability of aluminum alloy. In: Bieler, T. R., Carsley, J. E., Fraser, H. L., Sears, J. W., Smugeresky, J. E. (Eds.), Materials Processing and Manufacturing Division Sixth Global Innovations Proceedings. Trends in Materials and Manufacturing Technologies for Transportation Industries and Powder Metallurgy Research and Development in the Transportation Industry. TMS, pp. 59–64.

Seth, M., Vohnout, V. J., Daehn, G. S., 2005. Formability of steel sheet in high velocity impact. Journal of Materials Processing Technology 168, 390–400.

Sørensen, N. J., Freund, L. B., 2000. Unstable neck formation in a ductile ring subjected to impulsive radial loading. International Journal of Solids and Structures 37, 2265–2283.

Stiemer, S., Unger, J., Svendsen, B., Blum, H., 2006. Algorithmic formulation and numerical implementation of coupled electromagnetic-inelastic continuum models for electromagnetic metal forming. International Journal for Numerical Methods in Engineering 68, 1301–1328.

Stören, S., Rice, J. R., 1975. Localized necking in thin sheet. Journal of the Mechanics and Physics of Solids 23 (6), 421–441.

Svendsen, B., Chanda, T., 2005. Continuum thermodynamic formulation of models for electromagnetic thermoinelastic solids with application in electromagnetic metal forming. Continuum Mechanics and Thermodynamics 17, 1–16.

Takatsu, N., Kato, M., Sato, K., Tobe, T., 1988. High-speed forming of metal sheets by electromagnetic force. JSME International Journal 31 (1), 142–148.

Tirupataiah, Y., Sundararajan, G., 1994. The strain-rate sensitivity of flow stress and strain-hardening rate in metallic materials. Materials Science and Engineering A189, 117–127.

Triantafyllidis, N., 2004. Unpublished work.

Triantafyllidis, N., Massin, P., Leroy, Y. M., 1997. A sufficient condition for the linear

instability of strain-rate-dependent solids. Comptes Rendus de l'Academie des Sciences Series IIB Mechanics Physics Chemistry Astronomy 324 (3), 151–157.

Triantafyllidis, N., Waldenmyer, J., 2004. Onset of necking in electro-magnetically formed rings. Journal of the Mechanics and Physics of Solids 52, 2127–2148.

Trimarco, C., 2007. Material electromagnetic fields and material forces. Archive of Applied Mechanics 77 (2-3), 177–184.

Trimarco, C., Maugin, G. A., 2001. Material mechanics of electromagnetic solids. In: Configurational mechanics of materials. CISM courses and lectures, no. 427. Springer-Verlag, Wien, NY, pp. 129–171.

Unger, J., Stiemer, M., Svendsen, B., Blum, H., 2006. Multifield modeling of electromagnetic metal forming processes. Journal of Materials Processing Technology 177, 270–273.

Vural, M., Rittel, D., Ravichandran, G., 2004. High strain rate behavior of metal alloys at large strains. GALCIT Report, Graduate Aeronautical Laboratories, The California Institute of Technology, Pasadena, CA.

Yadav, S., Chichili, D., Ramesh, K., 1995. The mechanical response of a 6061-T6 Al/Al2O3 metal matrix composite at high rates of deformation. Acta Metallurgica et Materialia 43, 4453–4464.

Yadav, S., Repetto, E. A., Ravichandran, G., Ortiz, M., 2001. A computational study of the influence of thermal softening on ballistic penetration in metals. International Journal of Impact Engineering 25 (8), 787–803.

Zhang, H., Liechti, K. M., Ravi-Chandar, K., 2008. On the dynamics of localization and fragmentation – III. Effect of cladding with a polymer. International Journal of Fracture, to appear.

Zhang, H., Ravi-Chandar, K., 2006. On the dynamics of necking and fragmentation – I. Real-time and post-mortem observations in Al 6061-O. International Journal of Fracture 142, 183–217.

Zhang, H., Ravi-Chandar, K., 2008. Private communication.